Mapping nematic order in $BaFe_2(As,P)_2$

by

Eric Thewalt

A dissertation submitted in partial satisfaction of the

requirements for the degree of

Doctor of Philosophy

in

Physics

in the

Graduate Division

of the

University of California, Berkeley

Committee in charge:

Professor Joseph Orenstein, Chair
Professor James Analytis
Professor Ramamoorthy Ramesh

Fall 2018

Mapping nematic order in $BaFe_2(As,P)_2$

Abstract

Mapping nematic order in $BaFe_2(As,P)_2$

by

Eric Thewalt

Doctor of Philosophy in Physics

University of California, Berkeley

Professor Joseph Orenstein, Chair

The discovery of the iron-based superconductors (Fe-SCs) has been a great boon to the continuing development of our understanding of high-T_c superconductivity, providing a wealth of new information and a valuable theoretical testbed. One of the most interesting developments has been the observation of nematic quantum criticality near optimal doping in several Fe-SCs. This, together with evidence of electronic nematicity in the cuprates, has fueled speculation that high-T_c superconductivity may be related to nematic physics at a fundamental level.

Using ultrafast pump-probe reflectance as a photomodulation technique, we investigate superconducting and nematic order in the low-disorder $BaFe_2(As_{1-x}P_x)_2$ system, which contains a nematic quantum critical point. Our nonequilibrium approach is well-suited to the study of the onset and evolution of ordered phases, as the dominant effect of the pump pulse tends to be the suppression of the ordered phase. This yields a background-free probe of the order parameter, unlike measurements at equilibrium.

At and above optimal doping $x = 0.31$ we observe nematic order manifested in a change in sign of the pump-probe response under polarization rotation. This nematic phase is observed above the superconducting critical temperature and competes with the superconducting phase, and it typically onsets sharply with decreasing temperature in a manner inconsistent with a Curie-Weiss divergence.

We study the spatial variation of the nematic photomodulation response, and find that typical crystals have inhomogeneous nematicity on a length scale of $10-100$ μm. In fact, the sign, magnitude, and onset temperature of the nematic response all vary significantly at optimal doping. The observation of this inhomogeneity helps resolve tension between localized probes that show evidence of nematicity, and bulk probes, which do not.

By combining maps of strain obtained via spatially resolved Laue diffraction with photomodulation maps of nematicity at optimal doping, we test the hypothesis that a strong nematic susceptibility amplifies strain anisotropies intrinsic to the crystal in order to produce the observed nematic behavior. We find that local strain anisotropies cannot account for the

nematic order we observe, although applying a tensile uniaxial strain of 0.1% to an optimally doped sample in the Fe−Fe frame does bias the population of nematic domains.

We extend this multi-probe mapping analysis to the overdoped regime, and find that the nematic fraction of the samples studied decreased sharply for $x > 0.39$. However, each overdoped sample studied contains at least some regions of nematicity of both signs, with the same qualitative character as at optimal doping. Intriguingly, at the highest studied doping, $x = 0.50$, the apparent superconducting transition temperature in otherwise isotropic regions is found to change by 0.5 to 2.0 K under a $\pi/2$ rotation of the pump and probe polarization.

For my family.

Contents

Contents **ii**

List of Figures **iv**

List of Tables **v**

1 Introduction **1**
1.1 Superconductivity in Fe-pnictides . . . 2
1.1.1 Quantum criticality . . . 3
1.1.2 Nematic order in iron-based superconductors . . . 4

2 Optical methods **6**
2.1 Pump-probe reflectivity . . . 6
2.1.1 Photomodulation of an order parameter . . . 7
2.2 Space- and time-resolved measurements . . . 8
2.2.1 Pump-probe alignment in the Montana cryostat . . . 9
2.3 Pulse compression . . . 11
2.4 Surface-sensitivity of $\Delta R/R$ . . . 12

3 Laue microdiffraction **14**
3.1 X-ray diffraction and the strain tensor . . . 14
3.1.1 The strain tensor . . . 15
3.2 Beamtime best practices . . . 15
3.3 Data analysis . . . 17
3.3.1 Optimizing `XMAS` fits . . . 17
3.3.2 Aligning Laue maps to optical maps . . . 19
3.4 Twin peaks: domain fingerprinting in α-$RuCl_3$ . . . 20
3.4.1 Simulating Laue images in `XMAS` . . . 22

4 Initial optical study of nematicity in $BaFe_2(As,P)_2$ **24**
4.1 Introduction . . . 24
4.2 Results . . . 25
4.2.1 Spatial dependence . . . 25

4.2.2 Time and temperature dependence of ΔR . . . 27
4.3 Discussion . . . 31
4.3.1 Breaking C_4 at $T > T_s$ via residual strain for $x < 0.28$? . . . 31
4.3.2 Optimal sample: evidence for strain-induced phase transition . . . 32
4.3.3 Competition between superconducting and nematic order . . . 32
4.4 Conclusion . . . 34

5 Imaging nematicity near the quantum critical point 36
5.1 Methods . . . 38
5.2 Results and discussion . . . 38
5.3 Summary . . . 43
5.4 Additional notes and data . . . 44
5.4.1 Fluence dependence of T_c . . . 44
5.4.2 Photomodulation anisotropy as a proxy for C_4-breaking order . . . 44
5.4.3 Strain is not caused by mounting or cooling . . . 45
5.4.4 Resistivity . . . 46
5.4.5 Reproducibility across samples . . . 47

6 Nematicity beyond optimal doping 48
6.1 Introduction . . . 48
6.2 Results . . . 48
6.2.1 $T_c = 27$ K, $x = 0.39$ . . . 48
6.2.2 $T_c = 18$ K, $x = 0.50$ . . . 52
6.2.3 $T_c = 23$ K, $x = 0.44$ . . . 55
6.3 Discussion . . . 57

7 Summary and prospects 59

Bibliography 60

A Laue indexing tips and tricks 66
A.1 Laue fitting with XMAS desktop . . . 66
A.1.1 Dead pixels . . . 68
A.2 Laue fitting on the XMAS cluster . . . 68
A.2.1 The `NERSC` file . . . 70

List of Figures

1.1 Phase diagram and crystal structure of $BaFe_2(As_{1-x}P_x)_2$ 2
1.2 Manifestations of nematic order in the iron pnictides 5

2.1 Optical landmark for sample stabilization 9
2.2 Illustration of compression optimization 11
2.3 Surface sensitivity of the pump-probe reflectivity experiment 12

3.1 Improvement in indexing results due to decreased angular tolerance 16
3.2 Improvement in cluster fit results due to multigrain fitting 17
3.3 Improvement in cluster fit results due to refined geometry 18
3.4 Landmarking technique to align optical and Laue maps 19
3.5 Optical and Laue maps after region alignment, showing matching features . . . 20
3.6 Simulated α-$RuCl_3$ Laue diffraction patterns 21
3.7 Domain fingerprint example in α-$RuCl_3$ 22

4.1 Early optical maps of underdoped P:Ba122 26
4.2 Line cuts of $\Delta R/R$ at optimal doping 27
4.3 Time and temperature dependence of $\Delta R/R$ in P:Ba122 at $x = 0.14$ 28
4.4 Symmetrized/antisymmetrized $\Delta R(T)/R$ in underdoped P:Ba122 29
4.5 Time and temperature dependence of $\Delta R/R$ in P:Ba122 at $x = 0.31$ 30
4.6 Time dependence of $\Delta R(t)/R$ in two overdoped P:Ba122 samples 31
4.7 Successful fits of $\Delta R/R$ traces based on indirect coupling to superconductivity. . 34

5.1 Crystal structure of P:Ba122 and photomodulation results at optimal doping . . 37
5.2 Spatial variation of optical anisotropy and strain in optimally doped P:Ba122 . . 40
5.3 Comparison of spatial variation and temperature dependence of nematic order for uniaxially and biaxially strained samples of optimally doped P:Ba122 41
5.4 Dependence of apparent T_c on pump power in optimally doped P:Ba122 44
5.5 Successful Curie-Weiss fitting of antisymmetrized $\Delta R/R$ in underdoped P:Ba122 45
5.6 Strain anisotropy distributions for epoxy- and grease-mounted P:Ba122 samples 46
5.7 Resistivity as a function of temperature in optimally doped P:Ba122 46
5.8 Position dependence of $\Delta R/R$ on a different optimally doped P:Ba122 sample . 47

6.1 Spatial variation of optical anisotropy and strain at $x = 0.39$ 49
6.2 Illustration of normal-state and superconducting $\Delta R(t)/R$ integration regions . 50
6.3 Temperature dependence of $\Delta R/R$ at $x = 0.39$ 51
6.4 Spatial variation of optical anisotropy and strain at $x = 0.50$ 53
6.5 Temperature dependence of $\Delta R/R$ at $x = 0.50$ 54
6.6 Selected $\Delta R/R$ traces at $x = 0.50$ 55
6.7 Spatial variation and temperature dependence of $\Delta R/R$ at $x = 0.44$ 56

List of Tables

A.1 Important `NERSC` file parameters 71

Acknowledgments

I am deeply grateful toward the people who have made this work possible and these years at Berkeley so thoroughly worthwhile.

First, to my advisor, Joe Orenstein, thank you for your persistent encouragement and sage advice, especially when delivered with your singular sense of humor. I know I can always count on you for a novel take on pretty much any topic.

I'd also like to extend a warm thank you to my lab mentor Jamie Hinton, who showed me the ropes on the optics table and whose company during late-night data collection is second to none.

Thanks to Shreyas Patankar, Arielle Little, Dylan Rees, and Liang Wu for your help and camaraderie both inside the lab and out, and for making all those trips to La Val's with me.

Thanks also to Ian Hayes, who grew all the $BaFe_2(As_{1-x}P_x)_2$ samples discussed in this work and helped to develop our interpretation of our results.

I am grateful to Nobumichi Tamura and Camelia Stan for teaching me about the micro-Laue experiment, and for extensive help with data collection and analysis.

Thanks to Jake Koralek, Luyi Yang, and Giacomo Coslovich for help and advice during my early years in the lab.

Thank you to Donna Sakima and especially Anne Takizawa for your unending patience in helping me navigate the UC Berkeley system, and for genuinely caring about the students in the physics department.

I will never forget my three years playing for UGMO. (If you don't know, you better ask somebody.) Thank you to the whole UGMO family, and in particular to my physics/frisbee brothers in arms, Matt Jaffe, Michael Girard, Erik Urban, and Greg Salazar.

A big thank you also goes out to my friends Brian Shevitski, Andy Smith, and Patrick Lerchi.

Thank you to Jenifer and Michael Thewalt for your love, support, and trust.

Finally, a deep and heartfelt thank you to my wife Elaine, who knows very well the many reasons why.

This work was supported by:
UC Berkeley Department of Physics and Graduate Division
US Department of Energy, Office of Science
The Gordon and Betty Moore Foundation
National Sciences and Engineering Research Council of Canada

Chapter 1

Introduction

Half a century separated the discovery of superconductivity [1] and the publication of a microscopic theory describing it [2]. Thirty-two years of active research have elapsed since the discovery of high-temperature (high-T_c) superconductivity [3], and its mechanisms still elude a theoretical understanding beyond the phenomenological level.

Certainly, our phenomenological understanding has come a long way in that time. The total violation by the cuprate superconductors and, later, the iron-based superconductors (Fe-SCs) [4, 5, 6] of the famous Matthias rules of superconductivity [7], often playfully paraphrased as "avoid oxygen, magnetism, non-metals, and theorists", emphasizes just how different the high-T_c materials are from their conventional cousins. In the evolving picture of high-T_c physics a new list of apparently useful ingredients has taken shape: strong electronic interactions and even quantum criticality, magnetism, layered structures, complicated Fermi surfaces, and low conductivity in a typically non-Fermi liquid normal state that is often proximate to a (potentially orbital- or momentum-selective) Mott insulating state.

In this thesis we present a comprehensive investigation of the temperature-doping phase diagram of the isovalently doped superconductor $BaFe_2(As,P)_2$. Photomodulation measurements show evidence of a nematic phase that extends significantly beyond the nematic region of the phase diagram as understood by bulk probes. By combining these methods with broadband x-ray diffraction in a spatially resolved setting, we create multi-probe maps of nematic order and strain and show that strain is not the cause of the observed nematic order. Interpreting our results in the context of the broader literature, we propose that a nematic phase confined to the sample surface can account for our observations.

The remainder of this chapter constitutes a brief overview of the physics of the Fe-SCs, and in particular the $BaFe_2(As,P)_2$ (P:Ba122) compound that forms the core of this work. In Ch. 2 and Ch. 3 we discuss the experimental and analytical techniques used in our optical and x-ray measurements, respectively. In Ch. 4 we present our early work on inhomogeneous nematic order in P:Ba122, which led to the hypothesis that local strain in the presence of divergent nematic susceptibility produces a large increase in the magnetic transition temperature. In Ch. 5 we test, and ultimately refute, that hypothesis via a deep dive into the position and strain dependence of nematic order at optimal doping, arriving

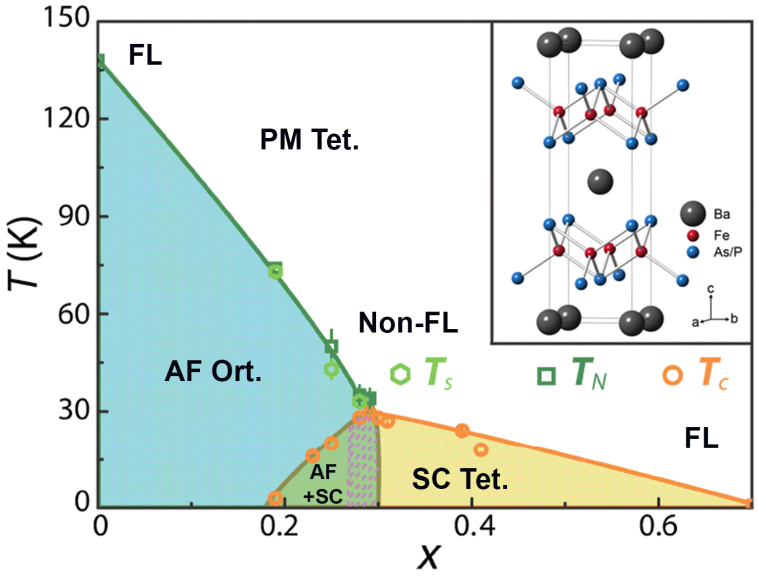

Figure 1.1: Phase diagram and (inset) crystal structure of $BaFe_2(As_{1-x}P_x)_2$. FL, Fermi liquid; SC, superconducting; PM, paramagnetic; AF, antiferromagnetic; Tet., tetragonal; Ort., orthorhombic. Adapted with permission from [8], copyright 2015 American Physical Society.

instead at a model of a nematic phase confined to the surface of the material. Chapter 6 extends that investigation to the overdoped regime. Finally, in Ch. 7 we summarize our results and suggest some avenues for future work.

1.1 Superconductivity in Fe-pnictides

While the origin of high-temperature (high-T_c) superconductivity in correlated electron materials remains mysterious, the discovery of superconductivity in the Fe-pnictides [4, 5, 6] has opened promising new directions in the effort to fully understand this phenomenon. Perhaps most significant is that the addition of the Fe-based compounds to the list of strongly correlated superconducting materials helps to identify common features that may be essential to creating a high-T_c superconductor.

The Fe-SCs differ from the cuprate family of SCs in that superconductivity in Fe-SCs can be induced not only by charge doping, but also by the application of hydrostatic pressure or by isovalent doping. The antiferromagnetic spin density wave (SDW) phase in $BaFe_2As_2$ is coupled to the Fe-As distance and the As-Fe-As bond angle [9], and when pressure is applied the resulting structural changes suppress the SDW [10]. Our compound of focus, P:Ba122, whose phase diagram [8] and crystal structure is shown in Fig. 1.1, is an example of an isovalently doped superconductor, and a low-disorder model system for superconductivity in Fe-based compounds. In P:Ba122, the causal relationship between crystal lattice changes

and SDW suppression is reversed: superconductivity arises as the competing SDW phase is suppressed due to the broadening of the Fe-$d_{xz,yz}$ bands with increasing P concetration [9]. Another notable distinction between the two SC families is that the antiferromagnetic parent compound in the cuprates is insulating, while in the Fe-pnictides it is typically a bad metal.

However, the Fe-pnictides reinforce the view that a key ingredient of a high-T_c superconductor is a non-superconducting, often antiferromagnetic phase whose transition temperature can be driven to zero by adjustment of a tuning parameter, x, such as pressure, magnetic field, or chemical composition. Superconductivity typically appears in a dome-like region in the $T-x$ plane roughly centered at the point x_c where this transition temperature reaches zero. This point is known as a quantum critical point (QCP), marking a continuous phase transition at zero temperature.

1.1.1 Quantum criticality

Although the basic phenomenology of superconductivity in correlated materials is well established, achieving a unified theory that accounts for all of the observations has proved challenging. One compelling theoretical paradigm is quantum criticality, which focuses on the effects of a QCP on the physics in the phase diagram neighborhood of x_c. The length and time scales of the quantum critical fluctuations associated with a QCP diverge as the QCP is approached, and thus the fluctuations have a significant effect on a material's behavior in a broad region of parameter space around the QCP, in particular at temperatures well above 0 K. For instance, in metals featuring an antiferromagnetic QCP, the resitivity ρ is a linear function of temperature in the vicinity of the QCP, in contrast to the normal Fermi-liquid metallic behavior, $\rho \sim T^2$. This T-linear resistivity state is referred to as a strange metal or non-Fermi liquid. In the quantum critical picture of high-T_c superconductivity, such fluctuations are responsible for amplifying or even generating the Cooper-pair instability.

Although the evidence for the connection between quantum criticality and superconductivity has been pursued with great intensity in the high-T_c cuprates, the theoretical picture is challenged by ambiguities associated with the pseudogap phase. In sharp distinction to the cuprates, it is clear what symmetries are broken in the Fe-pnictides, making them ideal platforms for testing quantum critical scenarios. In the parent, non-superconducting compounds, the high-temperature tetragonal/paramagnetic state evolves to a low-temperature orthorhombic/antiferromagnetic phase [11, 12, 13, 14, 15]. The broken-C_4 (orthorhombic) phase is referred to as *nematic*, and the driving force for the transition is most likely electronic correlations related to the incipient magnetic or orbital order, rather than structural instability [16].

There are several independent signs that quantum criticality plays an important role in the P:Ba122 phase diagram. The non-Fermi liquid nature of the normal state above the superconducting dome is a key feature of the phase diagram of P:Ba122 [17, 18]. In addition to T-linear resistivity in the neighborhood of x_c, where the SDW transition extrapolates to 0 K, indications of quantum criticality in the form of effective mass (m^*) enhancement have been observed [19]. Particularly striking is the observation of a cusp near x_c in the variation

of the superconducting penetration depth (λ_L) with x [20], which can be interpreted as a divergence of m^*/n_s, where n_s is the density of Cooper pairs. Furthermore, elastoresistance measurements reveal a divergent nematic susceptibility in P:Ba122 and several other Fe-SCs, suggesting the presence of a quantum critical point at a nematic phase transition [21].

However, neutron scattering and nuclear magnetic resonance measurements indicate that, at least in the temperature-doping plane of the P:Ba122 phase diagram, the SDW transition does not extend to 0 K, instead terminating into a region of microscopic phase separation [8]. In addition, while the sharp peak in $\lambda_L(x)$ seems to suggest the existence of a QCP under the dome of superconductivity, general theoretical arguments predict instead a monotonic increase in penetration depth with tuning from the superconducting to antiferromagnetic phase [22], and that a peak in $\lambda_L(x)$ is expected in the presence of microscopic phase separation near x_c [23]. A consistent understanding of these naively contradictory findings may require a multi-band approach [24].

1.1.2 Nematic order in iron-based superconductors

Much of the discussion in the following chapters focuses on nematic physics and phases of matter. The term *nematic* originated to describe a phase of classical liquid crystal where rod-like molecules spontaneously develop a common orientation, breaking rotational symmetry. (There is a rich variety of other classical oriented phases that break additional symmetries, many of which have their own names.) In the context of quantum materials the term is typically used more inclusively, describing phases with a preferred spatial axis that may also exhibit broken inversion, translational, or time-reversal symmetry [25].

The order parameter for a pure nematic phase (i.e., one lacking additional broken symmetries) is a director, which, like the rod-shaped molecules in the classical nematic phase, corresponds to an axis in space but does not distinguish between the two directions along that axis. In the Fe-SCs, the four-fold rotational symmetry of the crystal lattice implies that there are only two possibilities for the axis of this director, so the nematic phase in the Fe-SCs is called Ising-nematic. Figure 1.2 illustrates three different forms in which nematic order is exhibited in the Fe-SCs: structural (**a**), magnetic (**b**), and electronic (**c**) [26]. Our optical experiments directly probe electronic nematicity, but all three forms of nematic order are coupled due to their identical symmetry. The onset of one thus generically induces the others.

The location of the boundary of the nematic phase in P:Ba122 remains the source of some debate. Bulk probes, including neutron and x-ray scattering, transport, NMR [8], and specific heat [27], indicate that the (nematic) SDW phase onsets above the superconducting transition temperature T_c for P concentration up to, but not above, $x = 0.29$, just below optimal doping ($x = 0.3$). Despite the evidence from these bulk probes, persistent hints that C_4 symmetry is broken in samples with $x > 0.3$ suggest that there is more to the story. Angle-resolved photoemission (ARPES) [28, 29] and torque magnetometry [30] studies have found evidence of broken C_4 symmetry above the dome of superconductivity persisting above optimal doping in P:Ba122, and optical data suggest similar behavior in $Ba(Fe,Co)_2As_2$ [31].

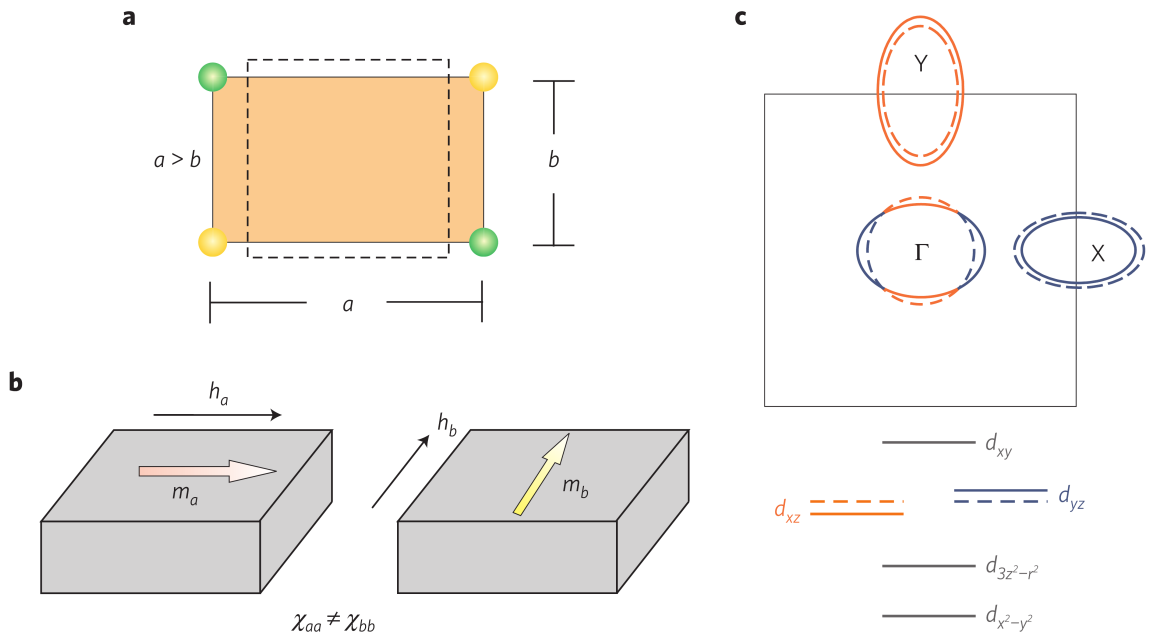

Figure 1.2: Manifestations of nematic order in the iron pnictides. **a**, Structural distortion from a tetragonal (dashed line) to an orthorhombic (solid line) unit cell. **b**, Anisotropy in the uniform spin susceptibility $\chi_{ij} = m_i/h_j$, where m_i denotes the magnetization along the i direction induced by a magnetic field h_j applied along the j direction. **c**, Splitting of the d_{xz} and d_{yz} orbitals (orange and blue lines, respectively). The corresponding distortion of the Fermi surface is also shown. This figure originally appeared in [26], and is reprinted with permission from Springer Nature.

Based on the measurements reported in Ch. 5 and Ch. 6, we propose that the nematic phase in P:Ba122 is confined to the surface of the crystal for dopings without a bulk SDW phase.

Chapter 2

Optical methods

2.1 Pump-probe reflectivity

The optical experiments described in this thesis are measurements of pump-probe reflectivity, also known as transient reflectivity. The basic experimental configuration is as follows.

An ultrafast pulse ($\sim$ 100 fs duration) of linearly polarized near-infrared light with center wavelength 800 nm is split into two beams with a power ratio of approximately 5:1. The weaker (probe) beam is sent down a variable delay line. The stronger (pump) beam passes through an amplitude modulator; we use a photoelastic modulator followed by a polarizer to rotate the pump polarization by $\pi/2$ relative to the probe while modulating the pump power at 100 kHz. The pump and probe beams are then focused onto the sample, and the reflected probe beam is collected into a detector. The ratio of the component of the detector voltage at the modulation frequency (100 kHz) to the DC component is the change in reflectivity induced by the pump pulse. By varying the delay of the probe pulse with respect to the pump, we can trace out the time dependence of the pump-induced change in reflectivity, $\Delta R/R$.

We briefly enumerate important additional components of the optical setup for future reference. A pulse compressor compensates for second-order dispersion in the optical path, and is discussed further in Sec. 2.3. Silica plates in the probe beam path match the dispersion that the pump pulses accumulate when passing through the photoelastic modulator. Neutral-density filters allow for independent control of the pump and probe intensities. A cage system houses the microscope objective that focuses the pump and probe onto the sample, along with a half wave plate, used to rotate the polarization of the pump and probe beams simultaneously, and a 50:50 beamsplitter, which allows the pump and probe beams to enter the microscope objective and extracts the reflected beams (the associated loss of power is inconsequential, as we typically filter the power down by a further factor of at least 10). The cage system allows the (upward-facing) sample to be replaced with minimal disruption to the optical alignment while keeping the half-wave plate as close as possible to the sample, which minimizes depolarization when the pump/probe polarizations are rotated away from

the lab frame. The 50:50 beamsplitter in the cage should be as non-polarizing as possible at the laser wavelength. Finally, a polarizer and physical filter are used to select the probe beam emerging from the microscope objective and reject the pump beam.

In order to minimize laser-induced heating of the sample, the laser intensity is kept as low as good signal-to-noise allows. The typical energy scale of the pump pulse at the sample surface is 40 pJ; the probe pulse is normally several times weaker.

2.1.1 Photomodulation of an order parameter

Pump-probe reflectivity provides a sensitive probe of ordered phases via photomodulation of the corresponding order parameters. For these purposes we define photomodulation (PM) as the change in reflectivity ΔR induced by photoexcitation with a pump pulse. The change in reflectivity is related to the change in the complex reflection coefficient, δr, through the relation $\Delta R = 2Re\,[r * \delta r]$, where r is the equilibrium reflection coefficient. In the experiments described in this thesis, ΔR is independent of the polarization of the pump beam, and linearly proportional to the energy, u, that the sample absorbs from the pump pulse. As u is a scalar quantity, the PM response is a rank-two tensor, like the reflectivity itself.

There are two main sources of PM in metals. In one, photoexcitation perturbs the electron occupation function by changing the electron temperature and/or chemical potential. The change in electron occupation modulates the dielectric function and consequently the reflectivity. Typically, PM that originates from this mechanism is relatively insensitive to temperature. A second source of PM occurs in metals that undergo phase transitions to states with magnetic, charge, orbital, or superconducting order. In such systems, the onset of the ordered phase alters the density of states and hence the equilibrium reflectivity. Photoexcitation perturbs the ordered state, typically weakening the order parameter, leading to a transient change in reflectivity. The amplitude of ΔR provides a local probe of the onset of order as a function of temperature.

As a method for detecting the onset of symmetry-breaking order, measurement of the photomodulation signal $\Delta R(T)$ can be more effective than measurement of the equilibrium reflectivity, $R(T)$. For a given direction of probe polarization, the dependence of the reflectivity on the order parameter can be described by $R(T) = R_0 + \alpha\phi(T)/\phi(0)$ where R_0 is a background contribution that is insensitive to order, $\phi(T)$ is a T-dependent order parameter, and α is a dimensionless coefficient. In the limit that the dominant effect of the pump pulse is to perturb the order parameter, $\Delta R(T)$ becomes a background-free probe of ϕ. The utility of PM as a method to detect order is enhanced by the stability of pulsed light sources such as the Ti:Sapphire oscillator operating at 1.5 eV, which enables measurement of $\Delta R(T)$ at the parts-per-million level.

Absorption of energy from the pump weakens ϕ in one of two ways. If the pump pulse increases the electron temperature, T_e, then $\Delta R(T) = \alpha(\partial\phi/\partial T)(\partial T_e/\partial u)\,u$, and the resulting PM signal will be proportional to the temperature derivative of the order parameter. The signature of this mechanism is a sharp peak in $\Delta R(T)$ at the critical temperature for

the onset of order. The other possibility is that absorption of energy from the pump causes a fractional reduction in the order parameter, $\delta\phi/\phi$, that depends linearly on the absorbed energy u and is independent of ϕ. If we express the photoinduced weakening of ϕ by a parameter, A, such that $\delta\phi/\phi = Au$, then $\Delta R(T) = A\,\alpha\,\phi(T)\,u$, and $\Delta R(T)$ is directly proportional to $\phi(T)$, rather than its derivative with respect to T. This mechanism dominates in PM measurements in P:Ba122.

The main focus of our optical work is the onset of order that lowers the point group rotational symmetry from four-fold (C_4) to two-fold (C_2). In the presence of C_4 symmetry, $\Delta R(T)$ is a scalar quantity; it is independent of the direction of the probe electric field with respect to the crystalline axes. Lowering of C_4 to C_2 allows for an anisotropic PM signal, described by the relation

$$\begin{pmatrix}\Delta R_a \\ \Delta R_b\end{pmatrix} \propto (\alpha_e\,\mathbf{1} + \alpha_o\,\boldsymbol{\sigma}_z)\,\phi(T) \tag{2.1}$$

where ΔR_a and ΔR_b are the photomodulation with the probe polarized along the (orthogonal) vectors $\boldsymbol{a}$ and $\boldsymbol{b}$, and $\mathbf{1}$ and $\boldsymbol{\sigma}_z$ are the unit and Pauli z matrices, respectively. The parameters α_e and α_o are coefficients that describe the even and odd components of $\Delta R(T)$, respectively, under rotation of the probe polarization by $\pi/2$. A nonzero α_o, or equivalently a nonzero value of $\Delta R_a - \Delta R_b$, indicates that C_4 symmetry is broken. Another implication of Eq. 2.1 that is important for interpretation of our results is that, in the presence of a single order parameter, $\Delta R_a(T)$ will be proportional to $\Delta R_b(T)$, so that a lack of proportionality $\Delta R_a(T) \propto \Delta R_b(T)$ indicates the presence of multiple forms of order.

2.2 Space- and time-resolved measurements

Early on in our studies of P:Ba122 we were puzzled by what appeared to be unexpectedly wild temperature dependence in the sub-50 K regime, including multiple changes in the sign of the pump-probe response. Such changes in sign typically accompany a phase transition, of which we expected to observe at most one at low temperatures. Furthermore, slight movements of the sample yielded completely different temperature dependence.

We hypothesized that we were observing not a wild temperature dependence in the pump-probe response, but rather, significant spatial variation in both its amplitude and sign. As the sample was mounted on the end of a copper cold finger, with increasing temperature the thermal expansion of the cold finger caused the sample to move relative to the pump-probe focus, so that inhomogeneity would manifest as apparent temperature dependence.

In order to test this hypothesis we implemented a coarse form of position control, using a high-resolution, high-magnification video feed in combination with an optical landmark (an X etched with a razor blade and illuminated) to track the movement of the sample, and a manual three-axis translation stage to return the sample to its original position.

After bringing the sample position under control, we found that the temperature dependence at a fixed position was indeed much more natural. We studied the spatial variation of

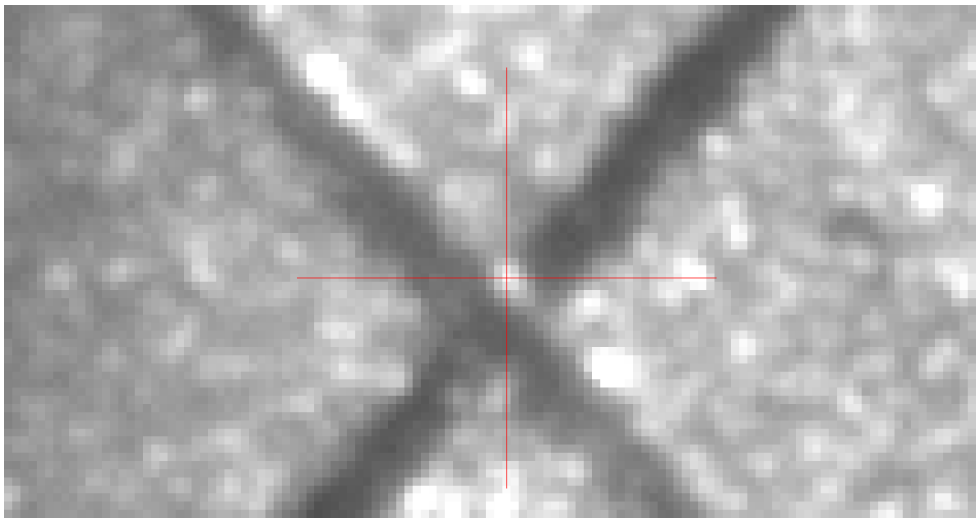

Figure 2.1: An example of an optical landmarking image. The cross of the etched X is apparent, and stabilization of the small reflection features relative to the overlaid red cross gives position control at the 5 μm level.

the pump-probe response and observed striking inhomogeneity at the 100 μm scale, which is discussed at length in Ch. 4-6. (Figure 4.1**A** in Ch. 4 shows an example of a pump-probe map obtained via manual position control.)

The observation of this inhomogeneity motivated the acquisition of a new Montana Instruments closed-cycle cryostat including a three-axis Attocube piezo stage that allows position control at the 1 μm level. We simultaneously upgraded our optical setup to reduce the pump-probe focal diameter from 75 μm to 10 μm. These improvements enabled us to collect high-resolution images of the pump-probe response in P:Ba122. An example of a pump-probe map collected using the Montana cryostat is shown in Fig. 4.1**B**.

2.2.1 Pump-probe alignment in the Montana cryostat

Aligning the pump and probe beams so that they are optimally focused at the same position on the sample surface is more difficult in the Montana cryostat than in earlier configurations, where a portable cryostat attached to a translation stage could be temporarily replaced with a pinhole. In this section we describe some techniques that help make this process feasible.

When aligning for the first time after a hiatus, it is best to begin by aligning the system using a sample with a large room-temperature pump-probe response, such as GaAs. This alignment sample can be placed alongside the sample of interest, but if that is impractical due to space constraints, the replacement of the alignment sample with the sample of interest need not be an invasive process. If the cage containing the objective is located at an extreme of travel in the vertical direction (for instance, if some component touches one of the cage support arms), it is easy to remove the cage without adjusting the rotation or position of

the cage support. The sample can then be changed out, and the cage returned to the same position with very good accuracy.

Since both the pump and the probe beams are focused onto the sample by the same microscope objective, it is useful to start the alignment process with these beams close to parallel. This is achieved using two pairs of extra-wide (in order to accomodate both beams) irises fixed to the optics table grid, one centered on each beam, just before the periscope that steers the beams into the cage system. A final set of steering mirrors for each beam allows the pump and probe to be centered through these iris pairs. Since the pump beam is rejected in part based on its spatial displacement relative to the probe, it is useful to place the irises so that there is a several-mm distance between the pump and probe beams. However, the further apart the pump and probe beams are, the more difficult it is to avoid clipping at some point in the cage, so in practice this separation (between the beam centers) should not be more than around 7 mm.

Once the approximately parallel pump and probe beams are entering the objective without clipping, the next step is to move the sample vertically so that its surface lies near the focal plane of the objective. This process is facilitated by picking off the beams reflected from the sample (after they return through the objective) and directing them to one of the lab walls. The goal is to locate the focus of the reflected pump and probe beams at infinity. This is easiest to optimize by first moving the sample so that the focus is within the lab, then tweaking the vertical position until the outgoing beams are collimated.

When the pump and probe are approximately focused on the sample surface, the next step is to optimize the steering of the pump beam relative to the probe so that both beams are focused at the same spot on the sample. To check this, it is now useful to record a pump-probe signal and maximize its magnitude, so the probe reflection from the sample should be steered into the detector, after which the probe steering is left fixed. Full pump and probe power should be used at this stage, so that a signal will be visible even with imperfect alignment. The pump steering is tweaked using the same steering mirrors that were used to steer the pump into the irises before the pre-cage periscope.

If a signal does not appear after some searching, the steering can be systematically optimized by adjusting the transverse position so that the beams are focused near an edge of the sample. By moving the sample a short distance at a time, a position can be found where one beam is reflecting off the sample surface while the other beam has "fallen off". It is then straightforward to determine the direction in which the pump needs to move in the relevant dimension. This process can be iterated until the pump and probe appear to fall off the sample at approximately the same position, after which the process can be repeated using an orthogonal sample edge and adjusting the steering in the other dimension.

Once a pump-probe signal is observed, the pump steering should be carefully adjusted to maximize the signal, after which the focus and steering alignment procedure is repeated at least once more. The uncertainty in the optimal focus should not be more than about 10 μm.

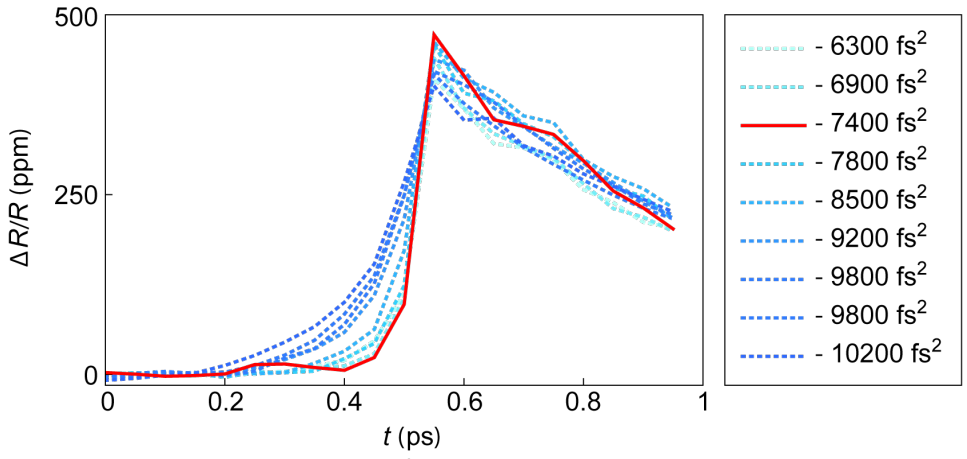

Figure 2.2: Illustration of compression optimization. Pump-probe traces are collected on GaAs with varying levels of compression in order to determine the compression corresponding to the shortest rise time. In this experiment, optimal compression (solid red trace) corresponded to a group delay dispersion of approximately -7400 fs^2.

2.3 Pulse compression

An ultrafast pulse consists of a superposition of many adjacent longitudinal modes of an optical cavity with a constant phase difference δ between neighboring modes. (Strictly speaking, in this constant-δ, or "mode-locked", configuration, the frequencies ω_i composing the pulse are shifted slightly relative to the cavity modes, so that there is a constant difference $\Delta\omega$ between the emitted (angular) frequencies.) When a pulse interacts with a dispersive optical element, the wave carrying the component at frequency ω_i accumulates a phase $\varphi(\omega_i)$, which changes the phase difference between the ω_i and $\omega_{i+1} = \omega_i + \Delta\omega$ waves: $\delta \to \delta'(\omega_i) = \delta + \varphi(\omega_i + \Delta\omega) - \varphi(\omega_i)$. Taylor expanding, $\delta'(\omega) = \delta + \Delta\omega \frac{d\varphi}{d\omega}\Big|_{\omega_i} + \frac{(\Delta\omega)^2}{2!}\frac{d^2\varphi}{d\omega^2}\Big|_{\omega_i} + \mathcal{O}\left((\Delta\omega)^3\right)$. The n-th derivative of $\varphi(\omega)$ is said to contribute n-th order dispersion to the pulse.

If $\varphi(\omega)$ is linear then $\delta'(\omega)$ is constant, and the pulse remains perfectly mode-locked. However, for a generic dispersive element the Taylor expansion of $\varphi(\omega)$ contains terms of all order and thus all orders of dispersion contribute to pulse broadening. In practice, it is usually possible to obtain pulses shorter than 50 fs by cancelling only the second-order dispersion $D_2(\omega) = \frac{d^2\varphi}{d\omega^2}$, also known as group delay dispersion (GDD). This dispersion cancellation can be achieved by determining the total GDD produced by the optics in the experiment, D_2^{tot} (which will often be dominated by a single highly-dispersive element), and inserting a carefully tuned optical element with GDD $-D_2^{tot}$. Typically, $D_2^{tot} > 0$, in which case the compensating element must have negative, or anomalous, dispersion, which can be obtained from a prism compressor.

In our experiment, the optical path contains many sources of dispersion, some of which are not well-characterized. These dispersion sources include the microscope objective and

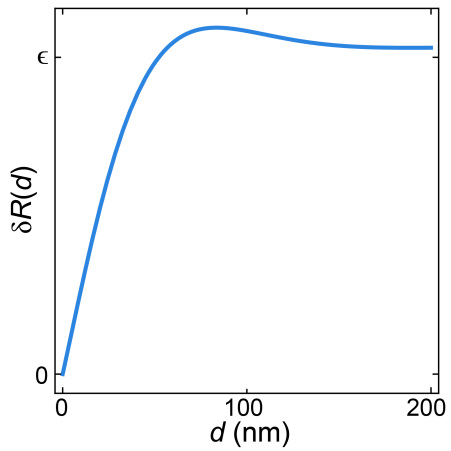

Figure 2.3: Relative change in reflectivity as a function of surface phase depth for a material with bulk refractive index $n = 1.9 + 1.9\,i$ and a surface phase of depth d with refractive index $n_s = 1.9 + (1+\epsilon) \times 1.9\,i$, in the limit of small ϵ. For a hypothetical surface phase with 10 nm depth, $\delta R(10\text{ nm}) = 0.27\epsilon$.

photoelastic modulator mentioned above, along with multiple wave plates and beamsplitters. This renders estimates of the total dispersion unreliable. We find that the most practical approach to dispersion compensation is to optimize the rise time of the pump-probe signal as a function of pulse compression, with the help of a broadly tunable commercial pulse compressor (Thorlabs FSPC). This optimization process is illustrated in Fig. 2.2.

2.4 Surface-sensitivity of $\Delta R/R$

While optical techniques are sometimes considered bulk probes, they are in fact quite surface-sensitive in materials whose refractive index has a significant imaginary component. In this section we show that the pump-probe technique is sensitive to a hypothetical surface phase in P:Ba122, even if the depth of that phase is smaller than the optical wavelength or penetration depth. This result will be especially relevant in the context of the data presented in Chapter 5.

In optimally doped $Ba(Fe,Co)_2As_2$ the optical reflectivity is $R_0 = 0.368$ and the optical conductivity is $1.506 \times 10^5\ \Omega^{-1}\ \text{m}^{-1}$ [32]. These values correspond to a penetration depth of 34 nm and a complex refractive index $n = 1.9 + 1.9\,i$, which we use in the absence of a value specific to P:Ba122.

We consider the reflectivity of a crystal with bulk refractive index n and a surface phase of depth d with refractive index

$$n_s = 1.9 + (1+\epsilon) \times 1.9\,i.$$

The Fresnel reflection coefficients for the vacuum-surface, surface-vacuum, and surface-bulk interfaces are $r_{12} = 1 - \frac{1-n_s}{1+n_s}$, $r_{21} = -r_{12}$, and $r_{23} = \frac{n_s-n}{n_s+n}$ respsectively, and the transmission coefficient from vacuum to surface is $t_{12} = \frac{2}{1+n_s}$. This yields a vacuum-surface transmittance $T_{12} = n_s t_{12}^2 = \frac{4n_s}{(1+n_s)^2}$. The total reflection coefficient, then, is

$$r(d) = r_{12} + T_{12} \frac{r_{23}\, e^{2i\phi(d)}}{1 - r_{23}\, r_{21}\, e^{2i\phi(d)}},$$

where $\phi(d) = \frac{2\pi}{800\ \text{nm}} n_s d$ is the phase accumulated in one pass through the surface layer. From the reflection coefficient we can extract the relative change in reflectivity,

$$\delta R(d) = \frac{|r(d)|^2 - R_0}{R_0},$$

due to the surface phase. In the strong-pump regime, where the pump pulse totally evaporates the surface phase (sending $\epsilon \to 0$), this quantity is the measured $\Delta R/R$.

We plot $\delta R(d)$ in the limit of small ϵ in Fig. 2.3. With a surface phase that is only 10 nm thick, the relative change in reflectivity is 0.27ϵ, which would be readily detected by our experiment for a typical value of $\epsilon = \mathcal{O}(0.01)$.

Chapter 3

Laue microdiffraction

In recent years our optical experiments have been complemented by a new technique: scanning Laue microdiffraction measurements of crystal structure and strain at beamline 12.3.2 at the Advanced Light Source [33]. In this chapter we give a brief review of the principles behind the technique and some of the quantities that it measures, followed by a practical overview of some important experimental best practices and analytical approaches that we have identified in the course of our work.

3.1 X-ray diffraction and the strain tensor

Consider an x-ray plane wave with wavelength λ and wavevector $\boldsymbol{k}$ incident on a crystal with principal axes $\boldsymbol{a}_i$ (alternatively written $\boldsymbol{a}$, $\boldsymbol{b}$, $\boldsymbol{c}$). Each illuminated atom in the crystal scatters the incoming wave elastically, and constructive interference can occur for scattered wavevectors $\boldsymbol{k}'$ satisfying $e^{2\pi i(\boldsymbol{k}-\boldsymbol{k}')\cdot\boldsymbol{x}} = 1$, where $\boldsymbol{x}$ is any lattice vector. This is the definition of the reciprocal lattice in the "crystallographer's normalization": $\boldsymbol{k} - \boldsymbol{k}' \equiv \boldsymbol{Q}_{hkl} = h\boldsymbol{\beta}_1 + k\boldsymbol{\beta}_2 + l\boldsymbol{\beta}_3$, where $\boldsymbol{a}_i \cdot \boldsymbol{\beta}_j = \delta_{ij}$ and $h, k, l \in \mathbb{Z}$. (In these units, $|\boldsymbol{k}| = 1/\lambda$.) Thus, constructive interference can occur when the change in wavevector is a reciprocal lattice vector.

This scattering can be visualized as specular reflection from a family of lattice planes (hkl) orthogonal to $\boldsymbol{Q}_{hkl}$, with spacing $|\boldsymbol{Q}_{hkl}|^{-1}$. In this picture, constructive interference can occur when the x-ray wavelength and angle of incidence θ satisfy the Bragg condition, $n\lambda = 2\,|\boldsymbol{Q}_{hkl}|^{-1} \sin\theta$, $n \in \mathbb{Z}$, and we label the resulting diffraction peak (h, k, l). The diffraction peak (nh, nk, nl) corresponding to wavelength λ/n has outgoing wavevector $n\boldsymbol{k}'$, and thus coincides with the peak (h, k, l), so the labels are given in lowest terms, $\gcd(h, k, l) = 1$.

Our discussion thus far has made no mention of the intra-unit cell structure of the crystal. Indeed, the intensity of the diffraction peaks depends on the distribution of electron density in the unit cell, and thus on both the constituent atoms and their locations. The resulting interference can be destructive, cancelling out some of the peaks predicted based on the crystal axes; see [34] for more details.

In Laue diffraction, collimated x-rays with a broad range of energies (approximately

$5 - 20$ keV in our experiment) illuminate a sample, simultaneously satisfying the Bragg condition for many different lattice planes, and the resulting diffraction peaks are imaged on a detector.

3.1.1 The strain tensor

The Laue microdiffraction experiment allows for the precise determination of the crystal orientation as a function of position, as well as the deviatoric strain. Deviatoric strain is a measure of relative, volume-preserving strain, and is encoded in the lattice constant ratios b/a and c/a, as well as the unit cell angles α, β, and γ. Equivalently, the deviatoric strain can be expressed in the form of a traceless rank-3 tensor $\boldsymbol{\varepsilon}$, with diagonal components corresponding to expansion or compression in a basis direction and off-diagonal components corresponding to pure shear. When the lattice parameters change, the diffraction peaks composing the Laue pattern move slightly, and the coherent motion of the large number of peaks in a typical diffraction pattern allows for sensitive detection of changes in e.g. b/a, comparable to one part in 10^4.

In Chapters 5 and 6 we use these deviatoric strain data to gain insight into the origin of nematicity in $BaFe_2(As,P)_2$. Due to the layered nature of these compounds and the strongly two-dimensional physics that results, it is useful to define the restriction of the strain tensor to the transverse (ab) plane, a rank-2 quantity denoted by $\boldsymbol{\varepsilon}^{(t)}$. We can then represent a few useful quantities in terms of $\boldsymbol{\varepsilon}^{(t)}$: the transverse unit cell dilation is given by $\mathrm{Tr}\,\boldsymbol{\varepsilon}^{(t)}$, the strain anisotropy in the ab basis is $\varepsilon^{(t)}_{bb} - \varepsilon^{(t)}_{aa}$, and the transverse equivalent strain (a measure of total strain) is $(2\varepsilon^{(t)}_{ij}\varepsilon^{(t)}_{ij}/3)^{1/2}$ with implicit summation over the repeated indices.

3.2 Beamtime best practices

In this section we collect a few suggestions that will help a user get the most out of time at the beamline.

First and foremost, it is very important to adjust the exposure time to ensure that the detector is not overloaded, or that at most a few peaks are overloaded in a few pixels. Ordering peaks by intensity is a critical part of the indexing process, and when peaks are thresholded this ordering can fail. In order to check for overloading, collect a single diffraction pattern and load it into `XMAS`, the Laue pattern analysis program*, then adjust the intensity range to include $2^{16} = 65536$ and check any obvious bright peaks for pixels that match or exceed that intensity. If there is significant overloading, reduce the exposure time and try again.

There tends to be interesting information at multiple length scales in the micro-Laue data. It is particularly useful to collect a coarse-resolution dataset that shows the crystal's edges. This can be used later on to align the micro-Laue maps with, for instance, optical

*We used version 6 in the work described here.

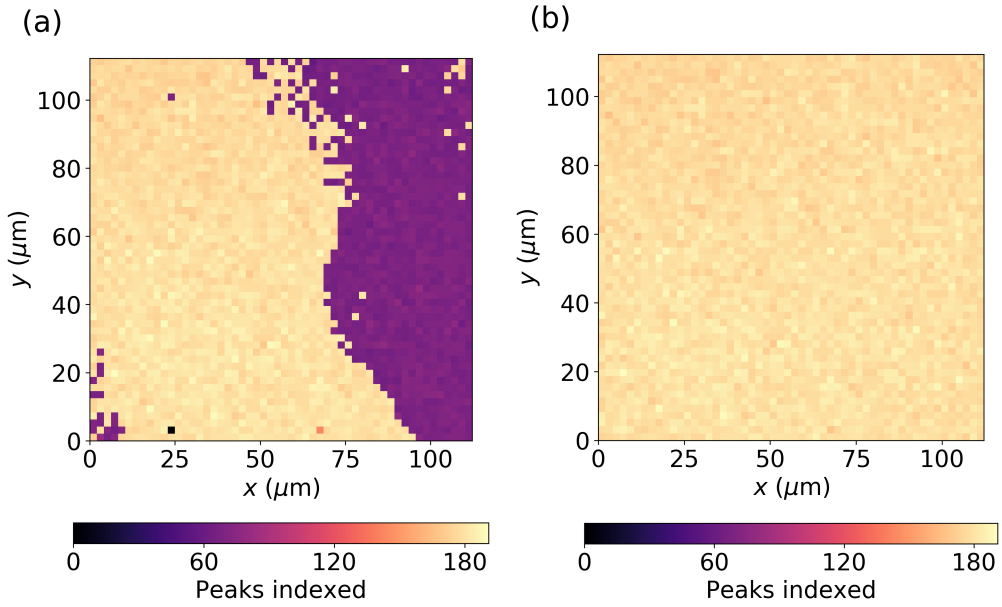

Figure 3.1: Comparison of the number of peaks successfully indexed on a 2 μm-resolution map of α-$RuCl_3$, with angular tolerance set to 0.08 degrees in (a) and to 0.05 degrees in (b). Without a strict tolerance setting the cluster fit converges to a suboptimal result on a large fraction of the map.

maps of the same sample (see Sec. 3.3.2). Time permitting, once the top priority map has been collected, it is also a good idea to do at least one higher-resolution scan, with the step size decreased by a factor of 5−10. This can help with later investigation of unexpected observations, for instance to determine if they are the result of aliasing.

It is worthwhile to take the time to collect a calibration pattern using crystalline Si. Its high symmetry makes the process of determining the correct detector geometry described in Sec. A.1 much more straightforward. If this step is omitted, the beamline scientist may be able to supply a copy of another user's Si calibration pattern taken just before or just after the beamtime in question.

Finally, one useful feature of the beamline software is the ability to program multiple scans to run sequentially. This can allow the user to get some valuable rest, and significantly reduce the stress of beamtime. Of course, there is a tradeoff: if the cyclotron goes down, or if the beam steering wanders particularly far, when the user returns to the beamline they will have to quickly assess what data is missing and needs to be retaken, and potentially reprioritize due to lost time. If this feature is to be used, the beamline scientist can help automate a sequence of several multi-hour maps.

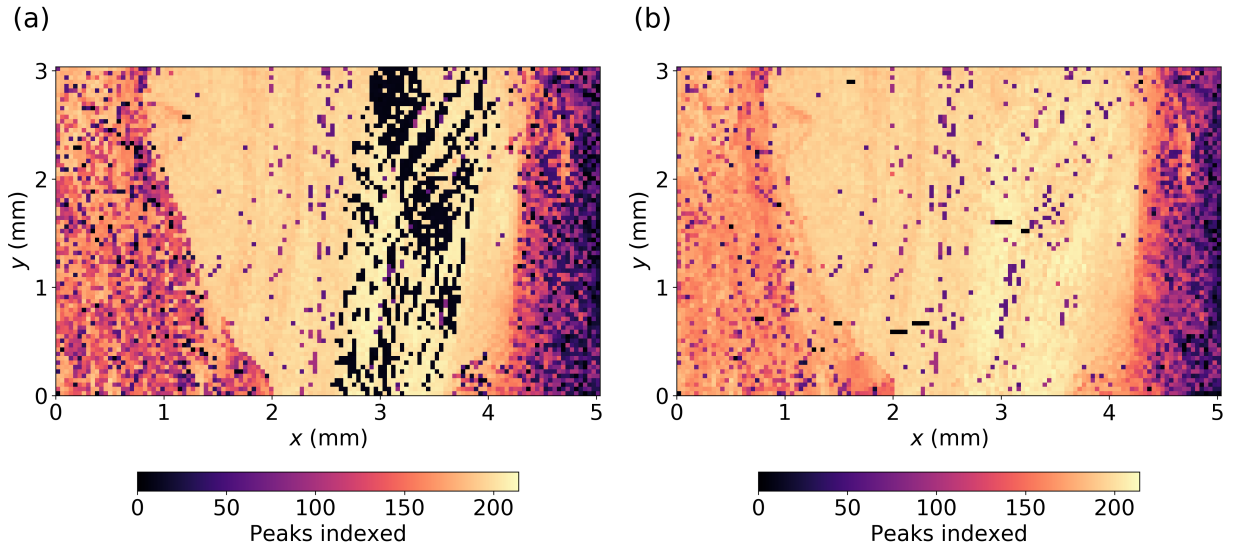

Figure 3.2: Comparison of cluster fit results on a 40 μm-resolution map of α-$RuCl_3$, with single-grain indexing in (a) and multi-grain indexing in (b). Multi-grain indexing fills in substantial regions of failing fits, leaving only isolated pixels where the indexing does not converge correctly.

3.3 Data analysis

The raw data making up one micro-Laue map can easily exceed 100 GB. There is a huge amount of potentially useful information contained in these images, but without careful analysis much of that information can remain hidden. In this section we review some of the most important techniques that we have developed and parameter choices that we have identified to optimize this information extraction process. We assume a basic familiarity with both the `XMAS` desktop software and its cluster implementation (and the associated `NERSC` file, which contains parameter definitions for cluster indexing). Appendix A contains more information on these, including a detailed walkthrough of the analysis procedure from start to finish.

3.3.1 Optimizing `XMAS` fits

In the course of our micro-Laue analysis work we have identified a few steps that are both 1) particularly useful for speeding up the indexing process or improving the fit results, and 2) somewhat unintuitive, and prone to being overlooked by a new user.

The most important single parameter we have identified is the angular tolerance, which is the maximum angular distance by which a peak's position can differ from its predicted position while still counting the peak as successfully indexed. This parameter is named `CALIB_XRES__` in the `NERSC` file. With a properly calibrated geometry configuration, using

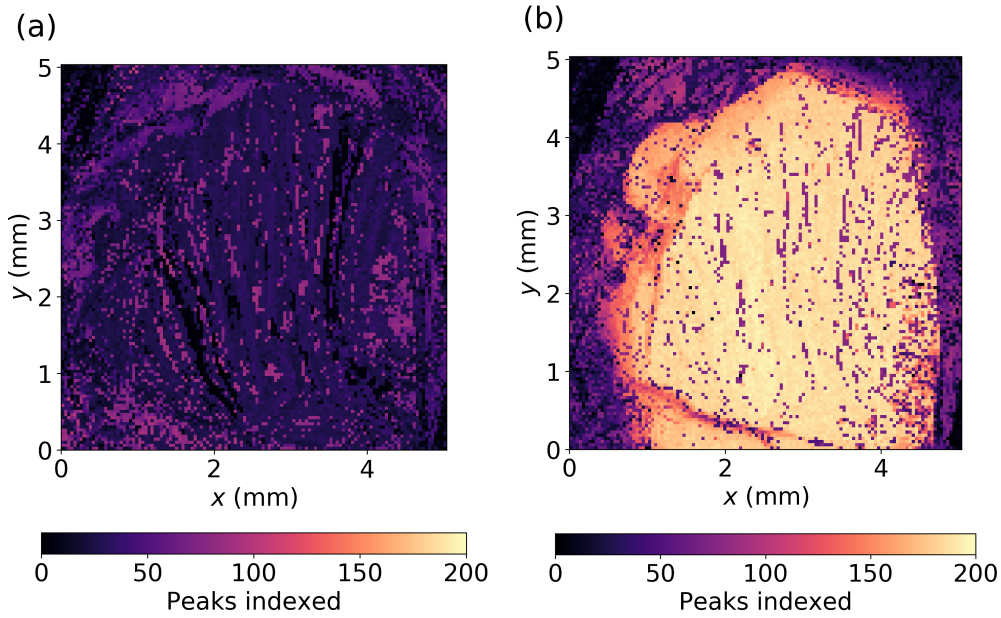

Figure 3.3: Comparison of cluster fit results on a 40 μm-resolution map of strained α-$RuCl_3$, with default geometry (a) and iteratively refined geometry (b). The indexing based on the unrefined unit cell completely fails, and when the input unit cell closely approximates the actual unit cell geometry the indexing is successful on the entire sample.

tight tolerances will help prevent the Laue indexing algorithm from converging to an incorrect fit. Empirically, this seems to be especially important if several peaks are overloaded. The practical difference between 0.05 degrees and 0.08 degrees is considerable. Figure 3.1 demonstrates the effect of reducing the tolerance from 0.08 degrees to 0.05 degrees; the regions of failed indexing (purple) that cover nearly half the map in Fig. 3.1(a) are completely eliminated when the tolerance is decreased.

It can also be helpful to perform multi-grain indexing rather than the default single-grain indexing. In this approach, after indexing a diffraction pattern, the algorithm excludes the indexed peaks and attempts to index the remaining peaks. This effectively gives the indexing algorithm another chance when the first fit fails. By choosing the fit result with the maximum number of indexed peaks we can significantly improve the reliability of the indexing, as shown in Fig. 3.2. In order to activate multi-grain indexing on the cluster, the `NERSC` file parameter `SINGLEMULTIT` must be set to 1, and `CALIB_MULTIG` and `MAXNUMBGRAIN` must be set to the number of grains to fit; 3 is a good choice.

Another good option is to use a small starting set in the Laue indexing process if the diffraction pattern to be indexed is relatively simple (i.e., single crystal). A value of 10 is a good choice; in general, one should increase the starting set only as much as necessary in order for the indexing to succeed reliably. This speeds up the fitting considerably; using a 20-peak starting set tends to take more than twice as long as a 10-peak set, and potentially

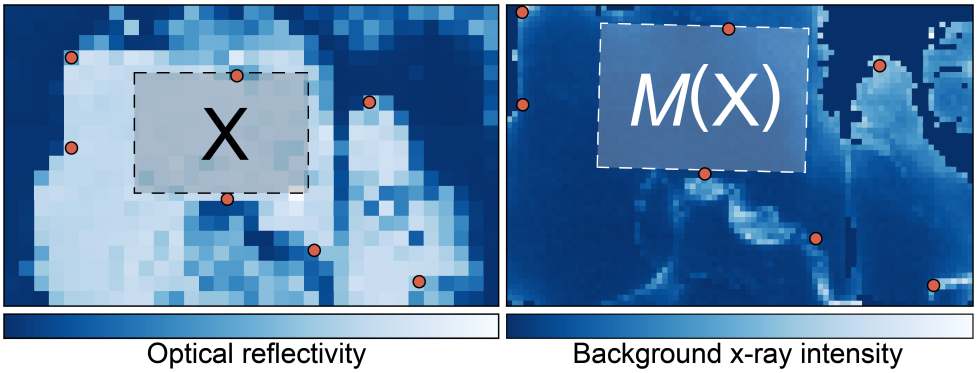

Figure 3.4: Large-scale maps of reflectivity (left) and background x-ray intensity (right) on an optimally doped P:Ba122 sample. Shared features used as landmarks are marked by orange circles, and their coordinates are used to fit for a similarity transformation M from the pump-probe region X to the corresponding subregion of the strain map, $M(\mathrm{X})$.

significantly longer when the indexing is unsuccessful. Due to the two-hour time limit for cluster jobs, this speedup can be quite important.

Finally, when attempting to index a crystal with a significant average strain or deformation, the indexing algorithm can run into trouble. In these cases it can be extremely helpful to focus on one image, manually index it as well as possible, and refine the strain parameters. This strain refinement can then be used to define a new unit cell geometry, which can form the basis of a fresh indexing attempt. By iterating this indexing and refinement procedure the fit results should improve significantly as the input crystal file converges to the deformed geometry of the sample. When updating the crystal file it is only necessary to change the lattice parameters; the symmetry information can be left unchanged. Once the indexing is working well, the deformed crystal file can be used as the basis for a cluster analysis of the entire map. Figure 3.3 shows an example of the indexing improvement due to this method on an α-$RuCl_3$ sample.

3.3.2 Aligning Laue maps to optical maps

The photomodulation and micro-Laue experiments are performed in different facilities and thus with slightly different sample orientations. Care is necessary to ensure that we compare the optical map with the correct subregion of the strain map. Figure 3.4 shows large-scale images of reflectivity (left) and background x-ray intensity (right) on an optimally doped P:Ba122 sample, with shared features on the sample surface marked by orange circles. After landmarking the images in this fashion, we fit for a mapping M (specifically, a similarity transformation) from the region corresponding to the photomodulation map, X, to the corresponding region on the strain map, $M(\mathrm{X})$. The alignment of various features shown in Fig. 3.5, which displays optically observed nematicity in panel (a) and strain quantities defined in Sec. 3.1.1 in panels (b-d), indicates that this procedure was successful.

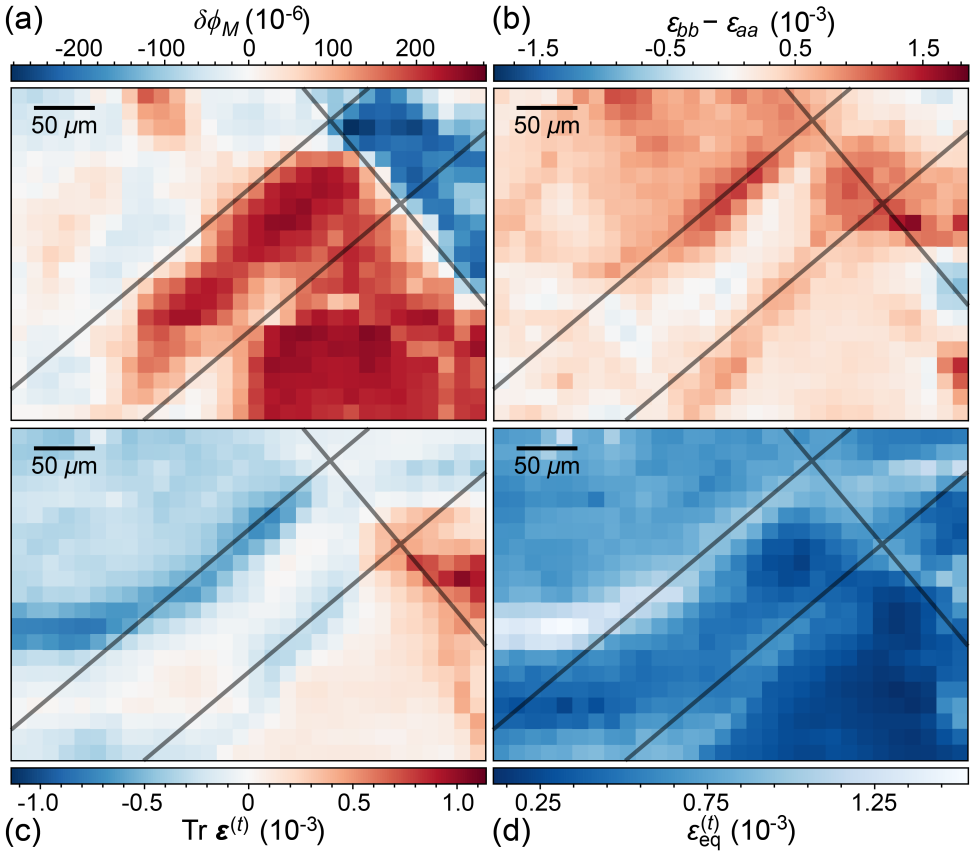

Figure 3.5: Spatial variation (13 μm resolution) of optical anisotropy (a) and ab-plane strain (b-d) on a 390×260 μm region of an optimally doped P:Ba122 crystal mounted on Cu. (a) Photomodulation proxy for nematic order, $\delta\phi_M$. (b) Transverse strain anisotropy $\varepsilon_{bb} - \varepsilon_{aa}$ in the Fe−Fe basis. (c) Transverse unit cell dilation $\mathrm{Tr}\,\boldsymbol{\varepsilon}^{(t)}$. (d) Transverse equivalent strain $\varepsilon_{\mathrm{eq}}^{(t)} = (2\varepsilon_{ij}^{(t)}\varepsilon_{ij}^{(t)}/3)^{1/2}$. Superimposed lines are parallel to the Fe−Fe directions and are located at the same positions in each image to facilitate visual comparison of features. Optical data were collected at $T = 5$ K; strain data at room temperature.

3.4 Twin peaks: domain fingerprinting in α-$RuCl_3$

In this section we focus on a specific data analysis application: measuring the domain composition of an α-$RuCl_3$ crystal. This material has a $C2/m$ crystal structure consisting of honeycomb ab plane layers stacked monoclinically with a per-layer shift of $-\boldsymbol{a}/3$ in the c-direction. Large samples of α-$RuCl_3$ tend to be multi-domain, with the direction of the stacking varying by an angle $2\pi/3$ in different regions. This multi-domain character has important implications for the magnetic properties of the material [35].

The basic approach is as follows: we begin with a standard indexing of the crystal using the `XMAS` desktop and cluster software, as described in Sec. 3.3.1 and in Appendix A. This

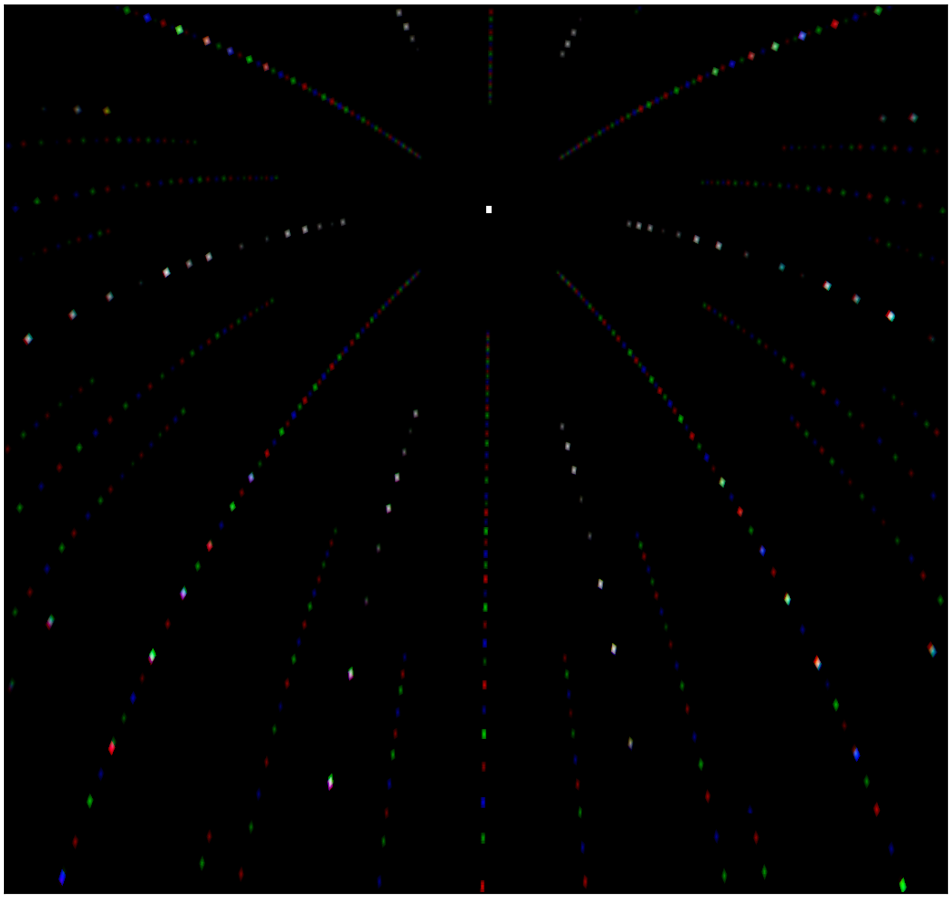

Figure 3.6: Simulated Laue diffraction patterns for three monoclinic α-$RuCl_3$ domains. The intensities in the red, green, and blue channels are the predicted x-ray intensities in the three domains with logarithmic scaling. Bright red, green, or blue peaks are fingerprint candidates.

indexing returns, among many other quantities, the unit cell vectors $\boldsymbol{a}$, $\boldsymbol{b}$, and $\boldsymbol{c}$ in the sample frame. This gives us the orientation of the dominant domain at each pixel, from which we can extract a unit vector normal to the ab plane, $\hat{\boldsymbol{n}}$. We can then determine the unit cell vectors corresponding to the other monoclinic domains by rotating e.g. $\boldsymbol{a}$ about $\hat{\boldsymbol{n}}$ by $\pm 2\pi/3$. Using the three domain orientations, we can predict the position of certain "fingerprint" peaks, unique to each domain, in the diffraction pattern. We define the total intensity $I^{(d)}$ as the sum of the x-ray intensity near the fingerprint locations corresponding to domain d, minus a correction accounting for background intensity. Then, defining $I_0^{(d)}$ as the predicted total intensity for domain d based on the Laue simulation, we can determine the relative compositions of the three monoclinic domains by comparing $I^{(d)}/I_0^{(d)}$, which we denote by $I_{\text{rel}}^{(d)}$.

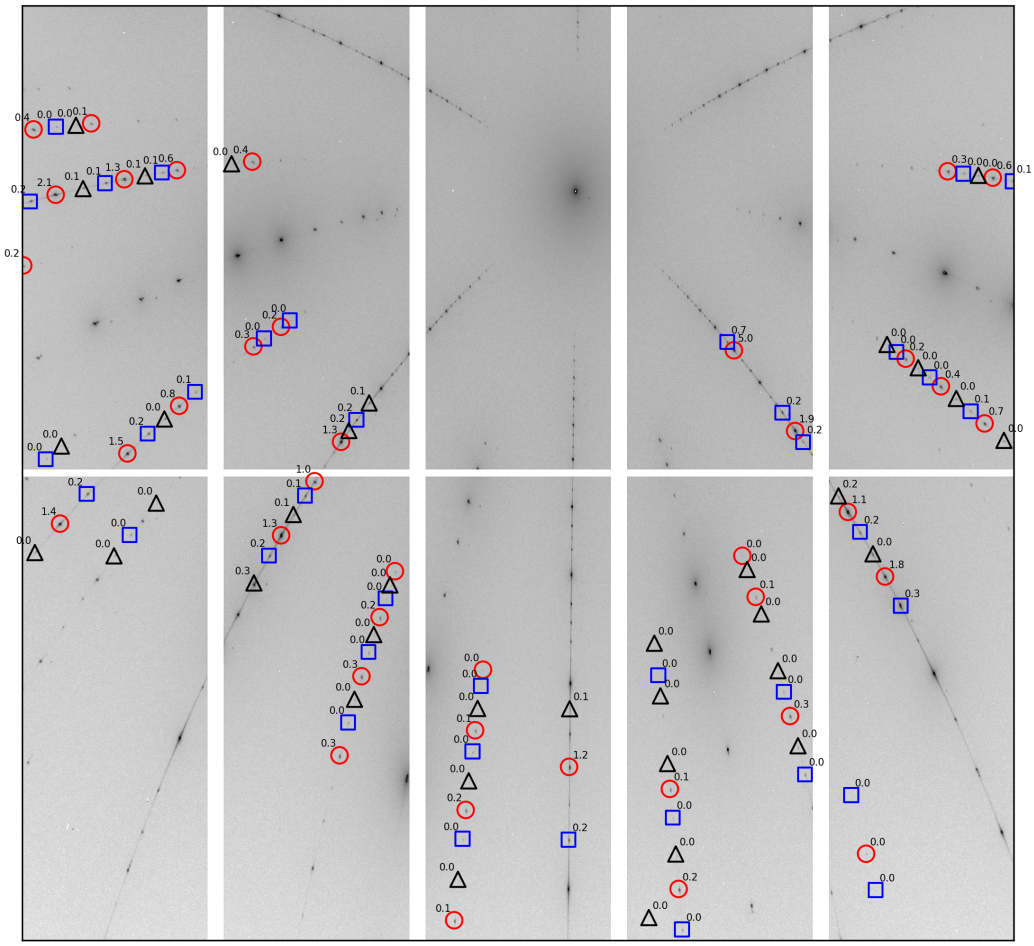

Figure 3.7: Example of domain fingerprinting in α-$RuCl_3$. The fingerprint peaks for the three monoclinic domains are marked by red circles, blue squares, and black triangles. The ratio of measured to predicted intensity for each peak is inscribed adjacent to the peak.

3.4.1 Simulating Laue images in XMAS

In order to identify the diffraction peaks that are unique to the monoclinic domains, we use the XMAS desktop software's built-in diffraction pattern simulation capability, accessed via `Utilities` → `Simulate Laue pattern image`. Once we have loaded a crystal structure corresponding to the crystal we want to simulate (see Sec. A.1), we simply enter the *hklxyz* matrix, which is the inverse of the 3×3 matrix whose rows are $\boldsymbol{a}$, $\boldsymbol{b}$, and $\boldsymbol{c}$ in the sample frame. When attempting to reproduce experimental results, it is important to note that the Laue simulation process uses the current geometry configuration to predict the peak positions, so this configuration must be up to date. Figure 3.6 shows an example of simulated Laue patterns for three monoclinic α-$RuCl_3$ domains, with the red, green, and blue channel intensities representing (the logarithm of) the x-ray intensity. Red, green, and blue peaks

each correspond to a particular domain.

When saving a simulated Laue pattern for use in analysis via `File` → `Save...` → `Image`, it is important to use the Pilatus `.tif` file format. All other formats only have 8-bit precision, i.e., 256 intensity levels, which is insufficient to capture the dynamic range of a typical Laue pattern, while the Pilatus `.tif` format has 16-bit precision (256^2 intensity levels). In order to save a simulation as a Pilatus `.tif` we must first load a data image and then generate the simulation on top of the data. If we then generate a second simulation, we will be unable to save the resulting image; loading a data image and generating the new simulation will solve the problem.

After simulating the diffraction patterns corresponding to the three monoclinic domains, the fingerprint peaks are identified by two obvious criteria: a fingerprint peak for e.g. domain 1 should have reasonably high intensity in the domain 1 simulation, and the corresponding region in the other simulations should be dark.

The α-$RuCl_3$ crystal structure is invariant under rotation by π about the b-axis, which maps $(h, k, l) \to (-h, k, -l)$, and under reflection $b \to -b$, which maps $(h, k, l) \to (h, -k, l)$. This means that for a perfect crystal the diffraction peak (h, k, l) is physically indistinguishable from $(h, -k, l)$, $(-h, k, -l)$, and $(-h, -k, -l)$; that is, the only meaningfully different peaks are $(\pm h, k, l)$. Thus, for any peak that is identified as a fingerprint peak, we should also include the other three indistinguishable peaks. This makes the list of fingerprint peaks much more generally applicable to other samples in different orientations.

Figure 3.7 shows an example diffraction pattern from α-$RuCl_3$, with the fingerprint locations for the three monoclinic domains marked. The intensity of each peak relative to its predicted intensity based on an equal combination of all three domains is inscribed adjacent to its marker. Relative to the ratio of measured to predicted total intensity $I_{\text{rel}}^{(1)}$ of the first, dominant domain (marked by red circles), the integrated intensities of domain two (blue squares) and domain three (black triangles) are $I_{\text{rel}}^{(2)} = 0.14 I_{\text{rel}}^{(1)}$ and $I_{\text{rel}}^{(3)} = 0.09 I_{\text{rel}}^{(1)}$, respectively. The subdominant domains are observed, but much more weakly than the dominant domain.

Chapter 4

Initial optical study of nematicity in $BaFe_2(As,P)_2$

4.1 Introduction

The Fe-pnictide system $BaFe_2(As_{1-x}P_x)_2$ (P:Ba122) has been the focus of significant attention because of its apparent quantum critical behavior near optimal doping and because the isovalent substitution of As for P leads to a superconducting phase with less disorder than doping on the Fe site, as illustrated by the observation of quantum magneto-oscillations [36]. Given that P:Ba122 is a low-disorder model system for testing the quantum critical paradigm, it is important to further probe the phase diagram near the critical P concentration. Here we present measurements of birefringent reflectivity, the difference in optical reflection coefficient for light polarized parallel to the two orthogonal Fe-Fe bond directions, in a series of P:Ba122 samples in which x spans x_c. Two methods for detection of optical birefringence were used in this work. To maximize the sensitivity to temperature dependence of order parameters, we used a photomodulation (or pump/probe) technique in which a weak laser pulse perturbs the equilibrium reflectance R and the subsequent change in reflectance, ΔR, is measured by a time-delayed probe pulse. Both pump and probe pulses are centered at a wavelength of 800 nm (photon energy 1.55 eV) and were focused to a spot of diameter 75 μm at the sample surface. In the measurements reported in this chapter, ΔR is independent of pump polarization and linearly proportional to the energy u that is absorbed from the pump pulse. In discussing the results we focus on $\Delta R_a(t) - \Delta R_b(t)$, where $\Delta R_a(t)$ and $\Delta R_b(t)$ are the modulation of reflectivity measured with the probe linearly polarized along the two orthogonal (a and b) Fe-Fe bond directions. In the second method we used a scanning confocal Kerr microscope operating at 633 nm (photon energy 1.96 eV) to produce maps of $\Re[(r_a - r_b)/(r_a + r_b)]$, where $r_{a,b}$ are equilibrium reflection coefficients parallel to the a, b directions, with 8 μm spatial resolution over a 300 μm $\times$ 300 μm field of view.

The photomodulation technique that we used in these experiments is introduced in Sec. 2.1.1. Section 4.2 presents results on the spatial, temperature, and time-dependence

of $\Delta R_{a,b}$ for P:Ba122 samples that span the critical P concentration. Two results relevant to quantum critical scenarios are, first, the observation that C_4 symmetry is broken in crystals for which $x > x_c$; that is, materials found by bulk probes to be tetragonal at all temperatures. Second, in this range of x the sign of $\Delta R_a(t) - \Delta R_b(t)$ reverses at the superconducting transition temperature. Section 4.3 focuses on the interpretation of these observations. These data suggest that C_4 symmetry breaking at $x > x_c$ reflects the combined effects of strain, divergent nematic susceptibility, and magneto-nematic coupling, leading to a large shift towards higher x of the line of magnetic phase transitions, $T_M(x)$; this hypothesis is tested in the following chapter. We interpret the change in sign of optical birefringence in these samples in terms of dynamic competition in the time domain between superconductivity and C_4-breaking order. Finally, Section 4.4 presents a summary of our experimental observations and modeling, and indicates goals for future measurements.

4.2 Results

4.2.1 Spatial dependence

Measurements of photomodulated reflectance were performed using 100 fs-duration pulses from a mode-locked Ti:Sapphire laser at 80 MHz repetition rate, 800 nm center wavelength, and 1 μJ cm^{-2} fluence focused to a 75 μm diameter spot. The results described below were obtained on crystals that were not deliberately strained. Structural phase transitions in unstrained Fe-pnictides are known to give rise to orthorhombic domains [37]. On the basis of reports that the typical domain size is in the $1 - 10$ μm range [37, 38], we expected the photomodulated optical reflectivity to be uniform and isotropic when probed on the 100 μm scale. However, our initial measurements showed strong dependence of the amplitude, and even the sign, of ΔR on the position of the laser beam focus on the sample. To characterize the spatial inhomogeneity we registered each position on the sample under study with respect to an optical landmark on the sample mount using a high-resolution video feed, allowing us to define beam position to a precision of 5 μm, which is small compared to the 75 μm focal diameter. We then used this optical landmarking capability to generate maps of the spatial variation of ΔR.

Figure 4.1**A** shows a picture of an underdoped ($x = 0.24$) sample overlaid with a false-color map of the amplitude of ΔR near zero time delay, measured in the orthorhombic phase at $T = 25$ K with the polarization of the pump and probe beams fixed parallel to the (orthogonal) Fe-Fe bond directions that define the a and b axes. In the red regions $\Delta R_a > \Delta R_b$, and in the blue regions $\Delta R_a < \Delta R_b$.

The contrast displayed in Fig. 4.1**A** suggests the existence of relatively large regions, of order 100 μm, where one orientation of the orthorhombic axes is predominant. This result is surprising, as domain imaging by polarized optical and scanning SQUID microscopies [37, 38] sees twin domains with length scale of order 10 μm. If the entire sample was populated by domain boundaries at this density, we would expect to observe only a

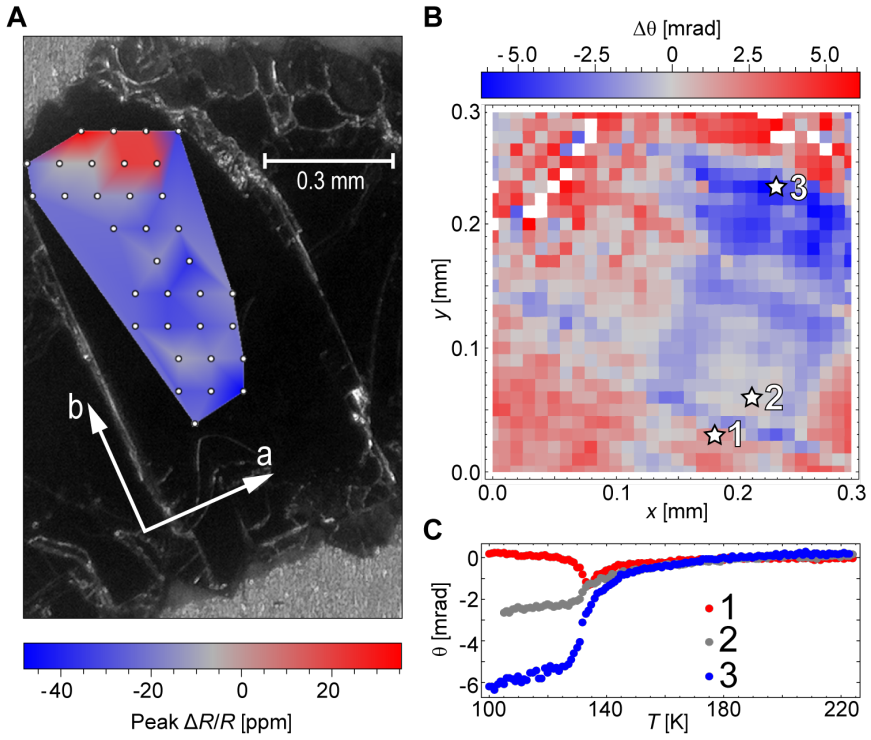

Figure 4.1: Optical mapping of orthorhombic domain in underdoped P:Ba122. **A**: Spatial variation of $\Delta R/R$ near zero time delay in $BaFe_2(As_{1-x}P_x)_2$ with $x = 0.24$ at $T = 6$ K, overlaid on an optical image of sample. Open circles indicate points where data were collected. **B**: Spatial variation of change in equilibrium birefringence between 120 K and 160 K in a sample with $x = 0$. **C**: Temperature dependence of equilibrium birefringence at the spots marked in **B**, showing transitions in twinned domains.

small and randomly fluctuating birefringence when probing with 75 μm spatial resolution. To further investigate the domain size, we used a cryogenic scanning Kerr microscope to obtain equilibrium birefringence images with 8 μm resolution. Figure 4.1**B** shows one such map of a 300 μm $\times$ 300 μm region of the surface of $BaFe_2As_2$; the false color represents the birefringence amplitude at 120 K, with a map of the same region measured at 160 K subtracted to remove the contribution of the cryostat window. This map shows that in addition to regions with high twin density, there exist relatively large areas with predominately a single orientation of the orthorhombic axes, consistent with the PM response obtained with a 75 μm laser spot. Figure 4.1**C** shows the temperature dependence of the Kerr signal at the three points marked in Fig. 4.1**B**, showing the characteristic, distinct behaviors for pure domains (of both signs) and mixed regions.

The existence of domains is anticipated for underdoped samples such as the ones described above, as they are known to undergo a tetragonal to orthorhombic phase transition with decreasing temperature. However, we found large domains of optical birefringence as

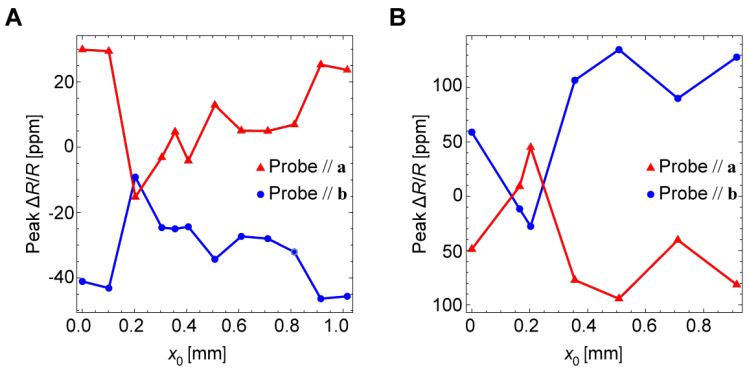

Figure 4.2: Spatial dependence of $\Delta R/R$ near zero time delay in an optimally doped sample ($x = 0.31$) at $T = 22$ K (**A**) and $T = 6$ K (**B**). The sign and magnitude of $\Delta R/R$ vary strongly with position, and changes sign under rotation of the linear probe polarization from the a crystal axis to the b axis.

well in samples with $x > 0.28$, in which bulk probes indicate that the low-temperature phase is tetragonal and superconducting rather than orthorhombic and antiferromagnetic. Figures 4.2**a** and **B** show line cuts of $\Delta R/R$ vs. position for probe polarization parallel to the a and b axes for a sample with $x = 0.31$, measured just above the superconducting transition and at 6 K, respectively. These position scans reveal extended regions of strong optical birefringence at both temperatures. Another notable feature is that the sign of the birefringence, i.e., $\Delta R_a - \Delta R_b$, reverses upon cooling from the normal to the superconducting phase. We return to a discussion of these features in Section 4.3.3.

4.2.2 Time and temperature dependence of ΔR

To measure the time and temperature dependence of ΔR we used our landmarking capability to locate the probe beam on a fixed spot in a homogeneous region as we varied T. Figure 4.3**A** shows ΔR vs. time delay, t, measured on a sample with $x = 0.14$ for temperatures in the range 5 K $<$ T $<$ 200 K, with the sample position fixed as described above. The two sets of traces in Fig. 4.3**A** were measured with the probe beam polarized parallel to the two Fe-Fe bond directions, arbitrarily labeled 𝕒 and 𝕓. To better illustrate singular features in the temperature dependence of the PM signal, we plot the peak amplitude of ΔR vs. T for the two sets of curves in Fig. 4.3**B**. With decreasing temperature, ΔR first appears above the noise level at $T \approx 160$ K and increases gradually, with a growing contrast between the response in the 𝕒 and 𝕓 directions. With further cooling there is an abrupt onset of an additional PM signal near 95 K that is negative for both directions of probe polarization.

In the context of Section 2.1.1, we note that the P:Ba122 system exemplifies a metal in which ΔR arises from the perturbation of order parameters, rather than changes in electron occupancy of a static band structure. The onset of a PM signal near 160 K coincides with the onset of birefringence (i.e., $\Delta R_a \neq \Delta R_b$, indicating that ΔR arises from an order parameter

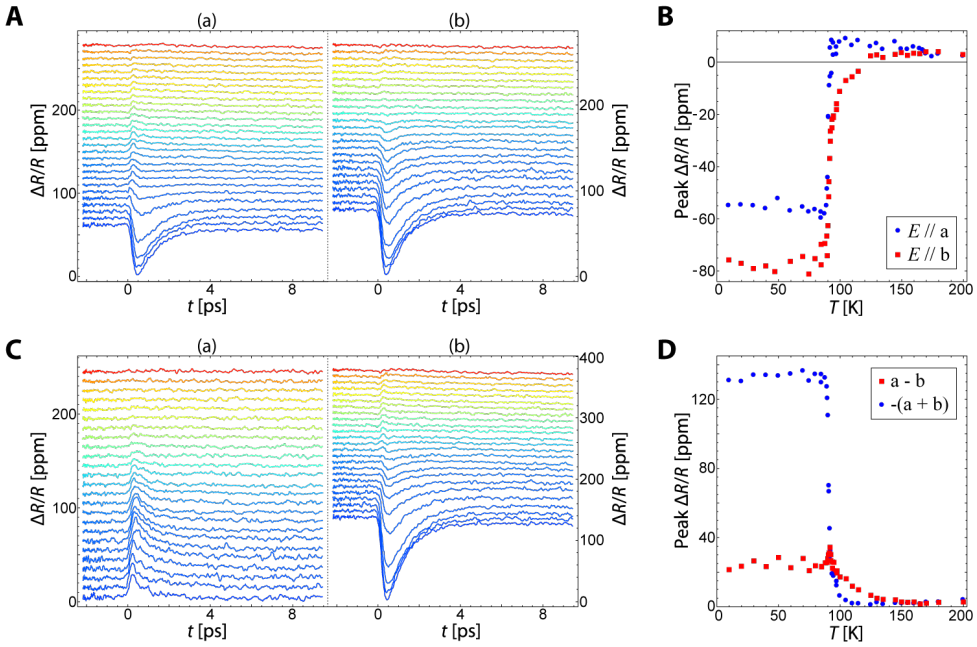

Figure 4.3: Time and temperature dependence of $\Delta R/R$ in $BaFe_2(As_{1-x}P_x)_2$ with $x = 0.14$. **A** and **C** show $\Delta R(t)/R$ between 5 K and 200 K in equal temperature intervals. In **A** probe polarization is parallel to the a (frame (a)) and b (frame (b)) crystal axes. **B**: Temperature dependence of the maximum value of $\Delta R(t)/R$ with probe parallel to a (blue circles) and b (red squares). **C**: Symmetrized and antisymmetrized responses generated from the sum (frame (a)) and difference (frame (b)) of the curves shown in **A**(a) and (b). **D**: Temperature dependence of the maximum value of $\Delta R(t)/R$ for the symmetrized (blue circles; shown with an overall factor of -1 for ease of comparison) and antisymmetrized (red squares) curves shown in **C**.

that breaks C_4 symmetry. Given that the PM response is a result of photomodulated order, Eq. 2.1 is relevant for interpretation of the T dependence shown in Fig. 4.3**B**. In particular, it is significant that $\Delta R_a(T)$ and $\Delta R_b(T)$ are not proportional, indicating that the response does not arise from photomodulation of a single form of order. We return to this point below when we discuss the PM response of the entire set of samples.

To focus on the breaking of C_4 symmetry, we calculate $\Delta R_a \pm \Delta R_b$, the sum and difference of signals measured along the two principal axes. The dependence of $\Delta R_a + \Delta R_b$ and $\Delta R_a - \Delta R_b$ on time delay is plotted Fig. 4.3**C** and their corresponding peak amplitudes are shown in Fig. 4.3**D**. From the amplitude of $\Delta R_a - \Delta R_b$ it is apparent that C_4 symmetry is broken well above the structural transition temperature, T_s, of 95 K. Beginning at approximately 160 K, $\Delta R_a - \Delta R_b$ increases smoothly with decreasing temperature until T_s, where it exhibits a cusp-like singularity. In contrast, $\Delta R_a + \Delta R_b$ exhibits a sharp step at T_s (width less than 1 K), suggesting that it is proportional to the magnetostructural order known to onset in a first-order transition (we have reversed the sign of $\Delta R_a + \Delta R_b$ to facilitate comparison with

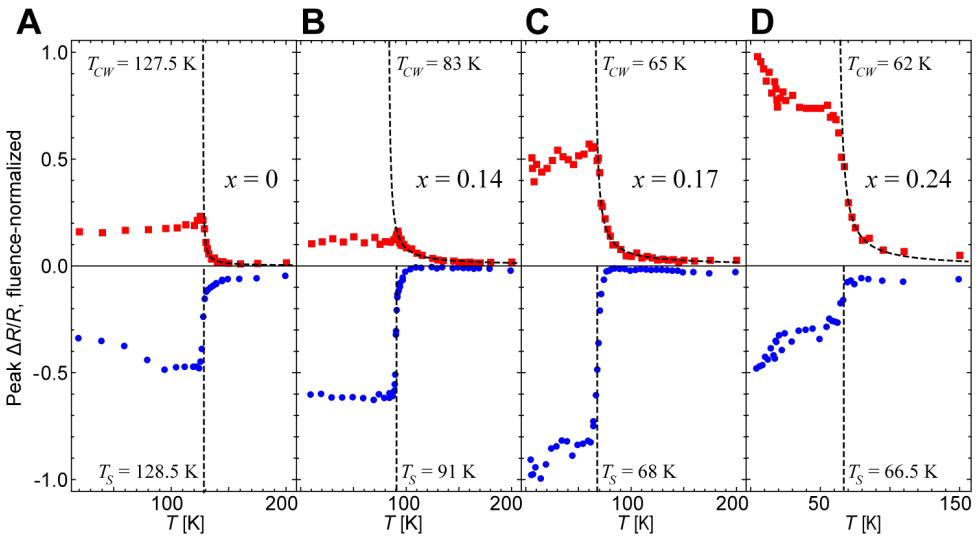

Figure 4.4: Temperature dependence of the peak symmetrized (blue circles) and antisymmetrized (red squares) response in underdoped samples, with **A**-**D** showing $x = 0$, $x = 0.14$, $x = 0.17$, and $x = 0.24$ respectively. Dashed lines in the upper panels are Curie-Weiss fits to the antisymmetrized data; dashed lines in the lower panels indicate the temperature of the step-like variation the symmetrized data; the Curie-Weiss temperatures obtained from the fits and the temperatures of the jumps in symmetrized data are shown in each panel.

$\Delta R_a - \Delta R_b$).

Underdoped samples: $x \leq 0.24$

Figures 4.4**A**-**D** present the symmetrized and antisymmetrized PM amplitudes ($\Delta R_a \pm \Delta R_b$) for a set of samples that includes the one whose PM response is shown in Fig. 4.3 (x equal to 0, 0.14, 0.17, and 0.24, respectively). The data have been normalized by fluence and scaled to the maximal amplitude. All samples exhibit C_4 breaking with a smooth onset at temperatures above T_s as well as a step-like change in PM response at the magnetostructural transition.

Optimally doped sample: $x = 0.31$

We turn next to the time and temperature dependence of the PM response in a sample of P:Ba122 with P concentration equal to 0.31, which are plotted in Fig. 4.5. At this value of x bulk probes find a low-temperature phase that is tetragonal and superconducting. However, the PM signal indicates that C_4 symmetry is broken at low temperatures. Optical birefringence onsets at approximately 60 K, with a discontinuous change in the slope of $\Delta R_a - \Delta R_b$ as a function of temperature. With further cooling the sign of the T derivative of the birefringence changes abruptly near the onset of superconductivity, and at low temperature

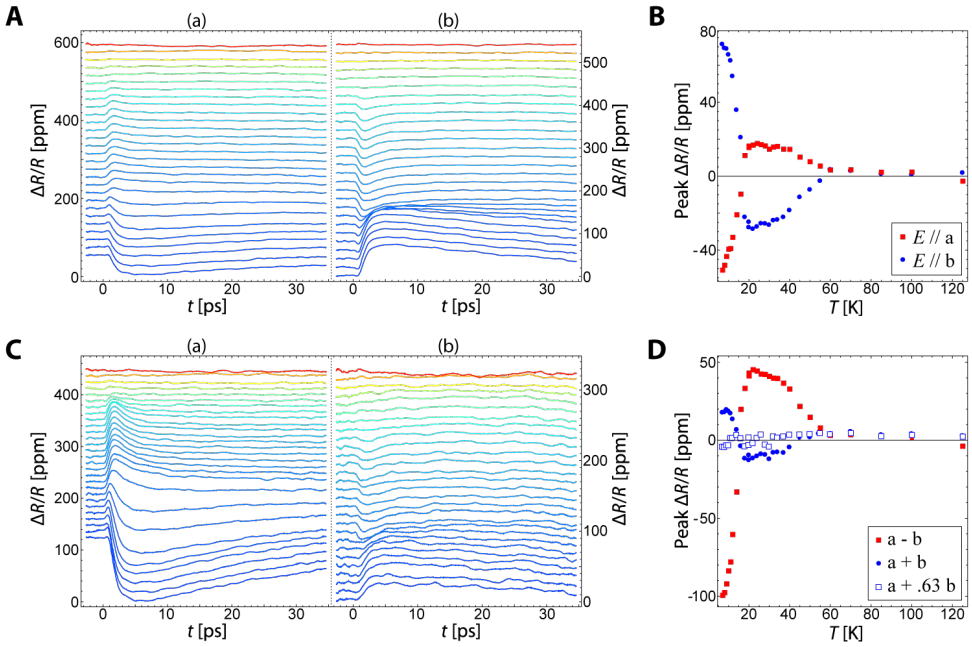

Figure 4.5: Time and temperature dependence of $\Delta R/R$ in the $x = 0.31$ sample. **A**: Time dependence of $\Delta R/R$ response with probe polarization parallel to the crystalline 𝕒 (frame (a)) and 𝕓 (frame (b)) axes between 5 K and 125 K. **B**: Temperature dependence of the peak $\Delta R/R$ response with the probe parallel to 𝕒 (blue circles) and 𝕓 (red squares). **C**: Time dependence of the antisymmetrized (frame (a)) and symmetrized (frame (b)) response between 5 K and 125 K. **D**: Temperature dependence of the peak symmetrized (solid blue circles) and antisymmetrized (red squares) response, along with $\Delta R_a + 0.63\Delta R_b$ (open blue squares). The proximity of $\Delta R_a + 0.63\Delta R_b$ to zero across the measured temperature range demonstrates that $\Delta R_a(T) \approx -0.63\Delta R_b(T)$.

the sign of $\Delta R_a - \Delta R_b$ is reversed relative to the normal state. We note that, despite the appearance of two singular features in the temperature dependence (and therefore evidence for two phase transitions), ΔR_a is proportional to ΔR_b over the entire temperature range, obeying $\Delta R_a \approx -0.63\Delta R_b$. We highlight this feature of the data by plotting the peak of $\Delta R_a + 0.63\Delta R_b$ as open symbols in Fig. 4.5**D**; this quantity remains close to zero throughout the full range of temperature. In the context of Eq. 2.1, the observation that $\Delta R_a \propto \Delta R_b$ indicates that the PM response in this sample should be attributed to photomodulation of a single form of order.

Overdoped samples $x = 0.37$, $x = 0.42$

Photomodulation measurements on overdoped samples, shown in Fig. 4.6, have significantly lower signal-to-noise than those reported on the underdoped and optimal crystals as a consequence of their smaller size and rougher surfaces. The overdoped crystals had typical

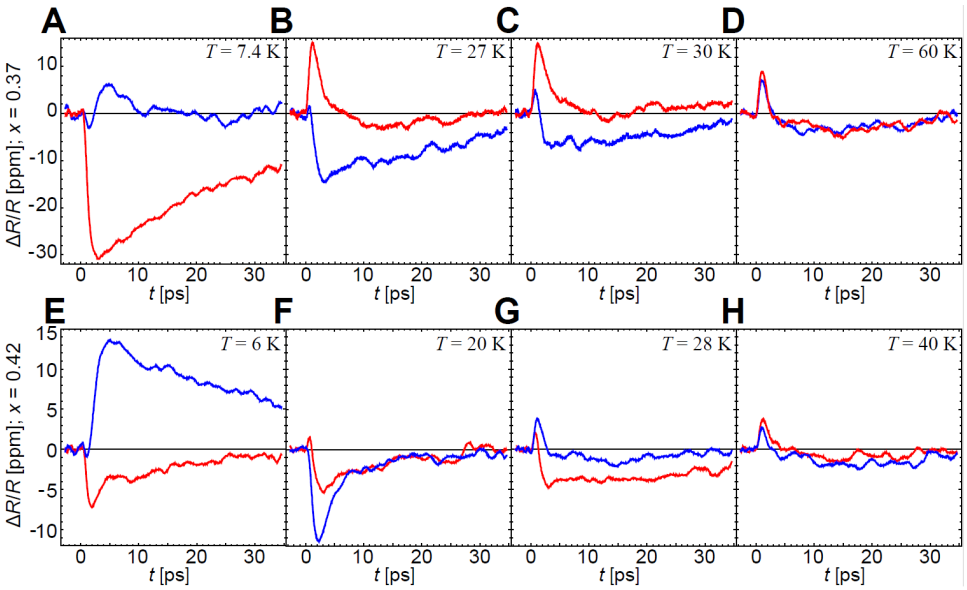

Figure 4.6: Raw time dependence of $\Delta R/R$ at select temperatures in the $x = 0.37$, $T_c = 27$ K (**A**-**D**) and $x = 0.42$, $T_c = 25$ K (**E**-**H**) samples. Birefringence is apparent both above and below the superconducting transition.

dimension 300 μm, as compared with the approximately 1 mm square underdoped and optimal crystals, leaving less opportunity to find single domain regions on the scale of the 75 μm beam focus. Despite these challenges, PM measurements on the overdoped samples yielded interesting information. Most notably, we observed birefringence above the superconducting critical temperature for both $x = 0.37$ and $x = 0.42$.

4.3 Discussion

4.3.1 Breaking C_4 at $T > T_s$ via residual strain for $x < 0.28$?

The smooth increase in birefringence with decreasing temperature in the samples with $x < 0.31$ suggests that this initial appearance of anisotropy in R is a consequence of strain imposed by differential thermal contraction rather than a phase transition. In the presence of uniaxial strain, δ, nematic order, and therefore ΔR would be proportional to $\chi_\phi(T)\delta$, where χ_ϕ is the nematic susceptibility. Although differential thermal contraction would induce biaxial strain, in the presence of large $\chi_\phi(T)$ a biaxial perturbation would tend to be accommodated by the formation of uniaxially strained regions.

The dashed lines in the upper panels of Fig. 4.3 show the resulting fits and the dashed lines in the lower panels indicate the steepest point of the step in $\Delta R_a(T) + \Delta R_b(T)$, which we take as a measure of T_s. For all samples in this doping range T_{CW} as determined from the Curie-Weiss fit is close to, but below, T_s. The quality of the fits and the consistency with

previous measurements of $\chi_\phi(T)$ suggest that the appearance of the birefringence above the nominal structural transition temperature is indeed associated with external strain.

4.3.2 Optimal sample: evidence for strain-induced phase transition

The direct evidence of C_4 symmetry in the optimally doped sample, as revealed by optical birefringence, is surprising given that other (mainly bulk) probes find that for $x > 0.28$, P:Ba122 remains tetragonal at all temperatures. As discussed above, the combination of large nematic susceptibility and biaxial strain can drive strong local C_4 breaking above a structural transition. However, the signature of such strain-induced symmetry breaking is that C_4 order onsets in a nonsingular fashion with a smooth Curie-Weiss temperature dependence. In contrast to this expectation, the onset of birefringence with decreasing temperature for the sample with $x = 0.31$ (see Figs. 4.5**b** and **d**) is quite abrupt and the T dependence cannot be fit with a Curie-Weiss (or any other) power law.

Given that the onset of birefringence is sharp, we consider a model in which the combination of strain, divergent nematic susceptibility, and magneto-nematic coupling induce a magnetic phase in samples that are paramagnetic in the absence of strain. A free energy, F, that includes these couplings has the following form:

$$F = a\left[T - T_M^0(x)\right] M_Q^2 + \frac{1}{2}\chi_\phi^{-1}\phi^2 - \lambda M_Q^2\phi - g\phi\sigma,$$

where a describes the strength of the magnetic phase with order parameter M_Q in the absence of strain, λ is the magneto-nematic coupling constant, and g describes the coupling of the nematic order to uniaxial strain, σ. In the absence of strain and magneto-nematic coupling, this form for F leads to a line of second-order magnetic phase transitions described by $T_M^0(x)$, which we assume to terminate at a critical P concentration, x_c^0. With application of strain, C_4 symmetry is broken externally, so there cannot be a nematic phase transition. However, an applied strain in the presence of magneto-nematic coupling will shift the magnetic phase boundary, given by

$$T_M(x) = T_M^0(x) + \chi_\phi\lambda g\sigma/a.$$

This shift is potentially quite large near the critical concentration because of the divergent nematic susceptibility, and could account for the observation of a magnetic phase at P concentrations above the nominal critical point.

4.3.3 Competition between superconducting and nematic order

Whatever the origin of C_4-breaking order at $x = 0.31$, the temperature dependence of the photomodulation (PM) amplitude shown in Figs. 1(b-d) and 3(d-e) indicates that the nematic order is strongly coupled with superconductivity. In this section we discuss the implications

of the sign change in $\delta\phi \equiv (\Delta R_b - \Delta R_a)/R$ near T_c, along with the fact that we generically observe proportionality $\Delta R_a(T) \propto \Delta R_b(T)$ at optimal doping.

In the presence of superconducting order, represented by ψ, and a C_4-breaking order ϕ, the pump-probe response includes contributions from both:

$$\begin{pmatrix} \Delta R_a \\ \Delta R_b \end{pmatrix} = (\alpha_e \mathbf{1} + \alpha_o \boldsymbol{\sigma}_z)\,\phi + (\beta_e \mathbf{1} + \beta_o \boldsymbol{\sigma}_z)\,|\psi|^2\,, \tag{4.1}$$

where $\mathbf{1}$ and $\boldsymbol{\sigma}_z$ are the unit and Pauli z matrices, respectively, and α_e and α_o (β_e and β_o) are coefficients describing the even and odd components, respectively, of ΔR under a $\pi/2$ rotation of probe polarization due to the pump-induced weakening of the ϕ (ψ) order. Equation 4.1 implies that the observed proportionality of $\Delta R_{a,b}$ for all T requires $\alpha_e/\alpha_o = \beta_e/\beta_o$; that is, that the ratio of symmetric and antisymmetric PM coefficients is the same for both forms of order. The microscopic origin of reflectivity modulation induced by distinct orders will differ, so this equality would be a significant coincidence. We hypothesize instead that the direct contribution of the pump-induced modulation of ψ is too small to observe; i.e., $\beta_e \approx \beta_o \approx 0$, so that even below T_c the pump-probe response arises exclusively from ϕ, and ψ is visible due to a repulsive interaction between the two phases of the form $\lambda\phi^2|\psi|^2$ in the Ginzburg-Landau free energy.

Above the superconducting transition, where $\psi = 0$, $\phi \neq 0$, the PM response can be described by the rate equation $\delta_t\phi = G(t) - \gamma(\phi - \phi_0)$, where G describes the pump-induced weakening of ϕ and γ is the rate at which it returns to its equilibrium value, ϕ_0. We assume that the system is in a linear regime where G is proportional to the laser fluence; G is also proportional to ϕ_0, as established in Sec. 5.4.2. In the short-pulse approximation, $G(t) = -F\phi_0\delta(t)$, where F is proportional to the number of photons in the pump pulse. Integrating the rate equation yields $\phi(t) = [1 - F\exp(-\gamma t)]\phi_0(T)$ for $t > 0$.

In the superconducting phase, the repulsive interaction energy $\lambda\phi^2|\psi|^2$ reduces the equilibrium order to $\phi_0(T) = \phi_0^*(T)(1 - 2\chi_\phi\lambda|\psi_0(T)|^2)^{-1}$, where ϕ_0^* is the order parameter amplitude in the absence of coupling to superconductivity, ψ_0 is the equilibrium value of the superconducting order parameter, and χ_ϕ is the nematic susceptibility. We assume that in the superconducting phase the pump pulse weakens both ϕ and $|\psi|^2$. Following photoexcitation, ϕ recovers not towards ϕ_0, but rather to a time-dependent quasi-equilibrium value $\phi_1(t)$, given by

$$\phi_1(t) \approx \phi_0\left(1 + \frac{2\lambda\chi_\phi\delta|\psi(t)|^2}{1 - 2\lambda\chi_\phi|\psi(t)|^2}\right),$$

which exceeds ϕ_0 because of the pump-induced weakening of the superconducting order, $\delta|\psi|^2$. In the presence of dynamic coupling, $\phi(t)$ will decay towards ϕ_1 rather than ϕ_0, according to $\delta_t\phi = G(t) - \gamma[\phi - \phi_1(t)]$.

Figure 4.7(a) compares the C_4-odd photomodulation response $\delta\phi$ measured at 14 K, 16 K, and 18 K with fits obtained by integrating the rate equation that accounts for coupled order. The quality of fit is excellent; in particular, the reversal of sign for $t \sim \gamma^{-1}$ is accurately

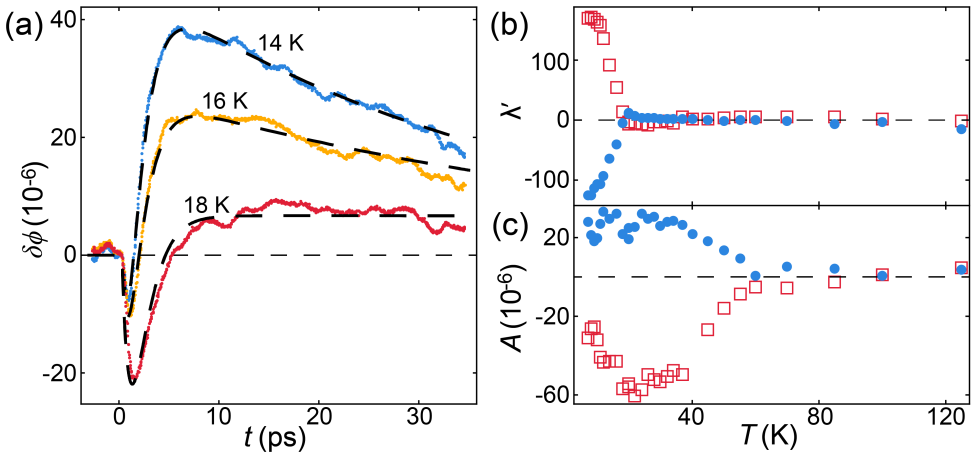

Figure 4.7: Fit results from a model wherein the suppression of the superconducting order parameter appears in $\delta\phi \equiv (\Delta R_b - \Delta R_a)/R$ only through the enhancement it induces in the nematic order parameter. (a) Example fits (dashed black) to the traces with $T = 14$ K, 16 K, and 18 K. (b) Temperature dependence of the fit parameter λ' corresponding to the amplitude of the superconducting response, with probe polarization parallel to the a axis (blue circles) and b axis (red squares). (c) Temperature dependence of the fit parameter A corresponding to the amplitude of the nematic response, with probe polarization parallel to the a axis (blue circles) and b axis (red squares).

reproduced. The fitted parameters are $\lambda' \equiv \lambda\chi_\phi(\phi_0^*/\phi_0)^2\delta|\psi(t)|^2$ and $A \equiv F\phi_0$, which are plotted as functions of temperature in Figs. 4.7(b) and (c), respectively. Accurate fits are obtained with decay times for ϕ and $|\psi|^2$ fixed at 1.4 ps and 40 ps, respectively. The physical picture of the coupled order parameter dynamics is as follows: immediately after photoexcitation, $\Delta\phi(t)/\phi_0(T) = -F$, just as in the normal state. However, for times $t \gg \gamma^{-1}$, a quasiequilibrium is reached in which $\phi(t) \approx \phi_1(t)$; that is, the time dependence of $\phi(t)$ tracks $\delta|\psi(t)|^2$. Note that whereas $\phi(t)$ is initially reduced relative to its equilibrium value, it is enhanced for $t \gg \gamma^{-1}$ due to the photoinduced suppression of superconducting order.

4.4 Conclusion

To summarize, we used time- and spatially-resolved optical birefringence to probe C_4 symmetry breaking in the model iron-pnictide system $BaFe_2(As_{1-x}P_x)_2$ as a function of temperature and P concentration, x. Spatially resolved measurements probed symmetry breaking on a 10-100 μm length scale, which lies between the scales probed by STM and bulk probes such as transport and scattering. Sub-picosecond time resolution enabled measurement of the dynamics of competition between C_4-breaking and superconducting order.

In underdoped ($x < 0.28$) samples C_4 breaking is observed well above the structural transition temperature. Its gradual onset follows the Curie-Weiss law and is consistent with a

combination of divergent nematic susceptibility and local uniaxial strain. A more surprising result was found for $x > 0.31$, where we found evidence for a phase transition above the superconducting dome that is not seen by bulk probes. We tentatively attributed this to the effect of linear-quadratic coupling between nematic and magnetic degrees of freedom, which in the presence of local uniaxial strain, can boost the Néel temperature to a finite value [14]. We examine this hypothesis in the following chapter.

The existence of birefringent domains in an optimally-doped sample enabled us to study the dynamic coupling between C_4 breaking and superconductivity at $x = 0.31$. Using time-resolved reflectance, we measured the amplitude of birefringence as a function of time after pulsed optical excitation. Above the transition to superconductivity, photoexcitation reduces birefringence, while below T_c birefringence is enhanced after an initial period of weakening of approximately 1 ps duration. We modeled this reversal of sign quantitatively using a time-dependent Ginzburg-Landau approach based on a repulsive interaction between C_4-breaking and superconducting order. The success of the model suggests that C_4-breaking (and perhaps magnetic order) can coexist and compete with superconductivity near optimal doping.

Chapter 5

Imaging nematicity near the quantum critical point

Iron-based superconductors [4, 5, 6] have been the subject of significant interest largely as a result of evidence for quantum criticality [39, 17, 11, 40, 20, 27, 18, 19, 21] accompanied by divergent nematic susceptibility [41, 42, 13, 43, 26] in the vicinity of optimal doping. These phenomena have been associated with an enhancement of the superconducting critical temperature T_c [44, 45, 46].

Evidence for a quantum critical point (QCP) near optimal doping is particularly strong in $BaFe_2(As_{1-x}P_x)_2$, or P:Ba122, an isoelectronically doped superconductor. At high temperature this material has a tetragonal crystal structure, shown in Fig. 5.1(a), consisting of layers of Fe ions arranged in a square lattice with a pnictogen ion alternating above and below the center of each plaquette, and Ba ions between the layers. The parent compound $BaFe_2As_2$ undergoes simultaneous tetragonal-to-orthorhombic and Néel spin-density-wave (SDW) transitions at $T_N \approx 150$ K [47], breaking four-fold rotational (C_4) symmetry. Substitution of As by P [15] and c-axis compression [48] each suppress T_N by reducing the average height of pnictogen ions and widening the Fe $3d$ bands, which destabilizes the SDW order [9]. Bulk probes, including neutron and x-ray scattering, transport, NMR [8], and specific heat [27], indicate that the SDW phase onsets above T_c for P concentration up to, but not above, $x = 0.29$, just below optimal doping ($x = 0.3$).

Despite the evidence from these bulk probes, persistent hints that C_4 symmetry is broken in samples with $x > 0.3$ suggest that there is more to the story. Angle-resolved photoemission (ARPES) [28, 29] and torque magnetometry [30] studies have found evidence of broken C_4 symmetry above the dome of superconductivity persisting above optimal doping in P:Ba122, and optical data suggest similar behavior in $Ba(Fe,Co)_2As_2$ [31].

The simplest explanation for this apparent discrepancy is that typical samples are under strain. This strain can either be frozen in during crystal growth, which we call intrinsic strain, or caused by the crystal mounting and cooling processes, which we call extrinsic strain. Such strain, when coupled with diverging nematic susceptibility near the QCP, would induce nematic order that would strengthen rapidly but smoothly with decreasing

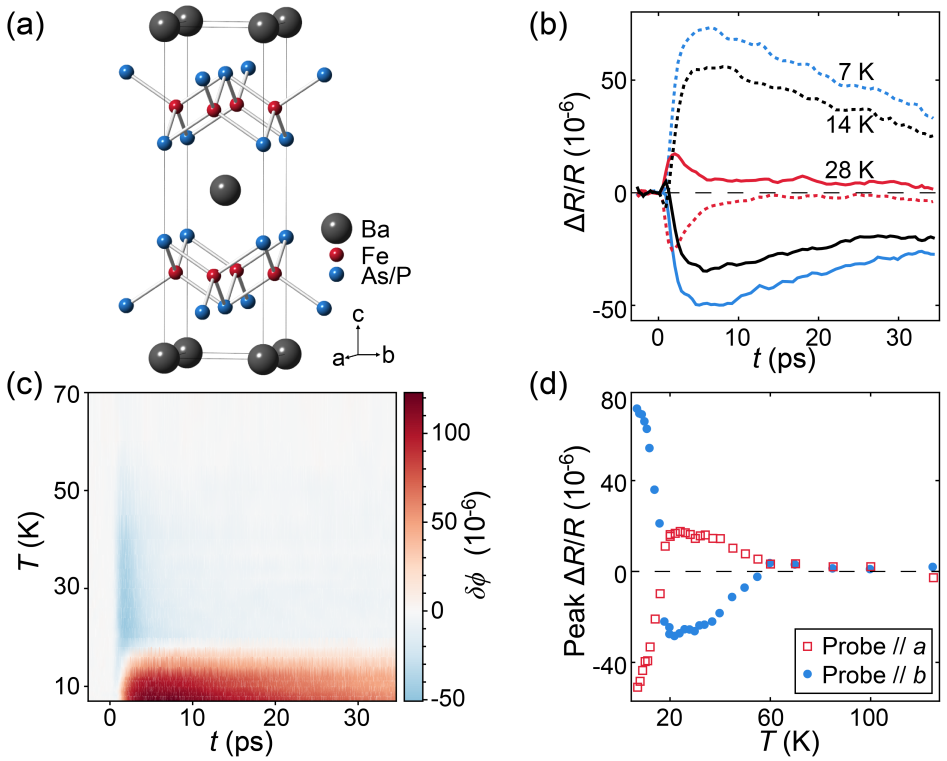

Figure 5.1: Crystal structure of P:Ba122 and photomodulation results at optimal doping. (a) Crystal structure of P:Ba122. (b) pump-probe response $\Delta R/R$ as a function of time at a fixed position, with probe polarization parallel to the Fe−Fe directions a (solid) and b (dotted). Red, black, and blue traces correspond to $T = 28$ K, 14 K, and 7 K, spanning the apparent superconducting transition temperature. (c) Time and temperature dependence of the C_4-odd photomodulation response $\delta\phi \equiv (\Delta R_b - \Delta R_a)/R$. (d) Temperature dependence of the maximum-amplitude value of $\Delta R(t)/R$ for probe polarization along a (red) and b (blue), illustrating near-perfect antisymmetry under a $\pi/2$ rotation of the probe polarization, abrupt onset of broken C_4 symmetry, and competition between superconductivity and nematic order.

temperature. However, the measurements of nematicity at $x > 0.3$ indicate that it tends to have an abrupt onset [28, 29, 31], and our results corroborate this observation.

In this chapter we present a study of nematicity in optimally doped P:Ba122, with the aim of resolving the apparent contradiction between implications from different experiments. We map a single region of a P:Ba122 crystal with two local probes of broken C_4: time-resolved optical pump-probe reflectance, or photomodulation, which enhances weak structure in the reflectance R [49]; and scanning Laue microdiffraction [33], which allows us to explore the link between local strain and the onset and strength of nematicity. Our photomodulation measurements reveal nematic order above T_c, with magnitude, sign, and onset temperature varying on a length scale of 50−100 μm.

Contrary to expectation, we find that the nematic order observed via photomodulation is strongest in regions where uniaxial strain and transverse dilation are weakest. However, the boundaries of domains of nematic order coincide with sharp features in local strain. This suggests that the nematic order develops in a genuine phase transition rather than as a result of local anisotropy amplified by strong nematic susceptibility. Our results are consistent with a surface nematic phase, as has been suggested by calculations incorporating interlayer hopping [50]. The existence of such a phase would relieve the tension between results from bulk and surface probes.

5.1 Methods

Measurements of photomodulated reflectance, ΔR, were performed using linearly polarized, 100 fs-duration pulses from a mode-locked Ti:Sapphire laser at 80 MHz repetition rate, 800 nm center wavelength, and $\sim$5 μJ/cm^2 fluence. Our initial measurements showed strong dependence of the amplitude and sign of ΔR on the position of the pump-probe focus on the sample surface. As a result, local characterization of the time and temperature dependence of ΔR required accurate stabilization of the position of the laser focus relative to the sample during cooling. This was achieved by registering the sample to an optical landmark on its mount using a high-resolution video feed, enabling us to fix the focal position with a precision of 5 μm.

In order to explore the link between local strain and the onset of nematic order, we used scanning Laue (i.e., polychromatic, with energy range 5$-$20 keV) x-ray microdiffraction to map the local strain at room temperature in the same region of the sample that was imaged using photomodulation (see Sec. 3.3.2 for details on the region-alignment procedure). A full diffraction pattern was collected at each position and used, along with the known lattice parameters, to extract the deviatoric (i.e., traceless) strain tensor $\boldsymbol{\varepsilon}$, which describes the local deformation of the unit cell. In a given basis, the diagonal components ε_{aa}, ε_{bb}, and ε_{cc} of the strain tensor correspond to expansion (or compression, for negative values) along the corresponding direction, while the off-diagonal components ε_{ab}, ε_{bc}, and ε_{ca} correspond to pure shear. Since we are primarily concerned with strain in the Fe$-$As layers, we focus on the ab subsector of $\boldsymbol{\varepsilon}$, which we denote by $\boldsymbol{\varepsilon}^{(t)}$. The dilation of the ab-plane unit cell is given by $\mathrm{Tr}\,\boldsymbol{\varepsilon}^{(t)} = \varepsilon_{aa} + \varepsilon_{bb}$; compression corresponds to negative values.

5.2 Results and discussion

Figure 5.1(b) shows examples of pump-probe traces measured at a fixed position on a sample with $x = 0.31$ at three temperatures spanning the apparent superconducting transition, with the probe polarized along the orthogonal Fe$-$Fe directions, which we (arbitrarily) label a and b (solid and dotted, respectively). (The stated temperatures are nominal; the actual crystal temperature at the laser focus is higher as a result of laser heating. We studied the

apparent superconducting transition temperature as a function of laser fluence and confirmed that T_c approaches 31 K at low fluence; the results are shown in Sec. 5.4.1.)

The photomodulation data show striking evidence of broken C_4 symmetry. In the presence of C_4 symmetry ΔR would be independent of the polarization of the probe electric field; that is, $\Delta R_a = \Delta R_b$. Instead, the pump-probe response is approximately equal and opposite along orthogonal Fe−Fe directions, i.e., $\Delta R_a \approx -\Delta R_b$. In subsequent discussion we consider the strength of the C_4-odd component of the photomodulation response, $(\Delta R_b - \Delta R_a)/R \equiv \delta\phi$, to be a proxy for nematic order (see Sec. 5.4.2 for details).

The full time and temperature dependence of $\delta\phi$ is shown in Fig. 5.1(c). There are two distinct forms of pump-probe response: above the superconducting transition, the response is short-lived and $\delta\phi$ is negative; well below T_c, the response is long-lived and $\delta\phi$ is positive. Near the transition, both forms are apparent. To better illustrate the singular features of the temperature dependence, we plot in Fig. 5.1(d) the maximum-amplitude value of $\Delta R(t)/R$ as a function of temperature for a and b probe polarizations. With decreasing temperature, ΔR first appears abruptly above the noise at ∼60 K. Upon further cooling, the sign of ΔR changes abruptly near T_c, and at low temperature the sign is reversed relative to the normal state.

The change in sign and relaxation rate at T_c can be understood on the basis of competition between the nematic order parameter, ϕ, and the superconducting order parameter, ψ. For $T > T_c$, the pump pulse weakens the nematic order, which then returns rapidly to its equilibrium value. However, for $T < T_c$ the pump also suppresses ψ, and since the timescale of this suppression is longer than that of the nematic order a quasiequilibrium results in which ϕ is enhanced due to the mutual repulsion of ϕ and ψ. The enhancement of ϕ persists until ψ returns to its equilibrium amplitude. For a detailed discussion of this model, refer to Sec. 4.3.3.

The observation of broken C_4 at a fixed location on the sample surface strongly suggests domain formation as the origin of the position dependence described above. To test this hypothesis, we mapped the variation of $\delta\phi$ on the sample surface. These maps were obtained by mounting samples onto an xyz piezo-stage, and scanning the sample with respect to an 8 μm diameter focus of overlapping pump and probe beams. The P:Ba122 crystal was mounted on a Cu plate, providing a net 0.2% compressive strain on the base of the sample via thermal contraction.

A map of local nematicity obtained by spatially resolved photomodulation is shown in Fig. 5.2(a). The color of each square encodes the maximum-amplitude value, $\delta\phi_M$, of $(\Delta R_b(t) - \Delta R_a(t))/R$, that is, of the difference between ΔR measured along the two principal axes. Domain boundaries separating regions of broken C_4 symmetry with orthogonal nematic order are readily apparent. We note that the typical domain size of ∼100 μm is large compared to the ∼10 μm structural domains that have been imaged using polarized light below the structural transition in underdoped P:Ba122 [37, 51, 12], and that 100 μm is the approximate size of crystals used in the previously cited torque magnetometry experiments that suggested a broad nematic phase above the superconducting dome [30].

The spatial patterns of positive and negative $\delta\phi_M$ do not change with repeated heating and cooling of the sample, suggesting that the magnitude and sign of the nematic order are

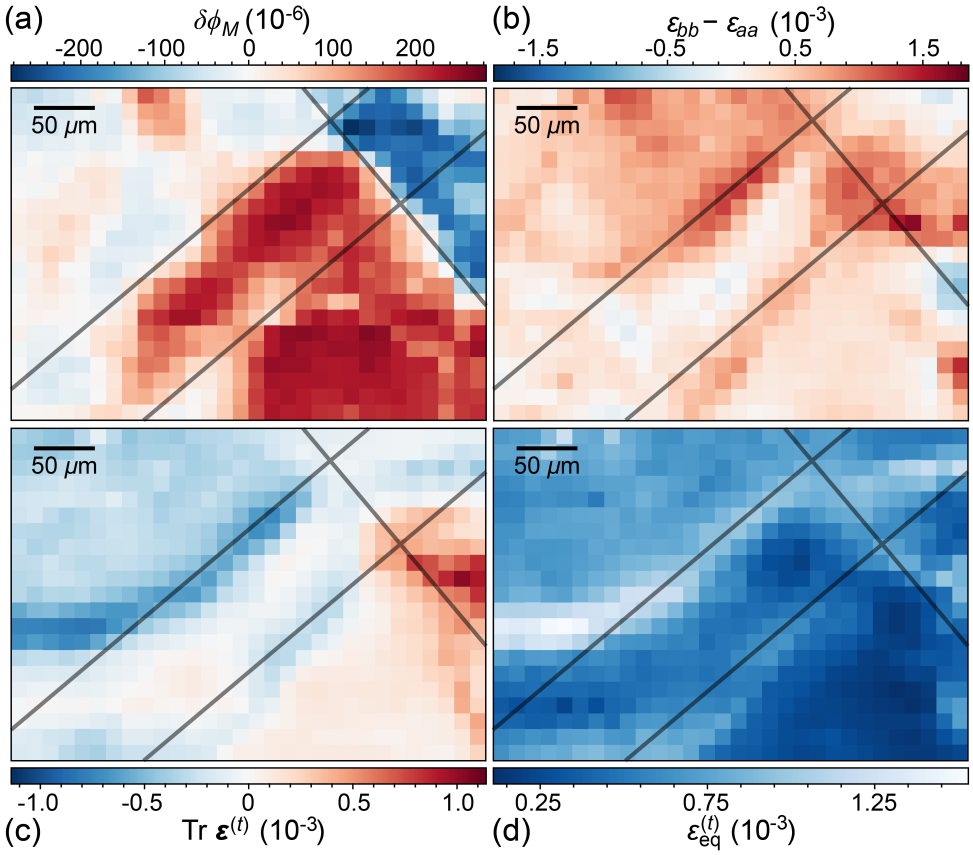

Figure 5.2: Spatial variation (13 μm resolution) of optical anisotropy (a) and ab-plane strain (b-d) on a 390×260 μm region of an optimally doped P:Ba122 crystal mounted on Cu. (a) Photomodulation proxy for nematic order, $\delta\phi_M$. (b) Transverse strain anisotropy $\varepsilon_{bb} - \varepsilon_{aa}$ in the Fe−Fe basis. (c) Transverse unit cell dilation $\mathrm{Tr}\,\boldsymbol{\varepsilon}^{(t)}$. (d) Transverse equivalent strain $\varepsilon_{\mathrm{eq}}^{(t)} = (2\varepsilon_{ij}^{(t)}\varepsilon_{ij}^{(t)}/3)^{1/2}$. Superimposed lines are parallel to the Fe−Fe directions and are located at the same positions in each image to facilitate visual comparison of features. Optical data were collected at $T = 5$ K; strain data at room temperature.

determined by some local quantity. A local strain field, perhaps frozen into the crystal during growth, is a natural candidate; a difference between the strains along orthogonal Fe−Fe directions would couple directly to C_4-breaking order [14]. Another potential contributing factor is local in-plane compression of the unit cell [52], which would increase the pnictogen height and the Fe−As−Fe bond angle, counteracting the effect of P doping [9] and driving the crystal back toward the underdoped SDW phase.

We used scanning Laue microdiffraction to investigate the relationship between local strain and the onset of the optically observed nematic order. Figure 5.2 illustrates the relationship between the previously discussed map of low-temperature optical anisotropy in Fig. 5.2(a) and the spatial variation of the strain tensor in Figs. 5.2(b-d). The superimposed

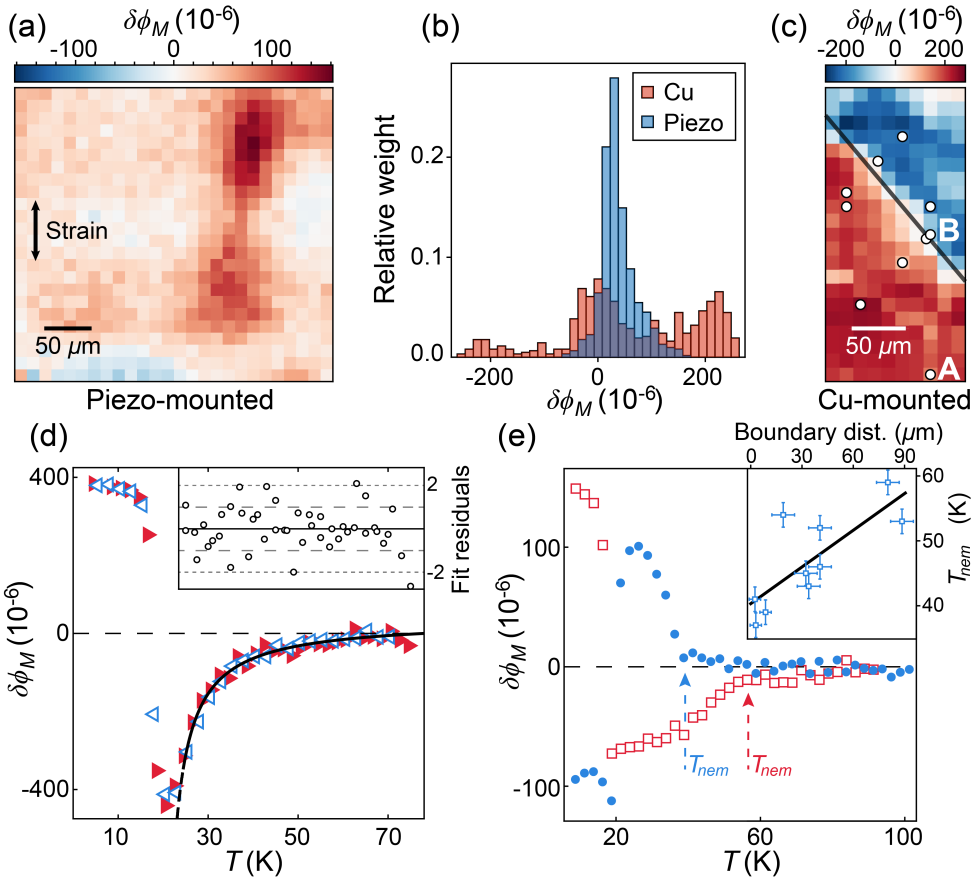

Figure 5.3: Comparison of spatial variation (13 μm resolution) and temperature dependence of nematic order for piezo-mounted (uniaxially strained) and Cu-mounted (biaxially strained) crystals. (a) Spatial variation of photomodulation proxy for nematic order, $\delta\phi_M$, on the piezo-mounted crystal, which is uniaxially strained as indicated. (b) Histograms showing distribution of $\delta\phi_M$ for both crystals. (c) Spatial variation of $\delta\phi_M$ on the Cu-mounted crystal, with open circles indicating positions at which temperature dependence data was collected and black line marking a region of null $\Delta R/R$ response separating regions of opposite nematic sign. (d) Temperature dependence of $\delta\phi_M$ for the piezo-mounted crystal while warming (right-pointed triangles) and cooling (left-pointed triangles). The black line is a Curie-Weiss fit with $T_{CW} = 19$ K (solid on fitted domain; dashed at lower temperatures). Inset: standardized fit residuals. (e) Temperature dependence of $\delta\phi_M$ for the Cu-mounted crystal far from the boundary at the point marked A (open squares) and near the boundary at the point marked B (circles). Apparent nematic transition temperatures are indicated. Inset: scatter plot of nematic transition temperature and distance from the domain boundary indicated by the black line in (c); correlation is positive with p-value $< 10^{-2}$.

lines, oriented with the Fe−Fe directions a and b, are positioned identically on each image. Figure 5.2(b) shows the strain anisotropy in the Fe−Fe basis, $\varepsilon_{bb} - \varepsilon_{aa}$, in the same region

of the crystal. Contrary to what would be expected if the nematic order were the result of a local strain bias, the changes in sign of $\delta\phi_M$ and the Fe−Fe strain anisotropy do not coincide. Furthermore, the Fe−Fe strain anisotropy is small in magnitude in most of the region where the nematic photomodulation response is strongest. Figure 5.2(c) shows the transverse unit-cell dilation $\mathrm{Tr}\,\boldsymbol{\varepsilon}^{(t)}$, which is small and mostly positive in the large region corresponding to large positive $\delta\phi_M$, contradicting the prediction that negative $\mathrm{Tr}\,\boldsymbol{\varepsilon}^{(t)}$ would drive the system toward the C_4-breaking SDW phase. Finally, Fig. 5.2(d) shows the equivalent strain $\varepsilon_{\mathrm{eq}}^{(t)} = (2\varepsilon_{ij}^{(t)}\varepsilon_{ij}^{(t)}/3)^{1/2}$, a measure of total strain. Although the nematic order and the strain anisotropy are not strongly correlated, the edges of the nematic domains are coincident with strain features; in particular, with local maxima in the equivalent strain and with extrema in $\mathrm{Tr}\,\boldsymbol{\varepsilon}^{(t)}$. (We note that the observed strain variations are likely intrinsic rather than extrinsic, as we observed similar variations in an optimally doped crystal mounted strain-free; see Sec. 5.4.3 for details.

Taken together these results strongly suggest that local strain is not the driver, via divergent susceptibility, of the nematicity we observe – in fact, strong strain anisotropy (and strong strain in general) appears to suppress the electronic nematicity.

In order to further study the effect of extrinsic uniaxial strain, we also performed ultrafast microscopy on an optimally doped sample mounted on a piezoelectric stack. On cooling, the piezo provides a tensile uniaxial strain by thermally contracting by 0.1% (similar to optimally doped P:Ba122) along one lateral dimension while expanding by 0.1% along the other. The crystal's Fe−Fe directions were aligned with these principal piezo axes. The resulting image of $\delta\phi_M$ is shown in Fig. 5.3(a). The domain population of the uniaxially strained crystal differs significantly from that of the Cu-mounted sample, as is evident in Fig. 5.3(b), which compares histograms of $\delta\phi_M$ in both samples. The uniaxial strain appears to bias the domain population, shifting the central Cu peak while suppressing the large-amplitude nematic response. Thus, while intrinsic strain defies expectation, extrinsic strain biases the electronic nematicity in the expected manner.

In addition to pump-probe microscopy, we measured the temperature dependence of $\delta\phi_M$ on both crystals, including at multiple points on the Cu-mounted sample. These points are indicated by white circles in Fig. 5.3(c), and the points marked A and B correspond respectively to the red and blue $\delta\phi_M(T)$ markers in Fig. 5.3(e), where $\delta\phi_M$ is plotted as a function of temperature.

The onset of the nematic optical response in the Cu-mounted crystal is abrupt at each position, and is manifestly distinct from a smooth Curie-Weiss behavior. The onset temperature varies between approximately 40 K and 60 K and is positively correlated (p-value $< 10^{-2}$) with distance from the line of null nematic response, as illustrated in Fig. 5.3(e). This range of onset temperatures is consistent with ARPES measurements [29] but is lower than the 100 K onset observed via torque magnetometry [30].

In contrast to the Cu-mounted sample, the temperature dependence of $\delta\phi_M$ on the piezo-mounted crystal is well-described by a Curie-Weiss form with transition temperature $T_{CW} = 19$ K. The fit (black line; solid on fitted region) and data are shown in Fig. 5.3(d),

with the standardized fit residuals in the inset. In the presence of strong, uniform uniaxial strain, therefore, we observe a nematic onset that is consistent with the picture of divergent nematic susceptibility, which makes the sharpness of the nematic onset in the Cu-mounted sample all the more notable. We do not observe any hysteretic difference between the data collected with increasing temperature (right-pointed markers) and with decreasing temperature (left-pointed markers).

The strong correlation between the nematic onset temperature and distance from the boundary between the positive and negative domains suggests that we may be observing a nucleation phenomenon, where the nematic domains arise deterministically at some distant crystalline features and then spread as the temperature decreases until they reach the high-equivalent-strain boundaries indicated in Fig. 5.2(d). This picture is particularly compelling in light of recent work incorporating hopping between Fe−As layers, which has shown that interlayer hopping can produce a surface nematic phase that onsets at significantly higher temperatures than in the bulk [50]. A surface phase, which could also arise due to stabilization of fluctuating order by soft surface phonons [53], would be more susceptible to confinement by boundaries of strain due to the reduced dimensionality and volume of the required region of contiguous deformation, and could be disfavored under transverse compression due to buckling-induced disorder. In addition, this model is consistent both with surface measurements that indicate a genuine nematic phase ([28, 29, 31], this work) and with bulk measurements that show no evidence of a phase transition [8, 27, 15]. An important open question that remains is what mechanism deterministically selects the sign of the nematic order at a given point on the crystal surface.

5.3 Summary

In conclusion, photomodulation measurements reveal that optimally doped $BaFe_2(As,P)_2$ has a C_4-breaking phase well above T_c that varies strongly in magnitude, sign, and onset temperature at length scales of 50−100 μm. Scanning Laue microdiffraction measurements show that the local strain anisotropy and local transverse compression of the unit cell, which are both expected to favor nematic order, are anticorrelated with the observed optical nematicity. These results imply that the optical nematicity in the biaxially strained crystal corresponds to a genuine nematic phase transition rather than amplification of local anisotropy by enhanced nematic susceptibilty. We interpret this phase as a surface phenomenon [50] that nucleates well above T_c and spreads until it reaches boundaries where the crystal is highly strained. A surface nematic phase with large domains reconciles ARPES [28, 29], optical [31], and torque magnetometry [30] measurements showing nematic order at optimal doping with bulk measurements [8, 27, 15] that do not show a phase transition. In general, phase diagrams of two-dimensional materials may differ significantly from those based on bulk measurements of the same compound.

5.4 Additional notes and data

5.4.1 Fluence dependence of T_c

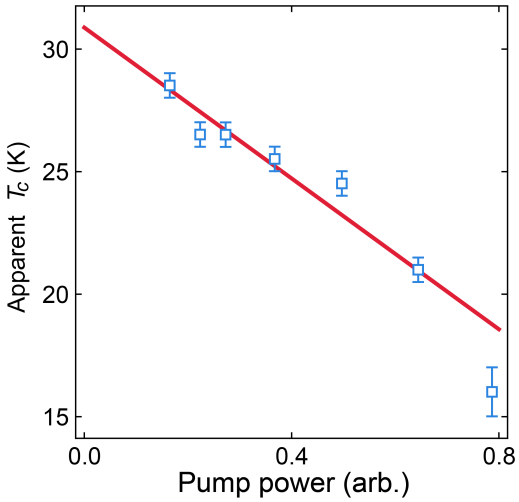

Figure 5.4: Apparent superconducting transition temperature T_c as a function of pump power in an optimally doped P:Ba122 sample. At zero power, the extrapolated T_c is 30.9 ± 0.9 K.

We collected photomodulation data as a function of temperature for a range of pump fluences. Figure 5.4 shows the apparent superconducting transition temperature T_c as a function of pump power. While pump-induced heating has a significant effect on nominal T_c at high fluence, a linear regression yields a low-power limit of $T_c = 30.9 \pm 0.9$ K, consistent with expectations.

5.4.2 Photomodulation anisotropy as a proxy for C_4-breaking order

In the pump-probe reflectivity experiment, the pump pulse, which generically causes an incoherent excitation of electrons, can couple to an order parameter Φ in two characteristic ways: 1) by raising the electron temperature T_e, in which case $\Delta R \propto \delta\Phi/\delta T_e$ and ΔR will be peaked near its transition temperature; or 2) by directly suppressing the order by depopulating relevant electronic states, in which case $\Delta R \propto \Phi$.

We performed a detailed study of the temperature dependence of the nematic pump-probe response in underdoped P:Ba122. In Fig. 5.5 we plot the peak (maximum amplitude) value of $(\Delta R_b - \Delta R_a)/R$ as a function of temperature for four underdoped P:Ba122 samples, along with fits to a Curie-Weiss temperature dependence. This quantity, which is odd under a $\pi/2$ rotation, has the symmetry of a nematic order parameter, and is approximately proportional

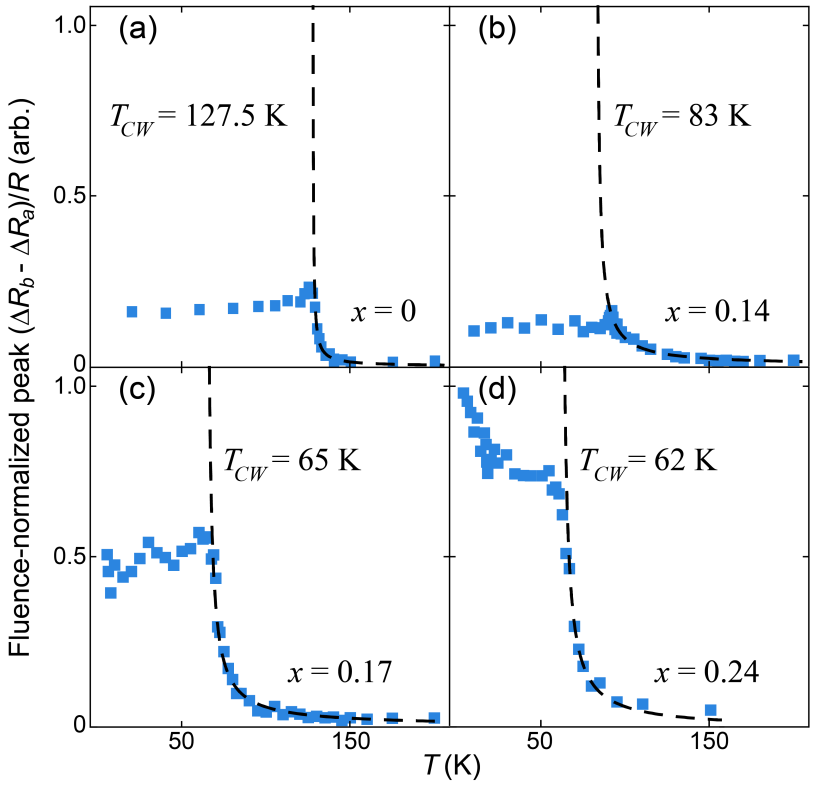

Figure 5.5: Normalized peak antisymmetrized pump-probe response, $(\Delta R_b - \Delta R_a)/R$, as a function of temperature for underdoped P:Ba122 samples with P concentration (a) $x = 0$, (b) 0.14, (c) 0.17, and (d) 0.24. Fits to a Curie-Weiss form proportional to $1/(T - T_{CW})$ are indicated by dashed lines.

to the C_4-breaking order parameter rather than its temperature derivative. This indicates that $(\Delta R_b - \Delta R_a)/R$ can be used as a proxy for nematic order in the P:Ba122 system.

5.4.3 Strain is not caused by mounting or cooling

In order to determine whether the strain variations we observed were intrisic or extrinsic, we performed micro-Laue measurements on a separate optimally doped P:Ba122 crystal mounted using grease and never cooled below room temperature. Figure 5.6 shows histograms of the Fe−Fe basis strain anisotropy drawn from the original sample, mounted with epoxy, and the grease-mounted sample. The strain anisotropy distributions are qualitatively very similar, indicating that the strain inhomogeneity we observe arises during sample growth.

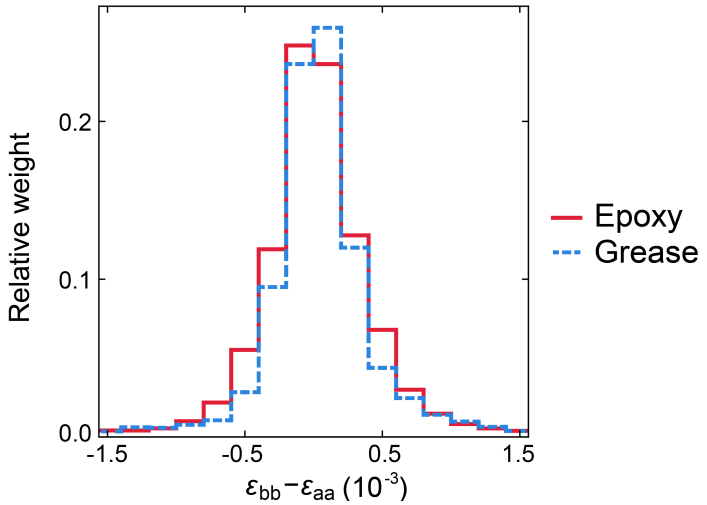

Figure 5.6: Distributions of Fe−Fe basis strain anisotropy in optimally doped P:Ba122 mounted with epoxy (solid red) and grease (dashed blue).

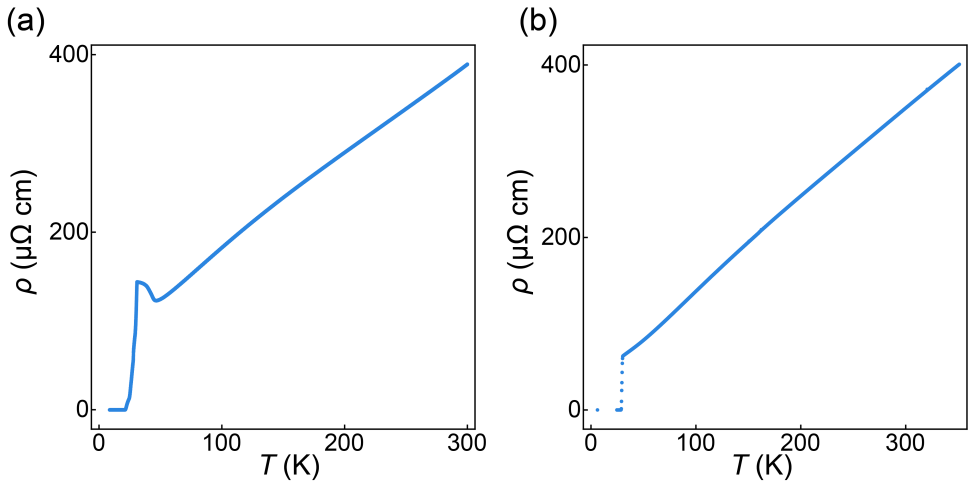

Figure 5.7: Resistivity as a function of temperature, measured on typical P:Ba122 samples with (a) $x = 0.26$ and (b) $x = 0.31$.

5.4.4 Resistivity

We performed resistivity measurements to confirm sample quality. Figures 5.7(a-b) show typical temperature dependence curves for an underdoped and optimally doped sample, respectively. In contrast to the significant resistivity increase as the sample cools through the Néel transition in the underdoped sample, the optimally doped sample has a monotonic temperature dependence and a sharp superconducting transition at 30 K.

5.4.5 Reproducibility across samples

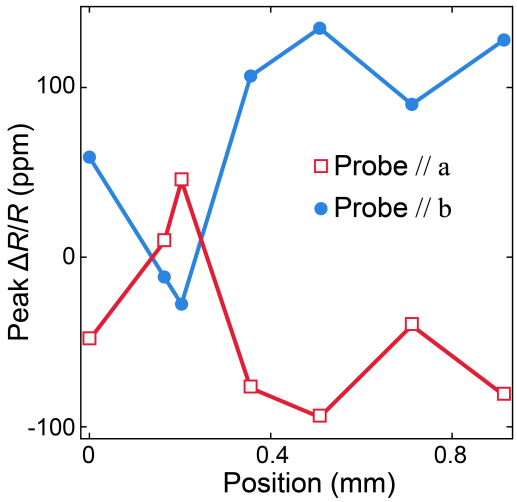

Figure 5.8: Position dependence of the peak pump-probe response $\Delta R/R$ as a function of position on a different sample to that discussed in the main text, with probe polarization parallel to the Fe−Fe directions a (red squares) and b (blue circles).

In order to confirm that the behavior we report is not an anomaly, we studied multiple optimally doped $BaFe_2(As,P)_2$ samples. The data in Fig. 5.1 were obtained using a different sample from the one we studied via optical and Laue mapping. In addition, before we developed our optical microscopy capabilities, we had strong evidence of the existence of nematic domains based on a coarse position dependence of the pump-probe response, shown in Fig. 5.8. Using a larger (100 μm) focal spot on a sample from a different growth, we found that the peak $\Delta R/R$ response retained near-perfect antisymmetry while varying strongly in magnitude, including changes in sign.

Chapter 6

Nematicity beyond optimal doping

6.1 Introduction

In light of the observation of nematicity in optimally doped P:Ba122 described in Chs. 4 and 5, we extended our investigation into the overdoped regime. In this chapter we report the results of exploratory photomodulation and micro-Laue measurements on $BaFe_2(As_{1-x}P_x)_2$ with $x = 0.39$, 0.44, and 0.50, corresponding to $T_c = 27$ K, 23 K, and 18 K respectively.

Our optical measurements show that the fraction of the crystal surface that is strongly nematic decreases with increasing doping, but that all three samples nonetheless contain regions of strong nematicity, which are concentrated near crystal edges. By aligning micro-Laue and optical maps and studying the correlation between nematicity and the strain features discussed in Ch. 5 (namely, equivalent strain $\varepsilon_{\text{eq}}^{(t)} = (2\varepsilon_{ij}\varepsilon_{ij}/3)^{1/2}$, transverse dilation $\text{Tr}\,\boldsymbol{\varepsilon}^{(t)}$, and ab-plane strain anisotropy $\varepsilon_{bb} - \varepsilon_{aa}$, where the a and b axes are taken to correspond to the Fe−Fe directions), we find that the nematicity cannot be explained as an effect of any of these strain quantities, in agreement with the results of the previous chapter. Rather, sample topography appears to play an important role. The samples all exhibit inhomogeneity at the 10−100 μm length scale, implying that an experimental picture of the full breadth of phenomena in these materials requires a multiple-scale analysis. We also find that the measured superconducting critical temperature in apparently non-nematic regions of the $x = 0.50$ sample depends on the pump/probe polarization, with a difference of 0.5−2 K. This effect is not observed at any lower dopings.

6.2 Results

6.2.1 $T_c = 27$ K, $x = 0.39$

Figure 6.1 illustrates the spatial variation of strain and nematicity in the $T_c = 27$ K, $x = 0.39$ sample. The optical and Laue images were aligned according to the landmarking procedure described in Sec. 3.3.2. The topography of the sample surface is shown via the average Laue

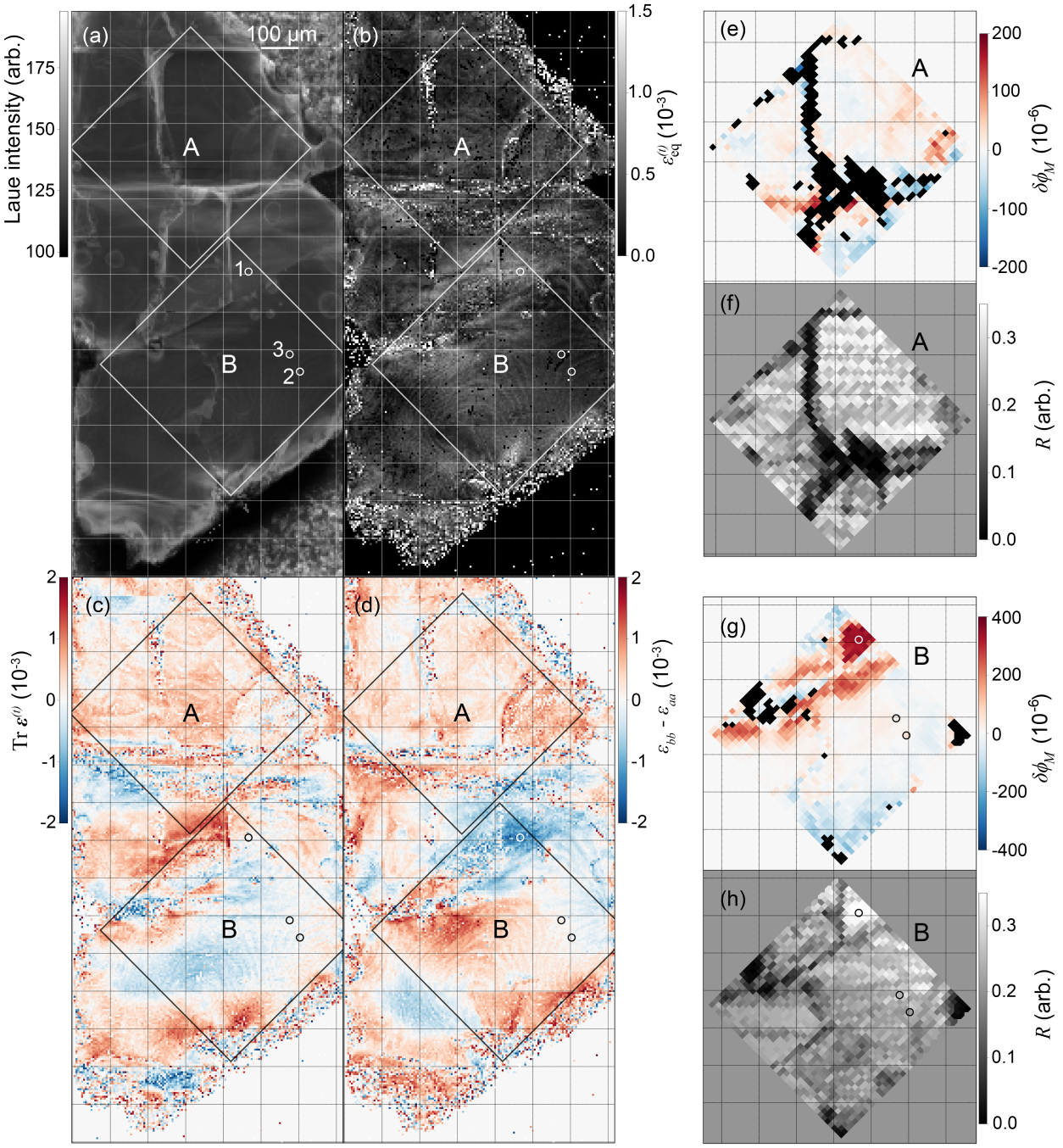

Figure 6.1: Spatial variation of *ab*-plane strain (a-d) and optical anisotropy at 5 K (e-h) in slightly overdoped P:Ba122 ($x = 0.39$, $T_c = 27$ K). (a) Average x-ray intensity, showing the structure of the sample surface. (b) Transverse equivalent strain $\varepsilon_{\rm eq}^{(t)} = (2\varepsilon_{ij}^{(t)}\varepsilon_{ij}^{(t)}/3)^{1/2}$. (c) Transverse dilation, $\mathrm{Tr}\,\boldsymbol{\varepsilon}^{(t)}$. (d) Strain anisotropy $\varepsilon_{bb} - \varepsilon_{aa}$ in the Fe−Fe basis. (e, g) Photomodulation proxy for nematic order, $\delta\phi_M$, in Regions A, B respectively. Black: low-reflectivity regions. (f, h) Optical reflectivity in Regions A, B respectively. For a full description of other annotations see Sec. 6.2.1.

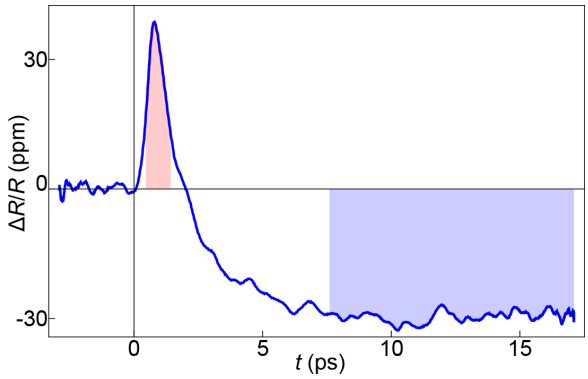

Figure 6.2: Example $\Delta R(t)/R$ trace from the $x = 0.50$ sample, collected at 11 K. The normal-state and superconducting integration regions are denoted by red and blue shading, respectively. The mean $\Delta R/R$ in these regions is interpreted as a measure of the strength of the corresponding order parameter.

intensity in panel (a), and panels (b-d) show the transverse equivalent strain, transverse dilation, and *ab*-plane strain anisotropy in the Fe−Fe basis, respectively. Panels (e-h) show the optical nematicity (e, g) and reflectivity (f, h) in the regions marked A (e, f) and B (g, h) in panels (a-d). The points marked with circles and numbered in panel (a) correspond to the locations of the temperature scans shown in Fig. 6.3. The boundaries of the Regions A and B that were studied via photomodulation are marked on the Laue images. The square grid is aligned on each image and has a spacing of 100 μm.

As was the case at optimal doping, none of the most natural strain quantities appears to be the cause of the nematicity. The transverse dilation (Fig. 6.1(c)) is uncorrelated with nematicity, and while the *ab*-plane strain anisotropy (panel (d)) is strong near the top of Region B, where the nematicity is strongest, there is no opposite-sign nematicity in regions where the *ab*-plane strain anisotropy is strong with the opposite sign, such as the left of Region B. While there is an apparent positive correlation between nematicity and transverse equivalent strain (panel (b)), this relationship does not appear to be causal, as illustrated by the fact that the strong nematicity near the top of Region B is confined to the right of the central line, while the equivalent strain is approximately constant across that line.

Rather than strain, the data suggest that macroscopic properties of the sample topography, which can be seen in Fig. 6.1(a), play an important role. The nematicity is concentrated near the boundaries of flat regions where one cleaving plane meets another, and in particular the region of strongest nematicity near the top of Region B corresponds to the corner of a cleaved region.

Figure 6.2 shows an example $\Delta R/R$ time trace from the $x = 0.50$ sample, collected at 11 K. The time dependence of $\Delta R/R$ in the overdoped regime has the same qualitative character as at lower dopings (see Sec. 4.3.3): above T_c, $\Delta R/R$ peaks and decays quickly, with a decay time comparable to 1 ps; just below T_c the response of the superconducting order parameter is apparent along with the aforementioned fast-decaying normal-state response; as

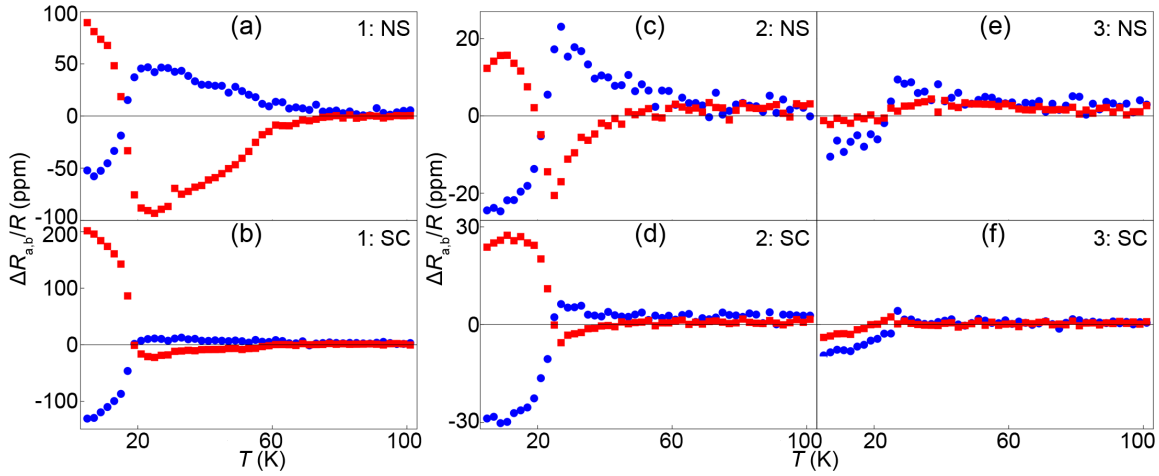

Figure 6.3: Temperature dependence of photomodulation response in slightly overdoped P:Ba122 ($x = 0.39$, $T_c = 27$ K). (a-b), (c-d), (e-f) Normal-state (NS) (a, c, e) and superconducting (SC) (b, d, f) components of $\Delta R_{a,b}(t)/R$ at points 1, 2, and 3 in Fig. 6.1(a), respectively. Blue circles and red squares correspond to data collected with probe polarizations parallel to orthogonal Fe−Fe directions.

$T \to 0$ the superconducting response becomes dominant. This general tendency holds both in strongly nematic regions, where the sign of $\Delta R/R$ changes with polarization rotation, and in regions that are much more isotropic, like near point 3 in Fig. 6.1 (marked in panel (a)). In order to study the independent evolution of both photomodulation components with changing temperature, we compute the mean $\Delta R/R$ in the time regions where the different signals dominate. The shaded regions in Fig. 6.2 denote the superconducting (blue; 9.5 ps duration) and normal-state (red; 1 ps duration) integration regions.

Figure 6.3 shows the temperature dependence of the normal-state (a, c, e) and superconducting (b, d, f) responses at the points numbered 1, 2, and 3 in Fig. 6.1(a) (panels (a-b), (c-d), and (e-f) respectively).

At point 1, shown in Fig. 6.3(a-b), which is in the center of the region of strongest nematicity, the normal-state response is nematic up to approximately 80 K, where the nematicity goes linearly to zero. The temperature derivative of the nematicity changes sharply at 60 K, and the response deep in the superconducting phase is strongly nematic with opposite sign relative to the normal state. The temperature dependence at point 2 (panels (c-d)) was of interest because the photomodulation response there was moderately strong and nematic, despite the fact that point 2 is surrounded by a large region exhibiting weak, isotropic response. The response at point 2 shares the low-temperature nematicity and sign change across the superconducting transition observed at point 1, but the onset of the nematicity is much more Curie-Weiss-like. Point 3 (panels (e-f)) is separated from point 2 by approximately 50 μm, and shows the character of the response in the non-nematic region surrounding point 2. The photomodulation response is quite weak, and while there is an

obvious difference between the a- and b-polarized responses, there is notably no change in sign under polarization rotation, except for at 25 K, just below T_c, and then only in the superconducting component.

6.2.2 $T_c = 18$ K, $x = 0.50$

Figure 6.4 illustrates the spatial variation of strain and nematicity in the $T_c = 18$ K, $x = 0.50$ sample. As in Fig. 6.1, the sample surface topography is shown in panel (a), and panels (b-d) show various strain quantities of interest. Panels (e) and (f) show the optical nematicity and reflectivity, respectively, in the boxed region marked in panels (a-d).

The $T_c = 18$ K sample has a much higher fraction of isotropic photomodulation response than at $x = 0.39$. Only small patches of nematicity are apparent in Fig. 6.4(e), most notably in the left corner of the optical region. The transverse dilation and ab-plane strain anisotropy both vary significantly throughout the optical region, where the response is essentially non-nematic, so these quantities appear to be unrelated, as suggested by our study of the $T_c = 27$ K sample in Sec. 6.2.1. While the transverse equivalent strain is elevated in the vicinity of the nematic patch, it is comparably strong in various other regions where the optical response is isotropic. Again, it appears that nematicity is associated with proximity to sample edges, although it is notable that the majority of the sample edge regions are non-nematic.

Figure 6.5 shows the temperature dependence of the normal-state (panels (a, c, e, g, i)) and superconducting (panels (b, d, f, h, j)) responses at the points numbered 1, 2, and 3 in Fig. 6.4(a) (panels (a-b), (c-d), (e-f), respectively), along with results from a separate study of a fourth point (point 4) near point 3 wherein we took particular care to eliminate any dependence of the pump power on polarization (g-j).

At point 1, where the photomodulation response (panels (a-b)) is strongly nematic, the temperature dependence is reminiscent of the nematic region of the $x = 0.39$ sample. The normal-state component becomes nematic at approximately 140 K, and the nematicity begins to increase more sharply as the sample is cooled below 95 K (a-b)c.f. 100 K and 60 K respectively for the corresponding phenomena at $x = 0.39$; see Fig. 6.3(a-b)). Unlike in the previous sample, the long-time superconducting component strengthens significantly, well above the nominal T_c, starting at approximately 30 K, before changing sign sharply below T_c, as at $x = 0.39$. The superconducting transition at point 1 begins at (nominal) temperature between 13 K and 15 K.

At point 2, 20 μm away, the response (panels (c-d)) is almost totally isotropic within the resolution of the measurement, except for the fact that the temperature dependence exhibits an apparent 2 K shift under rotation of the probe polarization. This shift is illustrated in Fig. 6.6(a-j), which contain selected $\Delta R/R$ time traces from the dataset corresponding to Fig. 6.5(c-d). The (weak) pump/probe response is isotropic at 25 K and becomes sharply stronger at 24 K. The superconducting transition at point 2 begins between 18 K and 17 K for the blue traces, and between 16 K and 15 K for the red traces. Well below T_c, the response is isotropic within the measurement resolution.

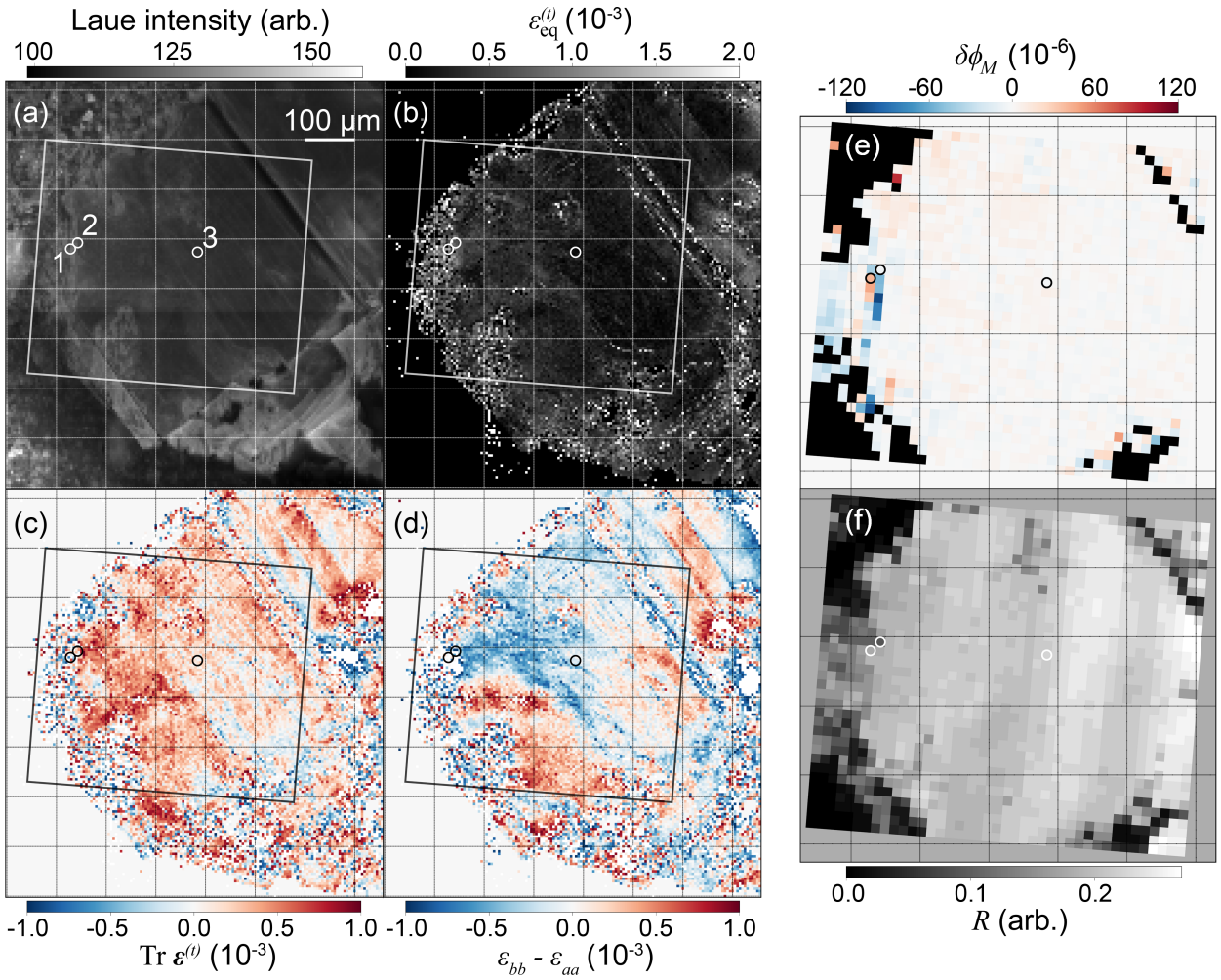

Figure 6.4: Spatial variation of *ab*-plane strain (a-d) and optical anisotropy at 5 K (e-f) in strongly overdoped P:Ba122 ($x = 0.50$, $T_c = 18$ K). (a) Average x-ray intensity, showing the structure of the sample surface. (b) Transverse equivalent strain $\varepsilon_{\rm eq}^{(t)} = (2\varepsilon_{ij}^{(t)}\varepsilon_{ij}^{(t)}/3)^{1/2}$. (c) Transverse dilation, $\mathrm{Tr}\,\boldsymbol{\varepsilon}^{(t)}$. (d) Strain anisotropy $\varepsilon_{bb} - \varepsilon_{aa}$ in the Fe−Fe basis. (e) Photomodulation proxy for nematic order, $\delta\phi_M$. Black: low-reflectivity regions. (f) Optical reflectivity. The points marked with circles and numbered in (a) correspond to temperature scan locations. The boundary of the region studied via photomodulation is marked on the Laue images. The square grid is aligned on each image and has a spacing of 100 μm.

At point 3, in the center of the sample (Fig. 6.5(e-f)), the photomodulation response is both weaker and much more isotropic than at $x = 0.39$ (c.f. Fig. 6.3(e-f)), and the superconducting transition begins between 18 K and 17 K. However, by increasing the pump intensity by a factor of 13.1 (panels (g-j)), we were able to resolve a slight anisotropy in this region. The normal-state component becomes anisotropic abruptly between 35 K and 40 K,

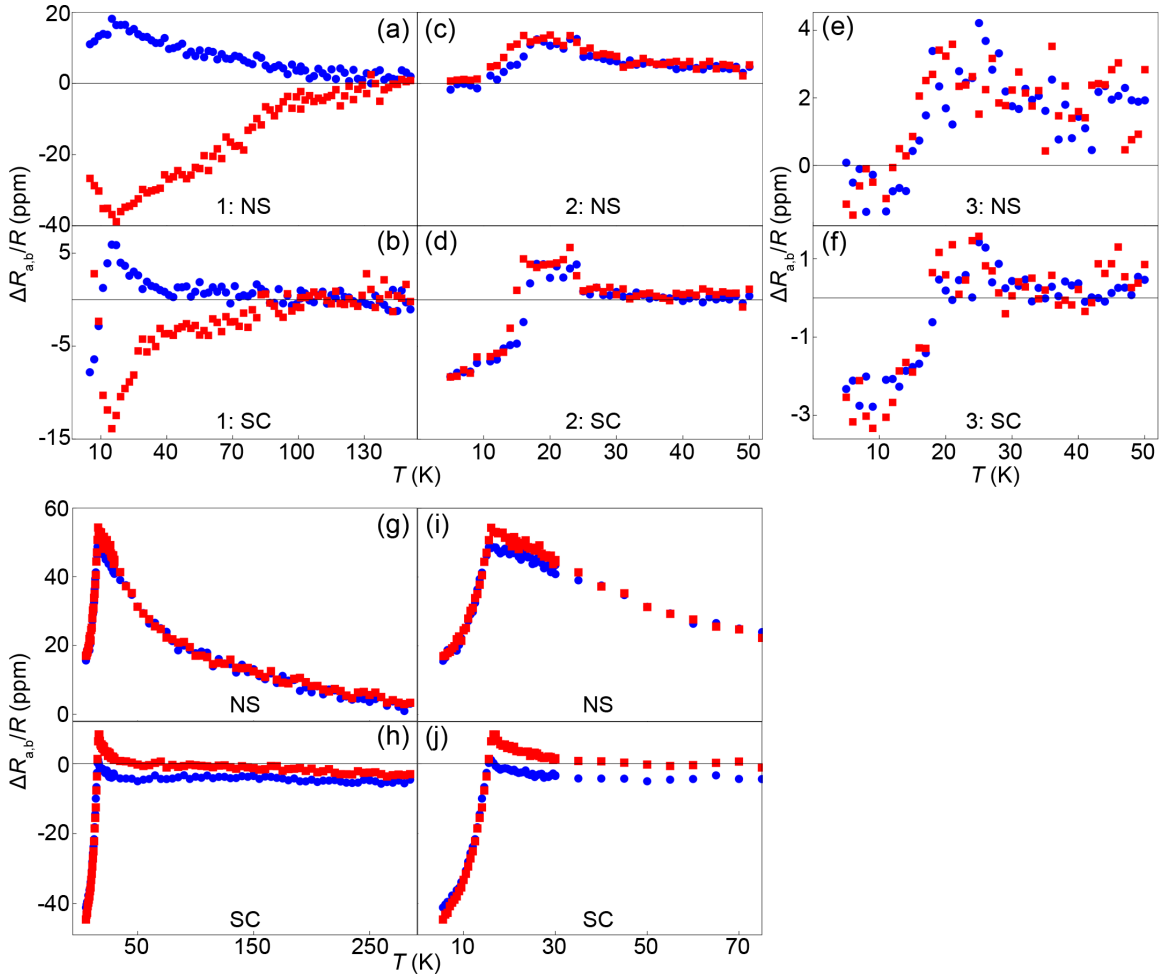

Figure 6.5: Temperature dependence of photomodulation response in strongly overdoped P:Ba122 ($x = 0.50$, $T_c = 18$ K). (a-b), (c-d), (e-f) Normal-state (NS) (a, c, e) and superconducting (SC) (b, d, f) components of $\Delta R_{a,b}(t)/R$ at points 1, 2, and 3 in Fig. 6.4(a), respectively. (g-h) Normal-state (g) and superconducting (h) components of $\Delta R_{a,b}(t)/R$ at a fourth point (point 4) near point 3 in Fig. 6.4(e-f), with pump power increased by a factor of 13.1 relative to points 1−3. Blue circles and red squares correspond to data collected with probe polarizations parallel to orthogonal Fe−Fe directions. (i-j) Same data as (g-h), respectively, for $T < 75$ K.

the superconducting component is stronger along one Fe−Fe axis, and there is once again an apparent discrepancy (now 0.5 K) in the apparent T_c between the two polarizations. Note that a slight imbalance in pump fluence cannot explain the observed discrepancy, as the stronger response corresponds to the higher apparent T_c.

Panels (k-t) of Fig. 6.6 show selected $\Delta R/R$ time traces at point 4, in the isotropic region near point 3, from the dataset corresponding to panels (g-j) in Fig. 6.5. The normal-state

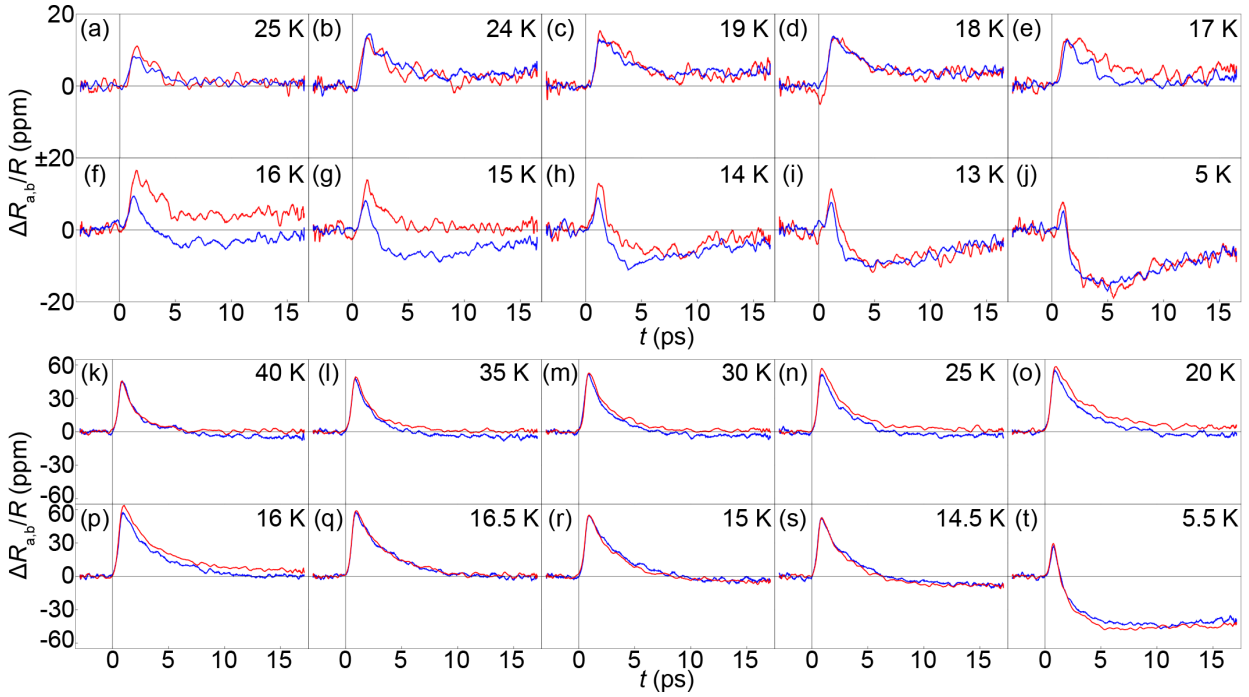

Figure 6.6: Selected $\Delta R/R$ traces in strongly overdoped P:Ba122 ($x = 0.50$, $T_c = 18$ K) showing the difference in apparent T_c between orthogonal probe polarizations. (a-j) Point 2 (labelled in Fig. 6.4(a) and panels (c-d) in Fig. 6.5). $T = 25$ K, 24 K, 19 K, 18 K, 17 K, 16 K, 15 K, 14 K, 13 K, and 5 K, respectively. (k-t) Point 4 (near point 3 in Fig. 6.4(a) and panels (g-j) in Fig. 6.5). $T = 40$ K, 35 K, 30 K, 25 K, 20 K, 16 K, 15.5 K, 15 K, 14.5 K, and 5.5 K, respectively. Blue and red traces correspond to the blue circle and red square datasets in Fig. 6.5.

response at 40 K is isotropic, and with decreasing temperature one polarization (red traces) becomes relatively stronger at early times. The beginning of the superconducting transition occurs at a (nominal) temperature between 15.5 K and 16 K for the red traces (the late time response decreases sharply), and between 15.5 K and 15 K for the blue traces. Below T_c the normal-state response is once again isotropic, and the superconducting response is very nearly so.

6.2.3 $T_c = 23$ K, $x = 0.44$

In Figure 6.7 we show the spatial variation and temperature dependence of the photomodulation response in a moderately overdoped sample with $x = 0.44$. From the map of nematicity in panel (a) it is clear that this sample has a particularly isotropic photomodulation response, similar to the bulk of the $x = 0.50$ sample. (The stronger blue/red points near the edge of panel (a) are artifacts of excess diffuse scatter of the pump beam from the rough sample surface.) Nonetheless, at point 1, near the boundary of a cleaving plane, we did observe

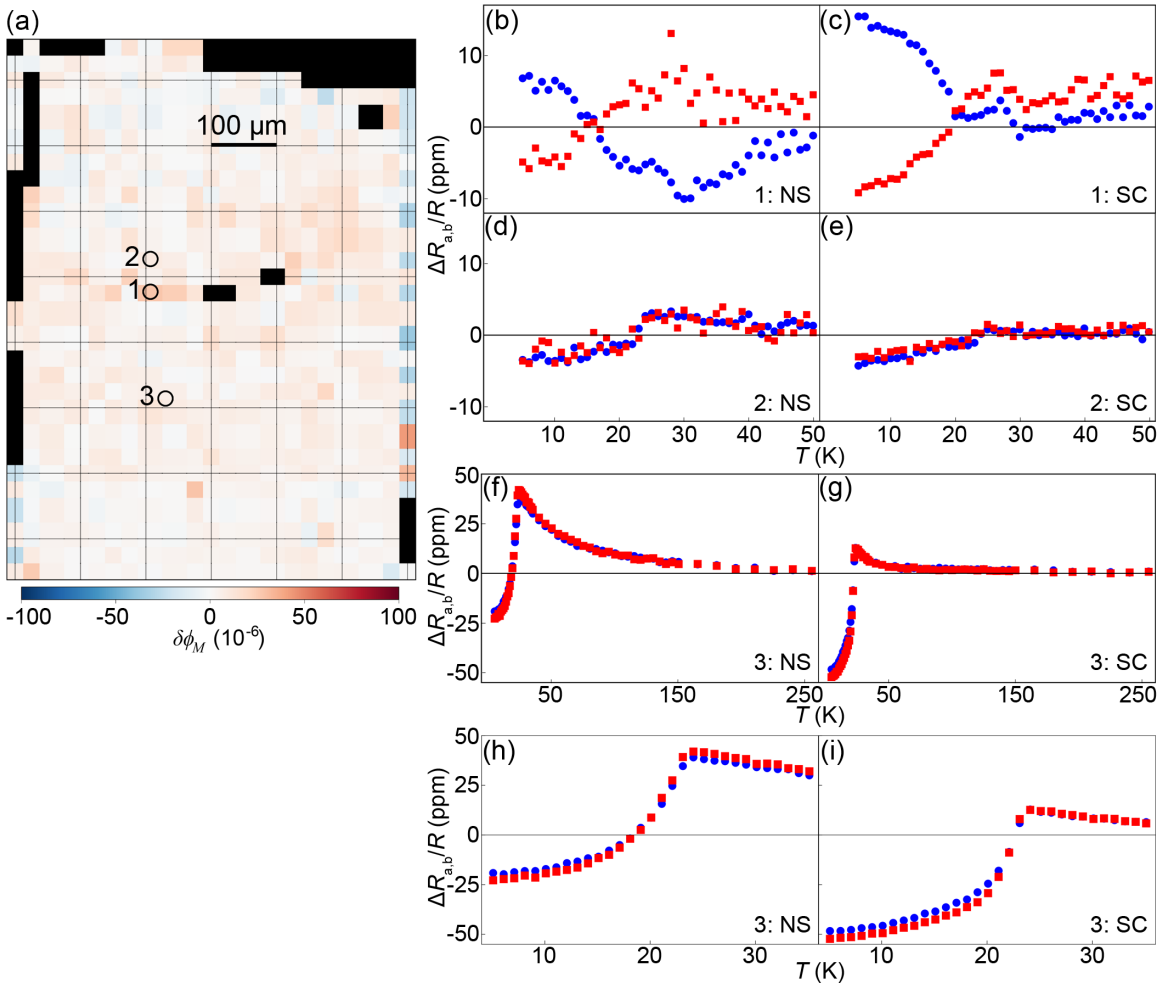

Figure 6.7: Spatial variation of optical anisotropy at 5 K and temperature dependence of photomodulation response in moderately overdoped P:Ba122 ($x = 0.44$, $T_c = 23$ K). (a) Map of photomodulation proxy for nematic order, $\delta\phi_M$. Numbered circles are locations of temperature scans. (b-c), (d-e), (f-g) Temperature dependence of normal-state (NS) (b, d, f) and superconducting (SC) (c, e, g) components of $\Delta R_{a,b}(t)/R$ at points 1, 2, and 3 respectively. (h-i) Same data as (f-g), respectively, for $T < 35$ K. Pump power used at point 3 (f-i) was larger by a factor of 4.3 relative to points 1, 2 (b-e).

a nematic response (panels (b-c)), albeit a weak one. The nematicity in the normal-state response onsets above 50 K and changes sign below T_c, while the long-time superconducting component becomes nematic at T_c. At point 2, 50 μm away (panels (d-e)), the photomodulation response is isotropic and qualitatively identical to the response at point 3 on the $x = 0.50$ sample. At point 3 and with the pump power increased by a factor of 4.3 (panels (f-i)), the response remains highly isotropic, although we measure a slight difference in the strength of both the normal-state and superconducting components below T_c for orthogonal probe

polarizations. Notably, we do not observe any discrepancy in T_c.

6.3 Discussion

Our results suggest two primary conclusions: that nematicity in the overdoped regime is associated with sample topography rather than strain, and that the fraction of a crystal's surface that exhibits strong nematicity decreases quickly with increasing P fraction above $x = 0.39$, although nematic regions of both signs were observed in all samples studied.

These new data reinforce our previous conclusion, originally stated in Sec. 5.2, that the physics of these materials is strongly inhomogeneous at the $10-100$ μm scale. This inhomogeneity is manifested not just in the changing strength or sign of an order parameter, but in very qualitative features like the presence or absence of a change in sign of the photomodulation response under polarization rotation.

We now consider the data from the overdoped regime in the context of the hypothesis, presented in Ch. 5, that the observed nematicity is a product of a surface-nematic phase. This hypothesis was initially motivated by the apparent inconsistency between bulk [8, 27, 15] and surface [28, 29, 31] probes on the question of the presence of nematic effects at and above optimal doping, including above our maximum doping $x = 0.50$, and by theoretical considerations suggesting that a surface nematic phase could be a natural result of interlayer interactions in the P:Ba122 system [50]. The nematicity measured via our photomodulation technique is proportional to the depth of the surface phase in the limit that this phase is thin compared to the optical wavelength, as discussed in Sec. 2.4. The photomodulation data in this chapter show strongly reduced nematicity above $x = 0.39$, while ARPES measurements at wavelength 30 nm show a gradually decreasing orbital anisotropy in the overdoped regime [29]. This implies that if the nematicity is indeed the result of a surface phase, that phase must become thin with increasing P doping above $x = 0.39$. More speculatively, the observation that nematicity in the overdoped regime is concentrated near the edges of samples may also point to the idea of the surface nematic. Roughness in this edge region, particularly flaking along the c-axis, would tend to contain more surface per unit optically probed volume, and thus exhibit a stronger nematic response.

We also observe that the qualitative character of the $\Delta R(t)/R$ traces in non-nematic regions is similar to the nematic case, with a short-lived normal-state response observed above and just below T_c and a long-lived superconducting response becoming dominant as T decreases below T_c. This indicates that the picture suggested in Sec. 4.3.3, which proposes that the superconducting phase is observed primarily via its repulsive coupling to the nematic phase, must be refined. In this adjusted picture, the superconducting phase corresponds with a normal-state order parameter that is not necessarily nematic. This model presents another question, however: if this picture is correct, what are the order parameter and broken symmetry corresponding to this normal-state phase that competes with superconductivity?

Finally, we observe a dependence of the apparent superconducting critical temperature on pump/probe polarization at $x = 0.50$. This cannot be a result of an anisotropy in pump

intensity (and thus sample heating), because the polarization corresponding to stronger photomodulation response has a higher apparent T_c (red squares in Fig. 6.5(i-j)). Nor can absorption anisotropy explain the effect: the T_c shift is large compared to the apparent heating, which would require an absorption anisotropy comparable to 100%; this is not observed.

Chapter 7

Summary and prospects

As we continue to refine our phenomenological understanding of high-T_c superconductivity in pursuit of a final theory, a deepening understanding of the rich and varied phase diagrams of these materials will likely play an important role.

In this thesis we have undertaken a study of nematic physics and inhomogeneity in the isovalently doped superconductor $BaFe_2(As_{1-x}P_x)_2$. Using ultrafast pump-probe reflectance measurements as a form of photomodulation, we found that a phase with broken rotational symmetry is apparent well beyond the boundary of the bulk orthorhombic phase.

We studied the spatial variation of this nematic phase and found that it is strongly inhomogeneous at the length scale of $10-100$ μm. This is both smaller than the typical size of crystals grown via popular methods and significantly larger than the characteristic distances of most microscopy techniques. In an inhomogeneous setting like this, any measurement that either averages over the entire sample or probes a local region smaller than 1 μm will tend to overlook important effects. Understanding the behavior of real materials thus requires probing them at multiple scales.

We combined our photomodulation microscopy measurements with spatially resolved Laue diffraction, and determined that the unexpected nematicity was not a product of intrinsic strain conditions, and that especially in the strongly overdoped regime ($x > 0.4$) it appears to be associated instead with sample topography, namely proximity to sample edges and boundaries between cleaving planes. However, for an optimally doped crystal under significant extrinsic uniaxial strain, we found that the population of nematic domains was biased, consistent with expectation based on a large nematic susceptibility. By continuously tuning the uniaxial strain up from zero, the crossover from the intrinsic, strain-independent regime to the extrinsic, strain-tuned regime could be studied.

The observed inhomogeneous nematic phase, which is evident via optical and ARPES measurements but not via several bulk-sensitive techniques, is consistent with a hypothesized surface nematic phase. This model could be further tested by simultaneously probing a sample using surface-sensitive and bulk-sensitive techniques. If the surface phase picture is confirmed, it may generalize to other layered compounds where two-dimensional physics is dominant, especially those in the vicinity of a quantum critical point.

Bibliography

[1] H. Kamerlingh Onnes, "The resistance of pure mercury at helium temperatures," *Commun. Phys. Lab. Univ. Leiden, b*, vol. 120, 1911.

[2] J. Bardeen, L. N. Cooper, and J. R. Schrieffer, "Theory of superconductivity," *Physical Review*, vol. 108, no. 5, p. 1175, 1957.

[3] J. G. Bednorz and K. A. Müller, "Possible high T_c superconductivity in the Ba-La-Cu-O system," *Zeitschrift für Physik. B, Condensed matter*, vol. 64, no. 2, pp. 189–193, 1986.

[4] Y. Kamihara, T. Watanabe, M. Hirano, and H. Hosono, "Iron-based layered superconductor La[$O_{1-x}F_x$]FeAs (x= 0.05-0.12) with T_c= 26 K," *Journal of the American Chemical Society*, vol. 130, no. 11, pp. 3296–3297, 2008.

[5] H. Takahashi, K. Igawa, K. Arii, Y. Kamihara, M. Hirano, and H. Hosono, "Superconductivity at 43 K in an iron-based layered compound $LaO_{1-x}F_xFeAs$," *Nature*, vol. 453, no. 7193, pp. 376–378, 2008.

[6] M. Rotter, M. Tegel, and D. Johrendt, "Superconductivity at 38 K in the iron arsenide $(Ba_{1-x}K_x)Fe_2As_2$," *Physical Review Letters*, vol. 101, no. 10, p. 107006, 2008.

[7] B. Matthias, "Chapter v superconductivity in the periodic system," in *Progress in low temperature physics*, vol. 2, pp. 138–150, Elsevier, 1957.

[8] D. Hu, X. Lu, W. Zhang, H. Luo, S. Li, P. Wang, G. Chen, F. Han, S. R. Banjara, A. Sapkota, *et al.*, "Structural and magnetic phase transitions near optimal superconductivity in $BaFe_2(As_{1-x}P_x)_2$," *Physical Review Letters*, vol. 114, no. 15, p. 157002, 2015.

[9] M. Rotter, C. Hieke, and D. Johrendt, "Different response of the crystal structure to isoelectronic doping in $BaFe_2(As_{1-x}P_x)_2$ and $(Ba_{1-x}Sr_x)Fe_2As_2$," *Physical Review B*, vol. 82, no. 1, p. 014513, 2010.

[10] S. A. Kimber, A. Kreyssig, Y.-Z. Zhang, H. O. Jeschke, R. Valentí, F. Yokaichiya, E. Colombier, J. Yan, T. C. Hansen, T. Chatterji, *et al.*, "Similarities between structural distortions under pressure and chemical doping in superconducting $BaFe_2As_2$," *Nature materials*, vol. 8, no. 6, p. 471, 2009.

[11] Y. Nakai, T. Iye, S. Kitagawa, K. Ishida, H. Ikeda, S. Kasahara, H. Shishido, T. Shibauchi, Y. Matsuda, and T. Terashima, "Unconventional superconductivity and antiferromagnetic quantum critical behavior in the isovalent-doped $BaFe_2(As_{1-x}P_x)_2$," *Physical Review Letters*, vol. 105, no. 10, p. 107003, 2010.

[12] J.-H. Chu, J. G. Analytis, D. Press, K. De Greve, T. D. Ladd, Y. Yamamoto, and I. R. Fisher, "In-plane electronic anisotropy in underdoped $Ba(Fe_{1-x}Co_x)_2As_2$ revealed by partial detwinning in a magnetic field," *Physical Review B*, vol. 81, no. 21, p. 214502, 2010.

[13] J.-H. Chu, H.-H. Kuo, J. G. Analytis, and I. R. Fisher, "Divergent nematic susceptibility in an iron arsenide superconductor," *Science*, vol. 337, no. 6095, pp. 710–712, 2012.

[14] H.-H. Kuo, J. G. Analytis, J.-H. Chu, R. M. Fernandes, J. Schmalian, and I. R. Fisher, "Magnetoelastically coupled structural, magnetic, and superconducting order parameters in $BaFe_2(As_{1-x}P_x)_2$," *Physical Review B*, vol. 86, no. 13, p. 134507, 2012.

[15] J. M. Allred, K. M. Taddei, D. E. Bugaris, S. Avci, D. Y. Chung, H. Claus, C. dela Cruz, M. G. Kanatzidis, S. Rosenkranz, R. Osborn, *et al.*, "Coincident structural and magnetic order in $BaFe_2(As_{1-x}P_x)_2$ revealed by high-resolution neutron diffraction," *Physical Review B*, vol. 90, no. 10, p. 104513, 2014.

[16] S. A. Kivelson and H. Yao, "Iron-based superconductors: unity or diversity?," *Nature materials*, vol. 7, no. 12, pp. 927–928, 2008.

[17] S. Kasahara, T. Shibauchi, K. Hashimoto, K. Ikada, S. Tonegawa, R. Okazaki, H. Shishido, H. Ikeda, H. Takeya, K. Hirata, *et al.*, "Evolution from non-fermi-to fermi-liquid transport via isovalent doping in $BaFe_2(As_{1-x}P_x)_2$ superconductors," *Physical Review B*, vol. 81, no. 18, p. 184519, 2010.

[18] J. G. Analytis, H. H. Kuo, R. D. McDonald, M. Wartenbe, P. M. C. Rourke, N. E. Hussey, and I. R. Fisher, "Transport near a quantum critical point in $BaFe_2(As_{1-x}P_x)_2$," *Nature Physics*, vol. 10, no. 3, pp. 194–197, 2014.

[19] T. Shibauchi, A. Carrington, and Y. Matsuda, "A quantum critical point lying beneath the superconducting dome in iron pnictides," *Annu. Rev. Condens. Matter Phys.*, vol. 5, no. 1, pp. 113–135, 2014.

[20] K. Hashimoto, K. Cho, T. Shibauchi, S. Kasahara, Y. Mizukami, R. Katsumata, Y. Tsuruhara, T. Terashima, H. Ikeda, M. A. Tanatar, *et al.*, "A sharp peak of the zero-temperature penetration depth at optimal composition in $BaFe2(as_{1-x}P_x)_2$," *Science*, vol. 336, no. 6088, pp. 1554–1557, 2012.

[21] H.-H. Kuo, J.-H. Chu, J. C. Palmstrom, S. A. Kivelson, and I. R. Fisher, "Ubiquitous signatures of nematic quantum criticality in optimally doped Fe-based superconductors," *Science*, vol. 352, no. 6288, pp. 958–962, 2016.

[22] D. Chowdhury, B. Swingle, E. Berg, and S. Sachdev, "Singularity of the london penetration depth at quantum critical points in superconductors," *Physical Review Letters*, vol. 111, no. 15, p. 157004, 2013.

[23] D. Chowdhury, J. Orenstein, S. Sachdev, and T. Senthil, "Phase transition beneath the superconducting dome in $BaFe_2(As_{1-x}P_x)_2$," *arXiv preprint arXiv:1502.04122*, 2015.

[24] V. Grinenko, K. Iida, F. Kurth, D. Efremov, S.-L. Drechsler, I. Cherniavskii, I. Morozov, J. Hänisch, T. Förster, C. Tarantini, *et al.*, "Selective mass enhancement close to the quantum critical point in $BaFe_2(As_{1-x}P_x)_2$," *Scientific Reports*, vol. 7, no. 1, p. 4589, 2017.

[25] E. Fradkin, S. A. Kivelson, M. J. Lawler, J. P. Eisenstein, and A. P. Mackenzie, "Nematic Fermi fluids in condensed matter physics," *Annu. Rev. Condens. Matter Phys.*, vol. 1, no. 1, pp. 153–178, 2010.

[26] R. M. Fernandes, A. V. Chubukov, and J. Schmalian, "What drives nematic order in iron-based superconductors?," *Nature Physics*, vol. 10, no. 2, pp. 97–104, 2014.

[27] P. Walmsley, C. Putzke, L. Malone, I. Guillamón, D. Vignolles, C. Proust, S. Badoux, A. I. Coldea, M. Watson, S. Kasahara, *et al.*, "Quasiparticle mass enhancement close to the quantum critical point in $BaFe_2(As_{1-x}P_x)_2$," *Physical Review Letters*, vol. 110, no. 25, p. 257002, 2013.

[28] T. Shimojima, T. Sonobe, W. Malaeb, K. Shinada, A. Chainani, S. Shin, T. Yoshida, S. Ideta, A. Fujimori, H. Kumigashira, *et al.*, "Pseudogap formation above the superconducting dome in iron pnictides," *Physical Review B*, vol. 89, no. 4, p. 045101, 2014.

[29] T. Sonobe, T. Shimojima, A. Nakamura, M. Nakajima, S. Uchida, K. Kihou, C. Lee, A. Iyo, H. Eisaki, K. Ohgushi, *et al.*, "Orbital-anisotropic electronic structure in the nonmagnetic state of $BaFe_2(As_{1-x}P_x)_2$ superconductors," *Scientific Reports*, vol. 8, no. 1, p. 2169, 2018.

[30] S. Kasahara, H. J. Shi, K. Hashimoto, S. Tonegawa, Y. Mizukami, T. Shibauchi, K. Sugimoto, T. Fukuda, T. Terashima, A. H. Nevidomskyy, *et al.*, "Electronic nematicity above the structural and superconducting transition in $BaFe_2(As_{1-x}P_x)_2$," *Nature*, vol. 486, no. 7403, pp. 382–385, 2012.

[31] L. Stojchevska, T. Mertelj, J.-H. Chu, I. R. Fisher, and D. Mihailovic, "Doping dependence of femtosecond quasiparticle relaxation dynamics in $Ba(Fe,Co)_2As_2$ single crystals: Evidence for normal-state nematic fluctuations," *Phys. Rev. B*, vol. 86, p. 024519, 2012.

[32] N. Barišić, D. Wu, M. Dressel, L. Li, G. Cao, and Z. Xu, "Electrodynamics of electron-doped iron pnictide superconductors: Normal-state properties," *Physical Review B*, vol. 82, no. 5, p. 054518, 2010.

[33] N. Tamura, A. A. MacDowell, R. Spolenak, B. C. Valek, J. C. Bravman, W. L. Brown, R. S. Celestre, H. A. Padmore, B. W. Batterman, and J. R. Patel, "Scanning X-ray microdiffraction with submicrometer white beam for strain/stress and orientation mapping in thin films," *Journal of Synchrotron Radiation*, vol. 10, no. 2, pp. 137–143, 2003.

[34] C. Kittel, *Introduction to Solid State Physics, Eigth Edition*, pp. 39–42. John Wiley & Sons, Inc., 2005.

[35] L. Wu, A. Little, E. E. Aldape, D. Rees, E. Thewalt, P. Lampen-Kelley, A. Banerjee, C. A. Bridges, J. Yan, S. Patankar, *et al.*, "Field evolution of magnons in α-RuCl $_3$ by high-resolution polarized terahertz spectroscopy," *arXiv preprint arXiv:1806.00855*, 2018.

[36] A. Carrington, "Quantum oscillation studies of the fermi surface of iron-pnictide superconductors," *Reports on Progress in Physics*, vol. 74, no. 12, p. 124507, 2011.

[37] M. A. Tanatar, A. Kreyssig, S. Nandi, N. Ni, S. L. BudâĂŹko, P. C. Canfield, A. I. Goldman, and R. Prozorov, "Direct imaging of the structural domains in the iron pnictides AFe_2As_2(A=Ca, Sr, Ba)," *Physical Review B*, vol. 79, no. 18, p. 180508, 2009.

[38] B. Kalisky, J. R. Kirtley, J. G. Analytis, J.-H. Chu, A. Vailionis, I. R. Fisher, and K. Moler, "Stripes of increased diamagnetic susceptibility in underdoped superconducting $Ba(Fe_{1-x}Co_x)_2As_2$ single crystals: Evidence for an enhanced superfluid density at twin boundaries," *Physical Review B*, vol. 81, no. 18, p. 184513, 2010.

[39] H. Shishido, A. F. Bangura, A. I. Coldea, S. Tonegawa, K. Hashimoto, S. Kasahara, P. M. C. Rourke, H. Ikeda, T. Terashima, R. Settai, *et al.*, "Evolution of the fermi surface of $BaFe_2(As_{1-x}P_x)_2$ on entering the superconducting dome," *Physical Review Letters*, vol. 104, no. 5, p. 057008, 2010.

[40] E. Abrahams and Q. Si, "Quantum criticality in the iron pnictides and chalcogenides," *Journal of physics: Condensed matter*, vol. 23, no. 22, p. 223201, 2011.

[41] L. W. Harriger, H. Q. Luo, M. S. Liu, C. Frost, J. P. Hu, M. R. Norman, and P. Dai, "Nematic spin fluid in the tetragonal phase of $BaFe_2As_2$," *Physical Review B*, vol. 84, no. 5, p. 054544, 2011.

[42] M. Yi, D. Lu, J.-H. Chu, J. G. Analytis, A. P. Sorini, A. F. Kemper, B. Moritz, S.-K. Mo, R. G. Moore, M. Hashimoto, *et al.*, "Symmetry-breaking orbital anisotropy observed for detwinned $Ba(Fe_{1-x}Co_x)_2As_2$ above the spin density wave transition," *Proceedings of the National Academy of Sciences*, vol. 108, no. 17, pp. 6878–6883, 2011.

[43] A. E. Böhmer, P. Burger, F. Hardy, T. Wolf, P. Schweiss, R. Fromknecht, M. Reinecker, W. Schranz, and C. Meingast, "Nematic susceptibility of hole-doped and electron-doped $BaFe_2As_2$ iron-based superconductors from shear modulus measurements," *Physical Review Letters*, vol. 112, no. 4, p. 047001, 2014.

[44] M. A. Metlitski, D. F. Mross, S. Sachdev, and T. Senthil, "Cooper pairing in non-fermi liquids," *Physical Review B*, vol. 91, no. 11, p. 115111, 2015.

[45] S. Lederer, Y. Schattner, E. Berg, and S. A. Kivelson, "Enhancement of superconductivity near a nematic quantum critical point," *Physical Review Letters*, vol. 114, no. 9, p. 097001, 2015.

[46] T. A. Maier and D. J. Scalapino, "Pairing interaction near a nematic QCP of a 3-band CuO_2 model," *arXiv preprint arXiv:1405.5238*, 2014.

[47] Q. Si, R. Yu, and E. Abrahams, "High-temperature superconductivity in iron pnictides and chalcogenides," *Nature Reviews Materials*, vol. 1, p. 16017, 2016.

[48] W. J. Duncan, O. P. Welzel, C. Harrison, X. F. Wang, X. H. Chen, F. M. Grosche, and P. G. Niklowitz, "High pressure study of $BaFe_2As_2$âĂŤthe role of hydrostaticity and uniaxial stress," *Journal of Physics: Condensed Matter*, vol. 22, no. 5, p. 052201, 2010.

[49] M. Cardona, K. L. Shaklee, and F. H. Pollak, "Electroreflectance at a semiconductor-electrolyte interface," *Physical Review*, vol. 154, pp. 696–720, Feb 1967.

[50] K. W. Song and A. E. Koshelev, "Surface nematic order in iron pnictides," *Physical Review B*, vol. 94, no. 9, p. 094509, 2016.

[51] M. A. Tanatar, E. C. Blomberg, A. Kreyssig, M. G. Kim, N. Ni, A. Thaler, S. L. Bud'ko, P. C. Canfield, A. I. Goldman, I. I. Mazin, *et al.*, "Uniaxial-strain mechanical detwinning of $CaFe_2As_2$ and $BaFe_2As_2$ crystals: Optical and transport study," *Physical Review B*, vol. 81, no. 18, p. 184508, 2010.

[52] A. E. Böhmer, A. Sapkota, A. Kreyssig, S. L. Bud'ko, G. Drachuck, S. M. Saunders, A. I. Goldman, and P. C. Canfield, "Effect of biaxial strain on the phase transitions of $Ca(Fe_{1-x}Co_x)_2As_2$," *Physical Review Letters*, vol. 118, no. 10, p. 107002, 2017.

[53] S. E. Brown, E. Fradkin, and S. A. Kivelson, "Surface pinning of fluctuating charge order: An extraordinary surface phase transition," *Physical Review B*, vol. 71, no. 22, p. 224512, 2005.

[54] S. Brückner, "Estimation of the background in powder diffraction patterns through a robust smoothing procedure," *Journal of Applied Crystallography*, vol. 33, no. 3-2, pp. 977–979, 2000.

[55] International Union of Crystallography, "Online Dictionary of Crystallography: Wyckoff position." `http://reference.iucr.org/dictionary/Wyckoff_position`. Accessed: 2018-08-28.

[56] SchedMD, "Slurm workload manager: squeue." `https://slurm.schedmd.com/squeue.html`. Accessed: 2018-08-28.

[57] Available on request from the author or the micro-Laue beamline scientists.

[58] U.S. Department of Energy, Office of Science, "National Energy Research Scientific Computing Center." `http://www.nersc.gov/`. Accessed: 2018-08-28.

Appendix A

Laue indexing tips and tricks

In this appendix we give in-depth instructions and practical advice on the sometimes-difficult process of fitting a crystal orientation and strain tensor to a Laue diffraction pattern or a many-pattern data set. The first step, described in Sec. A.1, is to use the XMAS desktop software to optimize the peak identification and Laue indexing. Section A.2 explains the process of porting the resulting configuration to the XMAS cluster for automated analysis of many images in parallel.

A.1 Laue fitting with XMAS desktop

The first step is to load a diffraction pattern via `File` → `Load image`. If you did not copy your data to a portable drive during the beamtime, you can either register for an XMAS cluster account and copy your data from the cluster file storage (see Sec. A.2 for details), or ask a beamline scientist to help you copy data manually. If the map covers a large area, it is preferable to choose an image near the center of the region of interest.

After loading an image, `Image` → `Fit and Remove Background` will remove the slow-varying background component of the diffraction pattern, leaving only the peaks. The background substraction is performed using the Brückner algorithm [54], which amounts to repeated applications of a low-pass filter alternating in the horizontal and vertical directions.

Once the background is removed, the peaks can be identified using the `Analysis` → `Peak Search` window. The two most useful settings in this window are the multiplicative threshold, which is the value a candidate peak must exceed to count as a peak, and the box size, which is the linear size of the region of the image corresponding to each peak (where no other peaks can be found within this region). Unless the diffraction pattern is very weak, a good value for the multiplicative threshold is around 4. For an image with around 100 peaks, a box size of 8-10 pixels is appropriate; with more peaks a smaller box size is warranted. For a Laue pattern with 450 peaks we have found that a box size of 4 pixels is effective. One note about the XMAS desktop software: when entering a value into an input box, the new value will not take effect until you move the mouse into and out of the input box.

It is very helpful to ignore the immediate vicinity of some bad (dead or incorrectly bright) detector pixels. This is achieved by checking the *Remove peaks* box and selecting a file that lists the peaks to remove in the top right corner of the window; see Sec. A.1.1 for details on bad pixels and the construction of this file.

Next, load the crystal structure file (in `.cri` format) corresponding to the sample you are indexing into XMAS. You will first have to copy the file into the `crysfiles/` directory in the XMAS installation directory, usually `C:/XMASv6/`. Then you can import the crystal structure via the `Parameters` → `Crystal Structure` window.

If you do not have a `.cri` file corresponding to your sample but you know the crystal structure, you can construct the file manually. The file format is quite straightforward: the first line is the name of the structure, the second line states the space group number, the third line contains the lattice parameters a, b, c, α, β, and γ (in nm and degrees), and the fourth line states the number of Wyckoff positions (essentially, a minimal list of atomic locations that generate the unit cell under the crystal symmetry operations; see [55] for more information). The remaining lines define the Wyckoff positions, first the atom and then the location in relative coordinates. The following is a full `.cri` file corresponding to $BaFe_2(As_{0.69}P_{0.31})_2$, for reference.

`PBa122_opt.cri`

```
Optimally doped BaFe2(AsP)2
   139
   0.39299   0.39299   1.28385  90.00000  90.00000  90.00000
     4
Ba001    0.00000   0.00000   0.00000   1.00000
Fe001    0.00000   0.50000   0.25000   1.00000
As001    0.00000   0.00000   0.35191   0.69000
P0001    0.00000   0.00000   0.35191   0.31000
```

Before indexing the peaks, we must configure the indexing algorithm via `Parameters` → `Calibration Parameters`. Here, the most useful parameters are the angular tolerance, the starting set size, and the minimum number of indexed peaks. The angular tolerance is the maximum angular distance between a peak and its predicted position for the peak to be considered successfully indexed. During the process of optimizing the geometrical calibration it can be helpful to use a large angular tolerance (say, 0.1 degrees), but once the geometry is determined this value should be reduced to approximately 0.05 degrees. The starting set is a set of the brightest peaks, from which the indexing attempts begin. For single crystals, a starting set of 10 is a good choice. Larger starting sets may help for Laue images consisting of multiple overlaid single-crystal patterns. Once an indexing attempt has successfully indexed a number of peaks that exceeds the minimum, the fitting stops and the resulting orientation is returned. This parameter should be reasonably large; between 50 and 100 should suffice for most diffraction patterns, with a higher threshold needed when more peaks are present.

Once the Laue indexing algorithm is configured, it can be started via `Analysis` → `Laue indexing`. It will run for some time on the order of minutes, and then return the

fit results. The number of indexed peaks at the top of the Laue indexing window is the main indicator of whether the indexing was successful; this number should be fairly large.

If the indexing is successful we can use the resulting fit to refine the sample and detector geometry. This simply fixes the crystal orientation and varies the geometric parameters to minimize the RMS deviation of the peaks from their predicted positions. First, we must use the `Parameters` → `Strain/Calibration Laue refinement parameters` window to make sure that we will be refining the geometry rather than the crystal unit cell geometry. Deselect the check boxes on the left corresponding to the unit cell parameters and select the boxes on the right corresponding to `distance`, `xcent`, `ycent`, `pitch`, and `yaw`. Then refine the geometry via `Analysis` → `Strain RefinementCalibration`, and update the calibration using the `SET NEW CALIBRATION` button in the resulting window.

For best results, iterate the Laue indexing and geometry refinement steps a few times.

A.1.1 Dead pixels

Here we include the contents of a text file, `dead_pix.msk`, listing dead and otherwise faulty pixels on the Pilatus detector currently in use at the micro-Laue beamline. Failing to ignore these pixels can cause the peak-finding algorithm to erroneously detect extremely bright peaks, which can then throw off the Laue indexing algorithm.

`dead_pix.msk`

```
18
927 545
862 11
530 46
49 235
317 392
921 586
966 157
895 37
713 633
1008 55
879 684
486 97
54 865
880 194
928 544
928 545
879 685
580 238
```

A.2 Laue fitting on the XMAS cluster

After successfully fitting an example diffraction pattern and refining the sample and detector geometry using the XMAS desktop software, we can proceed to the automatic analysis of an entire micro-Laue map on the XMAS cluster, a part of the Berkeley Laboratory Research

Computing cluster. You will need the approval of the micro-Laue beamline scientist to set up an account on the XMAS cluster.

Once you have an account you can use SSH to access the cluster:

```
ssh [username]@lrc-login.lbl.gov
```

Once you have logged in for the first time, copy the XMAS cluster executables into your new home directory. As of the time of writing, these executables are located in the directory /clusterfs/xmas/xmas-exec/. Copy the param/ directory in xmas-exec/ into your home directory as well.

Your data will be located in a directory like the following:

```
/clusterfs/xmas/xmas-storage/2018/orenstein_Feb2018/
```

Your cluster jobs will require all the input data the desktop software requires, namely a crystal structure .cri file and a list of bad pixels. You can use SCP to copy these files to the cluster, along with your NERSC file, which is discussed further in Sec. A.2.1. For example,

```
scp dead_pix.msk [username]@lrc-login.lbl.gov:/global/home/users/[username]/
```

The XMAS cluster is a shared resource. Before submitting a large job, it is a good idea to check whether any other users have active jobs on the cluster using the live status page at http://metacluster.lbl.gov/warewulf/xmas. If the cluster is in use, it may be prudent to scale down the number of CPU cores your job requires by adjusting the CLUSTERNUMNO setting in the NERSC file. If the cluster is not in use, it is best to use a relatively large number of cores, since jobs on the cluster expire after two hours whether or not they are complete.

To submit your job, navigate to the directory where you copied the XMAS executables, and run the XMASparamsplit_new.exe executable:

```
./XMASparamsplit_new.exe
```

An empty input field will appear. In this field, enter the path to the NERSC file for the job. If successful, the terminal will fill with messages reporting the submission of each sub-job to the cluster.

After submitting your job, you can monitor its progress using the squeue tool [56]. You can monitor the number of active jobs (plus one) using the following command:

```
watch -n 30 "squeue -u [username]" | wc -l
```

Once the job is complete, there will be a new file in the directory where you ran XMASparamsplit_new.exe with a name like s2_coarse.SEQ. You can use SCP from your computer to copy this file to local storage so that you can visualize the results using the XMAS desktop software:

```
scp [username]@lrc-login.lbl.gov:/global/home/users/[username]/[filename].SEQ .
```

Once you have copied your new .SEQ file to your computer, you can use XMAS desktop to visualize via the Analysis → Read Analysis sequential list window. Load the .SEQ file using the LOAD AS STRUC button and click DISPLAY. The display window has two drop-down menus in the top left where you can select output parameters to display; use the right menu to select a parameter like NINDEX, the number of indexed peaks, and mouse over the image in the bottom left. If you ran a multigrain fit, uncheck the Use brightest peak box. If you accidentally click a pixel on the image, conditions will be imposed on the plotted points and the map will change, often significantly. Simply locate the drop-down menu that

says *3 selection*, change it to *0 selection*, and mouse over the image again. You can use the display window to plot any of the many parameters returned by the cluster fit. For a description of these parameters, refer to the cluster instructions [57].

If `NINDEX` is comparable to what you achieved with the desktop software and relatively uniform, the fit was successful. You can save the data in raw text format using the `Save as list` button in the `Read Analysis sequential list` window. This will produce a much larger file but will allow you to read the data into your preferred analysis software. If there were problems with indexing, assess the issue (can you manually index the images that fail to index on the cluster, and update the calibration accordingly? Are there obvious issues with the diffraction patterns in the regions where indexing fails?). Tweak your parameters (especially angular resolution and starting set), and submit a new job.

A.2.1 The `NERSC` file

The `NERSC` file, whose name is a holdover from when XMAS ran on the `NERSC` cluster [58], contains most of the critical parameters that control the Laue pattern analysis.

The XMAS desktop software allows the user to automatically generate a `NERSC` file using the `Automated analysis` → `Set automatic analysis of Laue patterns` window. This is helpful for first-time users, as it creates a file with the correct formatting and automatically copies in the current peak search, geometry, and Laue indexing parameters. However, once a user has some experience with the XMAS cluster they may find it more efficient and transparent to edit the `NERSC` file directly. Table A.1 names and describes the most important and most frequently changed parameters in the `NERSC` file, and gives example values.

In addition to setting the parameters in Table A.1, we must make sure that we are refining the strain tensor rather than the sample and detector geometry. We do this by setting `STR_BATOGGLE`, `STR_CATOGGLE`, `STR_ALFATOGG`, `STR_BETATOGG`, and `STR_GAMATOGG` to 1 and setting `STR_DDTOGGLE`, `STR_XCENTTOG`, `STR_YCENTTOG`, `STR_PITCHTOG`, `STR_YAWTOGGL`, and `STR_ROLLTOGG` to 0.

Table A.1: Important `NERSC` file parameters

Parameter	Description	Typical value
	Laue indexing	
`CALIB_XRES__`	Angular tolerance in degrees for predicted peak position	0.05
`CALIB_STASET`	Number of peaks to use as the starting point for each fit	10
`CALIB_MININD`	Minimum number of indexed peaks for a successful fit	50−100
	Geometry calibration	
`CALIB_DIST_`	Distance in mm from detector to sample	149.683
`CALIB_XCENT_`	Horizontal position in pixels of center channel*	538.834
`CALIB_YCENT_`	Vertical position in pixels of center channel	228.524
`CALIB_DPITCH`	Detector pitch angle in degrees	0.937690
`CALIB_DYAW__`	Detector yaw angle in degrees	0.643180
`CALIB_DTILij`	(i, j) element of detector tilt matrix	$\sim\delta_{ij}$†
	Multigrain indexing	
`SINGLEMULTIT`	Toggle multigrain fitting off (0) or on (1)	1
`MAXNUMBGRAIN`	Maximum number of grains to fit for each image	3
`CALIB_MULTIG`	Equivalent to `MAXNUMBGRAIN`	3
	Peak finding	
`PEAK_BOXSIZE`	Size in pixels of region exclusive to one peak	4‡
`PEAK_MULTFAC`	Factor by which a peak's max. intensity must exceed background	4
`PEAK_RMVPEAK`	Toggle removal of peaks near bad pixels off (0) or on (1)	1
`PEAK_RMVFILE`	Path to file listing the bad pixels for peak removal	`dead_pix.msk`‖
`PEAK_XTOL___`	Max. horizontal distance in pixels to bad pixel for peak removal	3.00000
`PEAK_YTOL___`	Max. vertical distance in pixels to bad pixel for peak removal	3.00000
	Directory and file information	
`CRYDIRECTORY`	Directory where crystal structure file is located	`./param/`
`CRYFILE_____`	Filename of crystal structure file	`PBa122_opt.cri`
`IMGFILEDIR_`	Directory where images are located	...**
`AUTOLA_PATH_`	Equivalent to `IMGFILEDIR_`	
`AUTOLA_ROOT_`	Root of image filenames	`s2_coarse_`
`AUTOLA_INDFO`	Number of index digits of image filenames	5††
`AUTOLA_SPATH`	Directory to save auxiliary output files	
`AUTOLA_SROOT`	Root of output filenames	`s2_coarse`
	Image selection	
`AUTOLA_START`	Index of the first image to index	1
`AUTOLA_END__`	Index of the final image to index	9375
`AUTOLA_STEP_`	Index increment for selecting images to index	1
`CLUSTERNUMNO`	Number of CPU cores to use	375‡‡

*This is the position of the $(0, 0, 1)$ reflection if the sample is perfectly aligned with the sample stage.

†For pitch θ_p and yaw θ_y the detector tilt matrix T is defined by $T^{-1} = R\left(\theta_y, R(\theta_p, (1,0,0)^T)\cdot(0,0,1)^T\right)\cdot R(\theta_p, (1,0,0)^T)$, where $R(\theta, \mathbf{v})$ is the matrix for a rotation by angle θ about axis $\mathbf{v}$.

‡This parameter can be increased for images with fewer (~ 100) peaks.

‖For a useful list of dead and otherwise faulty pixels, see Sec. A.1.1.

**For example, `/clusterfs/xmas/xmas-storage/2018/orenstein_Feb2018/sample2_coarse/`.

††An example image filename is `sample2_coarse_00001.tif`.

‡‡The number of CPU cores must be a divisor of the number of images to be indexed, Floor ((`AUTOLA_END__` − `AUTOLA_START` + 1)/`AUTOLA_STEP_`), or some images will be left out.